OAK RIDGE
NATIONAL LABORATORY
MANAGED BY UT-BATTELLE
FOR THE DEPARTMENT OF ENERGY

ORNL/TM-2006/83

Implications of the PIE Results for the 50-GWd/MT MOX Test Capsules

S. A. Hodge
L. J. Ott

UT-BATTELLE
ORNL-27 (4-00)

Revision History

Revision No.	Date Issued	Reason for Revision
0	May 2006	Initial issue of report

ORNL/TM-2006/83

Nuclear Science & Technology Division

Implications of the PIE Results for the 50-GWd/MT MOX Test Capsules

S. A. Hodge
L. J. Ott

May 2006

Fissile Materials Disposition Program

Prepared by
OAK RIDGE NATIONAL LABORATORY
P.O. Box 2008
Oak Ridge, Tennessee 37831-6283
managed by
UT-BATTELLE, LLC
for the
U.S. DEPARTMENT OF ENERGY
under contract DE-AC05-00OR22725

CONTENTS

LIST OF FIGURES

LIST OF TABLES

Implications of the PIE Results for the 50-GWd/MT MOX Test Capsules

S. A. Hodge
L. J. Ott

ABSTRACT

For this test program, mixed-oxide (MOX) fuel was prepared with weapons-derived plutonium and irradiated to a burnup of 50 GWd/MT. This MOX fuel was fabricated at Los Alamos National Laboratory by a master-mix process and irradiated in the Advanced Test Reactor (ATR) at Idaho National Laboratory. Previous withdrawals of the same fuel have occurred at 9, 21, 30, and 40 GWd/MT for progressive fuel performance evaluations. Oak Ridge National Laboratory managed this test series for the Department of Energy's Fissile Materials Disposition Program (FMDP) and performed the postirradiation examinations (PIEs). A primary objective of this test irradiation was to demonstrate fuel performance comparable to that of the reactor-grade MOX that has been deployed successfully in overseas reactors for many years and for which a large database exists.

Capsules 5, 6, and 12, all with accumulated burnups near 50 GWd/MT, were withdrawn from the ATR in April 2004. The *MOX Test Fuel 50 GWd/MT PIE: Capsules 6 and 12 Final Report*, ORNL/MD/LTR-279, Volume 1, describes the PIEs performed for Capsules 6 and 12. The Capsule 5 irradiation history reflects lower linear heat generation rates and lower fuel temperatures, and the PIE for this capsule is reported separately, in ORNL/MD/LTR-280, Volume 1, *MOX Test Fuel 50 GWd/MT PIE: Capsule 5 Final Report*. In each case, Volume 1 explains how the PIE was conducted and presents the findings with limited additional comment and analysis. This report serves as Volume 2 to both 50-GWd/MT PIE Volume 1 reports, complementing their information via discussions of the significance of the more important observations such as the gallium concentrations, fission gas release fractions, the plutonium-rich agglomerates, cladding inner surface oxidation, fuel densification and swelling, and outward cladding creep.

---

1. INTRODUCTION

Capsules 5, 6, and 12, all with accumulated burnups near 50 GWd/MT, were withdrawn from the Advanced Test Reactor (ATR) in April 2004. The *MOX Test Fuel 50 GWd/MT PIE: Capsules 6 and 12 Final Report*, ORNL/MD/LTR-279, Volume 1, describes the postirradiation examinations (PIEs) performed for Capsules 6 and 12. The capsule 5 irradiation history reflects lower linear heat generation rates (LHGRs) and lower fuel temperatures, and the PIE for this capsule is reported separately, in ORNL/MD/LTR-280, Volume 1, *MOX Test Fuel 50 GWd/MT PIE: Capsule 5 Final Report.* In each case, Volume 1 explains how the PIE was conducted and presents the findings with limited additional comment and analysis. This report serves as Volume 2 to both Volume 1 reports, complementing their information via discussions of the significance of the more important observations such as the gallium concentrations, fission gas release fractions, the plutonium-rich agglomerates, cladding inner surface oxidation, fuel densification and swelling, and outward cladding creep.

Gallium is an alloying agent present in weapons-derived plutonium. For each successive PIE, fuel and cladding segments were analyzed for gallium content. The purpose was to determine if gallium had migrated from fuel to cladding, a major investigative object of this mixed-oxide (MOX) test irradiation. Chapter 2 addresses the technical issue as to whether the small amount of gallium present in the finished MOX fuel has affected irradiation performance.

Chapter 3 describes the measured fission gas release fractions and the significance of their magnitudes in comparison to the European MOX fuel experience. The preparation of the MOX fuel by the master-mix process and the particular characteristics of the plutonium-rich agglomerates in the irradiated MOX test fuel as observed in the 50-GWd/MT PIEs are discussed in Chapter 4.

The fissioning of heavy metal oxides releases oxygen atoms within the fuel matrix. Most are taken up by fission products or by increasing the oxygen potential of the remaining heavy metal oxides, but a small fraction of these promote cladding inner surface corrosion, which is discussed in Chapter 5. (There is no oxidation of the cladding outer surface, which remained in a helium atmosphere throughout the irradiation.)

The fuel swelling and densification history is derived by reviewing the changes in pellet dimensions from the initial unirradiated state through the successive PIEs conducted at 9, 21, 30, 40, and 50 GWd/MT. Determination of the pellet structural changes depends in turn upon correctly factoring the changes in cladding dimensions, including the effects of outward cladding creep as experienced during this test irradiation. These analytical processes and their results are discussed in Chapter 6.

Cladding diameter increases pursuant to outward cladding creep have been observed in all of the PIEs conducted for this MOX test fuel. This is contrary to the commercial fuel experience where the cladding creeps inward under the impetus of high coolant pressure. Commercially, creep-down occurs initially, closing the fuel-clad gap, but then creep-out occurs under the internal driving force of fuel swelling. The development of a model appropriate for representation of cladding creep for this MOX test irradiation is discussed in Chapter 7.

Chapter 8 reports the results of a set of fuel response calculations performed subsequent to the PIE to illustrate the actual performance of Capsules 6 and 12 during irradiation. The results of similar calculations for Capsule 5 are reported in Chapter 9. In all cases, the code input for the associated calculations has been based specifically upon the PIE observations for the capsule represented.

The overall purpose of this PIE has been to evaluate the performance of this weapons-derived MOX test fuel. The implications of the PIE findings are discussed in this report. The conclusions with respect to fuel performance are summarized in Chapter 10.

Chapter 11 comprises the references cited in this report.

2. GALLIUM MEASUREMENTS AND RESULTS

2.1 Initial Gallium Concentrations

Weapons-derived plutonium includes about one weight percent (10,000 ppm) gallium. The manufacturing process for use of this plutonium in preparation of MOX fuel is designed to reduce this gallium impurity to trace levels. Nevertheless, one of the top-level goals for this MOX test irradiation has been to "contribute experience with irradiation of gallium-containing fuel…" (Reference 1). Accordingly, to determine the extent of any adverse effects associated with gallium at low levels, the MOX test fuel was prepared with about two orders of magnitude more gallium than will be present in the Fissile Materials Disposition Program (FMDP) mission fuel. This section describes the initial gallium concentrations as measured in the MOX test fuel and cladding.

2.1.1 Fuel

Residual gallium concentration was the primary variable of interest in the two fuel types produced at Los Alamos National Laboratory for the MOX test irradiation. One batch was fabricated from plutonium feed containing a nominal one weight percent gallium without special treatment for removal of impurities. The second batch was made with the same feed but processed with a PuO_2 powder thermal-conditioning step intended to remove the gallium. This Thermally Induced Gallium Removal (TIGR—Reference 2) treatment is a dry process for separating Ga_2O_3 in which the PuO_2 powder is exposed to a flowing mixture of argon and (6%) hydrogen at about 1200°C. Under these conditions, the Ga_2O_3 is reduced to the volatile Ga_2O, which evolves from the dry powder and is collected downstream. In addition to removing most of the gallium, the TIGR processing served to coarsen the powder, increasing the PuO_2 particle size and reducing the specific surface area.

The variations in the gallium concentrations through the fuel preparation processes are shown in Table 2.1.

Table 2.1. Reduction in gallium content during pellet preparation

Preparation step	Gallium concentration (ppm)	
	With thermal treatment (TIGR)	Untreated
Plutonium metal	10,000	10,000
PuO_2 powder	~8,800	~8,800
PuO_2 powder post-treatment	~170	—
MOX powder blend	~8.5	~440
Sintered MOX pellet (Ref. 3)	0.77–1.89	0.95–4.99

The gallium concentration was reduced from 10,000 to 8,800 ppm when the plutonium metal was oxidized. For the TIGR-treated case, the treatment further reduced this concentration to about 170 ppm before the powder was diluted (blended with UO_2). Since the final MOX blend is 5% by weight, the dilution factor is 20, producing a final blend gallium concentration of about 8.5 ppm. For the untreated powder, the blending with UO_2 reduced the gallium concentration to about 440 ppm. In both cases, almost all of the remaining gallium was driven off when the pellets were sintered. (Liquid gallium deposits were subsequently removed from the sintering furnace walls.) Thus, use of the TIGR process produced very little change in the gallium contents of the finished pellets.

The gallium analyses performed at the ORNL Radioactive Materials Analysis Laboratory (RMAL) for ten unirradiated pellets from each MOX test fuel pellet batch are described in Reference 3. With the mass spectrometer, the presence of gallium is clearly indicated by a two-component set of activity lines at the stable isotope masses 69 (60.1% abundance) and 71 (39.9% abundance). In addition, the abundance ratio (60.1 to 39.9) serves as a check that the stable gallium isotopes are indeed the sources of the lines observed.

The measured gallium levels range from 1.09 to 2.03 ppm for the TIGR-treated batch with an average of 1.33 and a standard deviation of 0.28. For the untreated batch, the measured values range from 1.81 to 4.78 ppm with an average of 2.97 and a standard deviation of 1.01.

2.1.2 Cladding

The gallium contents of 14 samples of unirradiated cladding material archived from the MOX test fuel pins were determined in conjunction with the 30 GWd/MT PIE (Section 6.2 of Reference 4). The measured gallium concentrations range from 0.556 to 0.674 ppm, with an average value of 0.589 ppm (standard deviation 0.028 ppm). Further, samples of the stainless steel spring used to axially load the pellet stack within the fuel pin were found to contain about 34.0 ppm gallium. These results were surprising because gallium was not expected to be present in fuel pin structural materials beyond trace quantities.

Subsequent to these results for the MOX test fuel cladding, Framatome Advanced Nuclear Power, Inc. (ANP) provided six archive cladding samples from fuel they had produced between 1990 and 1994 for analyses at the RMAL. The average gallium content for these claddings was 0.275 ppm. Nine stainless steel fuel rod plenum spring material samples also provided at this time were found to have an average gallium concentration of 38.0 ppm.

2.2 Gallium in Irradiated Fuel

As discussed in the previous section, initial gallium levels in the MOX test fuels were measured from 1.8 to 4.8 ppm in the untreated fuel and from 1.1 to 2.0 ppm for the TIGR-treated fuel. Gallium measurements during the successive PIEs for irradiated pellets of both fuel types (untreated and TIGR) have indicated the expected pellet-to-pellet variations but no reduction in overall fuel gallium content.

2.3 Gallium in Irradiated Cladding

Each successive PIE included gallium content analyses for cladding segments from both the TIGR-treated and untreated fuel pins. The purpose was to determine if gallium was migrating from the fuel to the cladding, a major investigative object of this MOX test irradiation. The baseline comprised the gallium contents measured for archived unirradiated specimens of the identical cladding.

Resolution of gallium in unirradiated cladding is not difficult; concentrations were measured as approximately 0.59 ppm. Gallium measurements in irradiated cladding are more difficult because barium, a fission product, can become doubly ionized in the mass spectrometer and mimic gallium. Particularly at the small gallium levels present in the MOX test specimens, this complicates quantifying the measurement. Chemical separation steps were necessary to obtain a reliable mass spectrometer signal. Analytical uncertainties are estimated to be about 30%.

Comparisons of the measured gallium concentrations in the irradiated cladding with those of the unirradiated material indicate no significant change.

2.4 Stability of Gallium

Unirradiated MOX test fuel components showed gallium concentrations in the range from 1–5 ppm in the fuel and 0.3 to 0.6 ppm in the cladding. If all of the gallium in the fuel were transferred radially outward, the cladding concentration would increase to about 9 ppm. As part of each PIE, samples of irradiated fuel and cladding were sent to the RMAL for determination of the gallium contents. None of the cladding samples has shown any increase over the preirradiation gallium concentrations. Correspondingly, there has been no evidence of any attack of the inner cladding surface. Finally, each fuel sample has indicated, within the limits of analytical accuracy, that the gallium initially present has been retained. It is concluded that any migration of gallium from fuel to cladding is insignificant and presents no credible threat to the cladding integrity.

3. FISSION GAS RELEASE (FGR) WITH COMPARISON TO EUROPEAN EXPERIENCE

This chapter addresses the fission gas release (FGR) determinations for the MOX test fuel pins. The method depends upon measurement of the ^{85}Kr activity within the fuel pin free volume. To obtain this measurement, each capsule was mounted vertically with the upper end cap trimmed to reduce the path length into the capsule upper plenum. The vacuum-sealed drill press apparatus described in Reference 5 was then employed to drill downward through the capsule upper end cap. After recording the capsule pressure and any krypton activity (none was ever found), the drill was advanced through the fuel pin upper end cap to permit measurement of the pressure and krypton activity in the pin upper plenum and connected free volume. As described in Section 3.1, the fission gas release fraction is the ^{85}Kr activity in the gas collected from the fuel pin divided by the total activity of this isotope within the pin. Section 3.2 describes how this release fraction is checked by use of the pin pressure before drilling as derived from the pressure measured (post-drilling) for the combined fuel pin and collection chamber. The implications of the release fractions as determined for the various fuel pins are discussed in Section 3.3.

3.1 FGR Per Krypton-85 Activity Ratio

Krypton-85 is a reliable FGR marker because it is created within the fuel only by fission and has a half-life sufficiently long (about ten years) to make quantitative measurements practical. The total krypton activity present in the fuel pin as a function of time after shutdown is obtained via the ORIGEN code runs conducted at Idaho National Laboratory (INL) pursuant to each capsule withdrawal. This total (as of the time that the fuel pin was opened) is then divided into the activity measured in the gas collected from the pin free volume. The resulting gas release ratio of ^{85}Kr is then a good approximation (Reference 6) to the overall fission gas release fraction.

The FGR percentages as determined for the MOX test fuel pins are listed in Table 3.1. These are considered accurate to within ±8% of the listed values.

Table 3.1. Fission gas release percentages for the MOX test fuel pins as derived from measured ^{85}Kr activities

Parameter	21 GWd/MT withdrawal		30 GWd/MT withdrawal		40 GWd/MT withdrawal		50 GWd/MT withdrawal		
Capsule number	2	9	3	10	4	13	6	12	5
Fuel pin number	5	12	6	13	7	16	9	15	8
Measured fuel pin pressure (psia)	20.3	23.6	26.7	33.2	114.8	134.8	148.4	177.9	70.3
^{85}Kr activity (mCi) Collected Total created	 3.78 287	 5.37 286	 5.65 385	 9.01 391	 39.6 473	 44.8 471	 40.4 559	 48.6 564	 16.5 534
Implied fission gas release (%)	1.32	1.88	1.47	2.30	8.37	9.51	7.23	8.61	3.09

3.2 FGR Check Per Measured Fuel Pin Pressure

The free volume gas inventory is the sum of the helium initially loaded plus the released portions of the fission gases (krypton and xenon) and of the helium created within the fuel during and after irradiation. [Other gases may be present in trace (negligible) quantities.] Knowledge of the fuel pin free volume and its gas content permits use of the perfect gas law to find the corresponding pin total pressure. This can

then be compared with the measured fuel pin pressure. Following a discussion of the fuel pin helium inventories, an example calculation is provided to demonstrate the check methodology for Fuel Pin 8.

3.2.1 Helium Generation and Release

Gas releases collected from the MOX test fuel pins include significant quantities of helium. This helium derives from two primary sources, as discussed in the following subsections.

3.2.1.1 Helium—initially loaded

Much of the helium found in the MOX test fuel pins is the initial charge introduced at atmospheric pressure when the upper end caps were welded closed at Los Alamos National Laboratory (LANL). The pressure exerted by this helium fill gas during capsule irradiation was considered in the Safety Analyses for this test irradiation as discussed in Reference 7. Applying the perfect gas law with the estimated LANL glove box atmosphere conditions (11.1 psia; 80°F), approximately 4 E-5 mole helium was loaded into each fuel pin's initial free volume of about 1.3 cm^3. Table 3.2 provides as-fabricated values for the three capsules that attained the highest burnups.

Table 3.2. Initial helium fills for capsules withdrawn at 50 GWd/MT

Capsule	Fuel Pin	Initial free volumes (cm^3)	Helium fill (gram-mole)
5	8	1.318	4.047E-5
6	9	1.300	3.992E-5
12	15	1.326	4.071E-5

3.2.1.2 Helium created during and after irradiation

The second primary source for the helium present when the fuel pin free volumes are opened is by creation within the fuel during and after irradiation. Most of the helium created within the fuel derives via alpha decay of the higher mass-number elements formed by successive transmutation of plutonium. Other sources, such as alpha particles formed by ternary fission and (n, alpha) reactions between O-16 and fast neutrons, are relatively small. The helium created within the fuel is subject to diffusion and subsequent release from the fuel matrix. Information concerning the production and potential for release of this created helium is available in References 8 through 11.

Curium-242 is the major (90%) contributor to helium production by alpha decay. Its prominence derives from its half-life of 163 days, which is short relative to the half-lives of the competing transuranic elements. Because the transmutation chain to ^{242}Cm is shorter when plutonium is irradiated, the helium production rate in MOX fuel is about four times the rate in UO_2 (Reference 10). Table 3.3 lists the helium inventories created within the MOX test fuel as predicted by the ORIGEN calculations performed at INL.

Table 3.3. Created helium inventories at shutdown and 120 days thereafter

Capsules	Withdrawal		Created helium (gram-moles × 10^{-5})	
	Burnup (GWd/MT)	Exposure (EFPDs)	At-shutdown	Shutdown + 120 days
2 and 9	21.0	383	1.10	1.44
3 and 10	30.2	615	2.32	2.77
4 and 13	39.8	904	4.92	5.82
6 and 12	50.1	1307	11.31	11.98
5	49.5	1462	11.97	12.66

As indicated, the inventory of created helium increases exponentially with burnup. For the capsules withdrawn at 50 GWd/MT, Table 3.4 provides the amount of created helium in each fuel pin at the time the fuel pin was drilled and the gas collected.

Table 3.4. Created helium in 50-GWd/MT fuel pins at time of opening

Capsule	Fuel Pin	Date drilled	Time after shutdown (days)	Created helium (gram-mole)
12	15	10/13/04	178	12.25E-5
6	9	10/27/04	192	12.27E-5
5	8	11/10/04	206	12.99E-5

Some of this created helium was released into the pin free volume, where it joined the approximately 4×10^{-5} gram-moles initially present when the pins were sealed.

3.2.1.3 Helium release during and after irradiation

In general, release of the helium created within the fuel matrix is negligible in commercial pressurized water reactor (PWR) fuel due to the high partial pressure [25 bar (360 psia) cold] exerted by the initially charged helium in the fuel pin free volume. On the contrary, it is more probable that some of the initial fill gas will be absorbed or taken up within the PWR fuel matrix. Helium release is expected, however, for design conditions such as employed for the MOX test fuel pins, where the initial helium charge was inserted at atmospheric pressure. Literature for helium release under these conditions is limited, but available results (References 10 and 11) indicate helium release fractions 3–5 times the fission gas release fraction.

The mechanisms for helium release from fuel are discussed in Reference 10. Although helium diffuses about 30 times faster than xenon, diffusion to the pin free volume is not the major factor in helium release, primarily because of the long path lengths involved. Rather than migrating directly to a free volume boundary, it is more likely that the diffusing helium will intersect and coalesce with the existing fission gas bubbles located within the matrix and along the internal grain boundaries. In general, faster-moving helium atoms reach and reside within porosity originally occupied by the fission gases alone. Most of the created helium becomes mixed with the fission gas in these bubbles and subsequently follows the same release pathways. Thus, the release of helium to the pin free volume is observed to be proportional to the fission gas release and to exhibit the same initiation threshold. For the experiments cited in Reference 10, the helium release (40%) from fuel was five times greater than the fission gas release (8%).

The helium mole fractions in the gas collections from the fuel pin free volumes were measured as part of the 50 GWd/MT PIEs. From these, the helium release fractions can easily be calculated. As an example for Fuel Pin 8 (Capsule 5), the helium mole fraction was 0.236, while the pin pressure and free volume were 0.485 MPa (70.3 psia) and 1.2163 cm^3. Using the perfect gas law with a gas temperature of 308.8 K (96°F), the total fuel pin gas inventory was 22.96E-5 mole. Thus, the helium constituent is

$$0.236 \times 22.96\text{E-}5 = 5.425\text{E-}5 \text{ mole} \ .$$

The initial helium inventory for Fuel Pin 8 was 4.047E-5 mole (Table 3.2). The created and released helium content is then

$$5.425\text{E-}5 - 4.047\text{E-}5 = 1.38\text{E-}5 \text{ mole} \ .$$

With 12.99E-5 helium moles created as of the date the fuel pin was opened (Table 3.4), the helium release fraction is

$$1.38/12.99 = 0.106 \ .$$

This is 3.4 times the fission gas release fraction for this fuel pin as measured by ^{85}Kr activity.

3.2.2 Fission Gas and Helium in Pin Free Volume

The amount of fission gas created is obtained from the ORIGEN runs performed at INL. Multiplying by the fission gas release fraction then yields the fission gas inventory in the fuel pin free volume. For Fuel Pin 8, the calculated fission gas generation (krypton plus xenon) at the time the pin was opened is 520.73E-5 mole. With a fission gas release fraction of 0.031 (Table 3.1), the fission gas inventory in the fuel pin free volume is 16.14E-5 mole. This is listed as item (c) in Table 3.5.

As discussed in the previous section, the gas constituents collected from the 50-GWd/MT fuel pins were identified and quantified by mass spectrometer. The helium mole fraction of 0.236 for Fuel Pin 8 is entered as item (d) in Table 3.5, with an uncertainty range of ±5%.

Table. 3.5. Fuel Pin 8 pressure calculation based on fission gas release fraction derived from ^{85}Kr activity measurement

Parameter	Value	Uncertainty or range
(a) Fission gas release fraction	0.031	—
(b) Fission gas created ($\times 10^{-5}$)	520.73 mole	None assumed
(c) Fission gas in free volume ($\times 10^{-5}$)	16.14 mole	—
(d) Helium mole fraction in free volume	0.236	0.224–0.248
(e) Total free volume gas ($\times 10^{-5}$)	21.13 mole	20.81–21.47 mole
(f) Fuel pin free volume	1.216 cm^3	±2.29%
(g) Gas temperature	308.8 K	±1.60%
(h) Calculated pressure	0.4461 MPa (64.7 psia)	0.4225–0.4713 MPa (61.3–68.4 psia)
(i) Measured pressure	0.4847 MPa (70.3 psia)	0.4604–0.5089 MPa (66.8–73.8 psia)

3.2.3 Total Fuel Pin Free Volume Gas Inventory

With the assumption that other gases are limited to trace (negligible) quantities, the total gas inventory within Fuel Pin 8 can now be calculated. Adjusting for the helium content, the 16.14 moles of fission gas [Table 3.5, item (c)] constitute (1.0–0.236) or 0.764 of the total gas moles. The total free volume gas inventory is therefore

$$16.14/0.764 = 21.13 \text{ mole} \ ,$$

which is entered in Table 3.5 as item (e). The associated range corresponds directly to the range of values for the helium mole fraction [item (d)].

3.2.4 Measured and Calculated Fuel Pin Pressure

The fuel pin 8 free volume [item (f) in Table 3.5] was measured by gas backfill as described in Volume 1. The measured volume of 1.216 cm^3 agrees well with the volume calculated by use of the CARTS and FRAPCON codes and is considered accurate within 2.3%.

The effective temperature of the gas at the time Fuel Pin 8 was opened is taken from the CARTS calculation as 96.1°F ± 9°F, which corresponds to 308.8K with an uncertainty of 1.6%, entered as item (g) in Table 3.5. This temperature and the fuel pin free volume are utilized with the perfect gas law to calculate the expected gas pressure corresponding to the free volume gas content (moles fission gas plus helium).

Table 3.5, items (e) through (g) list the parameters for the perfect gas law calculation for Fuel Pin 8. The result [item (h)] is 0.4461 MPa (64.7 psi). The uncertainty range associated with this value overlaps the measured pressure and associated uncertainty listed as item (i).

3.2.5 Assessment: FGR Fraction Determination and Check

Gas release fractions were determined by measurement of ^{85}Kr activity at the time when each fuel pin was opened. A check was provided by simultaneous measurement of total gas pressure, which could then be compared with the expected (calculated) pressure based on the fission gas release fraction as derived from ^{85}Kr activity. For example, comparison of items (h) and (i) in Table 3.5 provides a satisfactory check. Use of this method provided an acceptable check for all of the fuel pins for which fission gas release fractions were determined (those listed in Table 3.1).

It should be noted, however, that direct measurement of the helium mole fraction was only employed for the 50-GWd/MT withdrawals. For the earlier PIEs, the amount of created helium was much less (see Table 3.3), and a satisfactory check could be obtained simply by making very broad assumptions for the release range. For example, the helium release was assumed to lie in the range from 25% to 75% for the 40-GWd/MT withdrawals. (An indisputable range from 0 to 100% release was used in the earlier PIEs.)

3.2.6 Independent Calculation of FGR Fraction

Since fuel pin pressure is proportional to the fission gas release fraction, it is easy to conclude from the parameter values listed in Table 3.5 that the calculated pressure will match the pressure measured for Fuel Pin 8 if the fission gas release fraction is 0.037. This illustrates the point that a fission gas release fraction completely independent of the ^{85}Kr activity measurements can be obtained when the constituent mole fractions are determined by mass spectrometer, as was done for the 50-GWd/MT withdrawals (only).

Specifically, Table 3.5 [items (i) measured pressure, (g) gas temperature, and (f) fuel pin free volume] can be used with the perfect gas law to obtain the total number of gas moles. Multiplication by the fission gas mole fraction yields the number of fission gas moles. Division by the fission gas moles created [Table 3.5, item (b)] then produces the release fraction. Table 3.6 lists the results for the 50-GWd/MT fuel pins.

Comparison of the entries in the last two rows of Table 3.6 indicates that the agreements between these two independent methods of determining fission gas release fractions are quite good.

Table 3.6. Fission gas release fractions for 50-GWd/MT fuel pins as determined by measured pressure/mole fractions and by ^{85}Kr activity ratio

Parameter	Fuel Pin		
	8	9	15
(a) Measured pressure, psia	70.3	148.4	177.9
(b) Total gas moles ($\times 10^{-4}$)	2.296	4.787	5.718
(c) Fission gas mole fraction	0.7637	0.7962	0.8655
(d) Moles fission gas in free volume ($\times 10^{-4}$)	1.754	3.811	4.949
(e) Moles fission gas created ($\times 10^{-4}$)	52.07	53.40	53.63
(f) Fission gas release fraction	0.0337	0.0717	0.0922
(g) Krypton-85 activity ratio	0.0309	0.0723	0.0861

3.3 Implications of the Fuel Pin FGR Fractions

Fission gas release fractions are estimated within a reasonable uncertainty (±8%) for the MOX test fuel pins by measurement of the ^{85}Kr activity in the gas collected from the fuel pin free volume. The fission gas release percentages determined for the MOX test fuel pins withdrawn at burnups of 21, 30, 40, and 50 GWd/MT are listed in Table 3.1. The corresponding release fractions for the 21- and 30-GWd/MT withdrawals range from 0.0132 to 0.0230. These four fuel pins occupied symmetric positions with respect to the ATR core during the irradiation and have similar temperature histories through the end of Phase II. Thus, it is not surprising that the fission gas release fractions for these four pins should fall within this narrow a range.

The fission gas release fractions for the two fuel pins withdrawn at 40 GWd/MT are four to five times higher. Fuel Pins 7 and 16 occupied symmetric test assembly positions throughout the irradiation and have release fractions of 0.084 and 0.095, respectively. These higher release fractions are attributed to the much higher LHGRs (and fuel temperatures) that these pins encountered. Between the two pins, the LHGRs for Fuel Pin 16 were slightly higher than those for Pin 7. However, other factors probably contribute to the difference between the Pin 16 and Pin 7 fission gas release fractions.

3.3.1 Higher Gas Releases for TIGR-Treated Fuel

It should be noted from Table 3.1 that Fuel Pins 12, 13, 16, and 15 all have higher fission gas release fractions than their symmetrically-placed counterparts 5, 6, 7, and 9. The PuO_2 powder for Fuel Pin 12, 13, 15, and 16 was subjected to the TIGR process (Reference 2) so that most of the gallium was removed before pellet sintering. The average gallium content of fuel in these pins is about 1.3 ppm. Fuel Pins 5–7, and 9 were prepared with untreated PuO_2 powder, so most of the gallium was driven off during pellet sintering, leaving an average gallium content of about 3.0 ppm.

While carrying out its primary purpose of gallium removal, the TIGR process also affects the powder (and pellet) morphology. As discussed in Reference 2, TIGR treatment at the temperatures (about 1200°C) for which it is effective tends to increase the particle size while greatly reducing the specific powder surface area. It is certainly plausible that these presintering changes in particle characteristics have contributed to the observed differences in fission gas release fractions between the TIGR-treated and the untreated MOX fuels. As discussed in Chapter 4, the TIGR-treated fuel is noticeably more friable at the higher burnups.

3.3.2 Comparison to the European Experience

Figure 3.1, which is adapted from Reference 12, displays literature values for fission gas release of European commercial test fuels plotted against the corresponding average LHGRs during the second irradiation cycle. This figure also presents, in the upper left hand corner, a bar chart indicating the relative axial powers (LHGRs) typically encountered during each of the three irradiation cycles.

The blue portions of the bar chart illustrate the ranges within which LHGRs are typically experienced by European commercial fuel during the first, second, and third irradiation cycles. In general, the LHGRs increase somewhat in advancing from the first to the second cycle, and, in all cases, decrease in proceeding from the second to the third cycle. It is important to understand that the highest powers are experienced during the second irradiation cycle. This is why the average LHGR during the second irradiation cycle has been chosen as the abscissa parameter for the fission gas release plot of Figure 3.1. (The exception is those cases where the fuel was irradiated for just one cycle—for these, the fission gas is plotted against the average LHGR during that single cycle.)

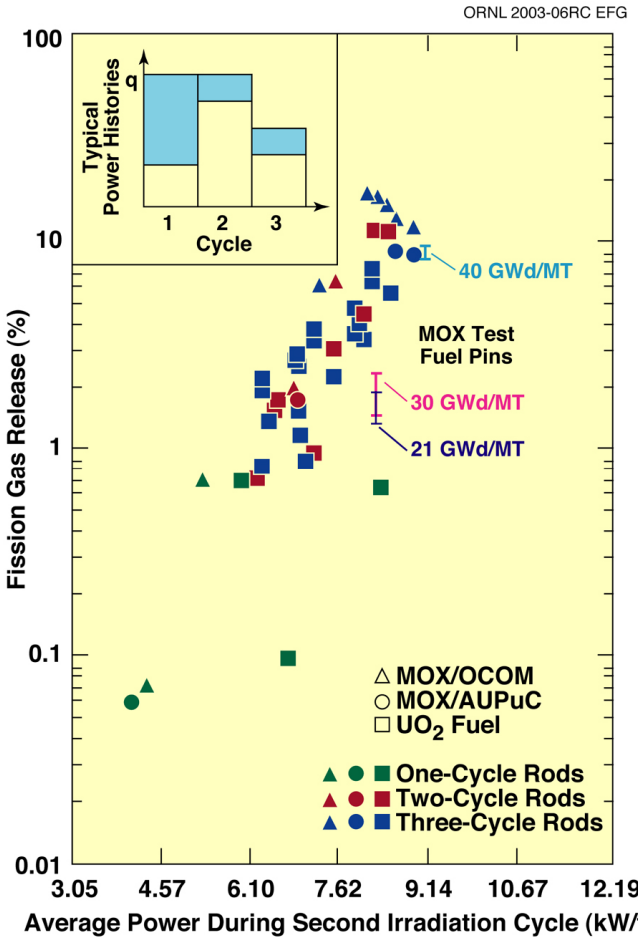

Fig. 3.1. The MOX test fuel pins exhibit gas release fractions proportional to their linear heat generation rate experience.
Source: Basic plot is taken from Reference 12.

Since fuel temperatures are proportional to LHGRs, the points plotted in Figure 3.1 also represent the linear relation (on a logarithmic scale) between the accumulated gas release at the end of the irradiation and the temperatures experienced by the fuel during the second cycle of the irradiation. This indicates that it is the highest temperature ever experienced by the fuel (which occurs during the second irradiation cycle) that primarily determines the fission gas release fraction, not the extent of the accumulated burnup. (The amount of gas available for release does, of course, increase directly in proportion to burnup.)

Superimposed on the plot of Figure 3.1 are the implied fission gas release fractions (Table 3.1) as obtained by the ^{85}Kr activity measurements for the 21-, 30-, and 40-GWd/MT withdrawals of the MOX test irradiation. (The 50-GWd/MT withdrawals are discussed in the following section.) The abscissa values for these release fractions are the average LHGRs experienced by the test fuels during Phase II of the irradiation. The ranges extend between the implied fission gas release fractions determined for the TIGR-treated and untreated fuels.

As discussed previously, all four of the 21-GWd/MT and 30-GWd/MT "MOX Test Fuel Pins" represented on Figure 3.1 were symmetrically loaded within the test assembly and had similar irradiation histories. Fuel pin-average LHGRs increased from 7.98 kW/ft for Phase I to 8.21 kW/ft for Phase II and then (30-GWd/MT pins only) fell to 5.48 kW/ft for Phase III. The highest LHGR for these pins was 9.7 kW/ft at the beginning of Phase II. Although burnup increased by almost half for the 30-GWd/MT withdrawals, the fission gas release fractions were very nearly the same as for the 21-GWd/MT pins.

The fuel pins withdrawn at 40 GWd/MT experienced higher LHGRs (and temperatures) during their irradiations and hence exhibit much higher fission gas release fractions, as shown on Figure 3.1. These two pins, with similar irradiation histories by virtue of their symmetric test assembly loadings, achieved average LHGRs during Phase II of about 9.1 kW/ft, with a maximum of about 10.7 kW/ft. These were the highest LHGRs experienced by any of the MOX test capsules.

Although greater than one percent in all cases, the fission gas releases for the weapons-derived MOX test fuel pins represented in Figure 3.1 are low in comparison with the European experience for mixed-oxide fuels with similar irradiation histories. Until about ten years ago, it was common practice to plot measured fission gas release percentages against the final burnups of the associated fuels. In general, this approach is characterized by wide scatter in the plotted points. Since about 1993 (with publication of Reference 12), it has become generally recognized that the fission gas release fraction has a much stronger dependence on the maximum temperature experienced by the fuel than on the accumulated burnup.

When fission gas release percentages are plotted against the highest LHGR experienced by the fuel, a linear relation is displayed, as on Figure 3.1. This means that the same fuel can be expected to have a lower fission gas release fraction at higher burnup, if the higher burnup is achieved with a lower maximum LHGR. This is indeed the case for the 50-GWd/MT withdrawals, as discussed in the following section.

3.3.3 FGR for the 50-GWd/MT Fuel Pins

Figure 3.2 is a replication of Figure 3.1, with the addition of fission gas release percentages for each of the three fuel pins irradiated to 50-GWd/MT burnup. These are Fuel Pins 9 and 15, irradiated in symmetric test assembly positions, and Fuel Pin 8, irradiated without a TIGR-treated counterpart. The plotted ranges extend between the fission gas release percentages as found by the two independent means employed for the 50-GWd/MT PIE—^{85}Kr activity ratio and measured pressure/mole fractions. For example, the range for Fuel Pin 15 extends from 9.22% to 8.61%, items (f) and (g) of Table 3.6, respectively.

Similar to the earlier withdrawals, the abscissa values for the 50-GWd/MT fuel pin representations are the average LHGRs experienced by the test fuels during Phase II of the irradiation. As discussed in Chapter 3 of Volume 1, Phase II was the first irradiation Phase for Fuel Pins 9 and 15. Reference to Phase II is appropriate nevertheless because the highest LHGRs were encountered here. Maximum LHGRs for Pins 9 and 15 were about 8.7 kW/ft at the beginning of the irradiation, with Phase II averages of about 7.7 kW/ft.

Fuel Pin 15 contained the TIGR-treated fuel which, as usual, exhibits (Figure 3.2) a higher fission gas release percentage than its untreated symmetrically-loaded counterpart. Of more interest is the observation that the fission gas release percentage is lower for Fuel Pin 9 and Fuel Pin 8 at 50 GWd/MT than for Fuel Pin 7 (also containing untreated fuel) at 40 GWd/MT.

Fuel Pin 8 had the lowest average LHGR during Phase II and hence appears farthest to the left of all MOX test fuel pins on Figure 3.2. It is important to note that at 50 GWd/MT, its range (3.09–3.37) is much lower than the fission gas release percentage (8.37) for Fuel Pin 7. This much lower gas release is directly attributed to its lower fuel temperature during the irradiation. For ease of comparison, the calculated fuel centerline temperature traces for Fuel Pins 7, 8, and 9 (only) are provided in Figure 3.3.

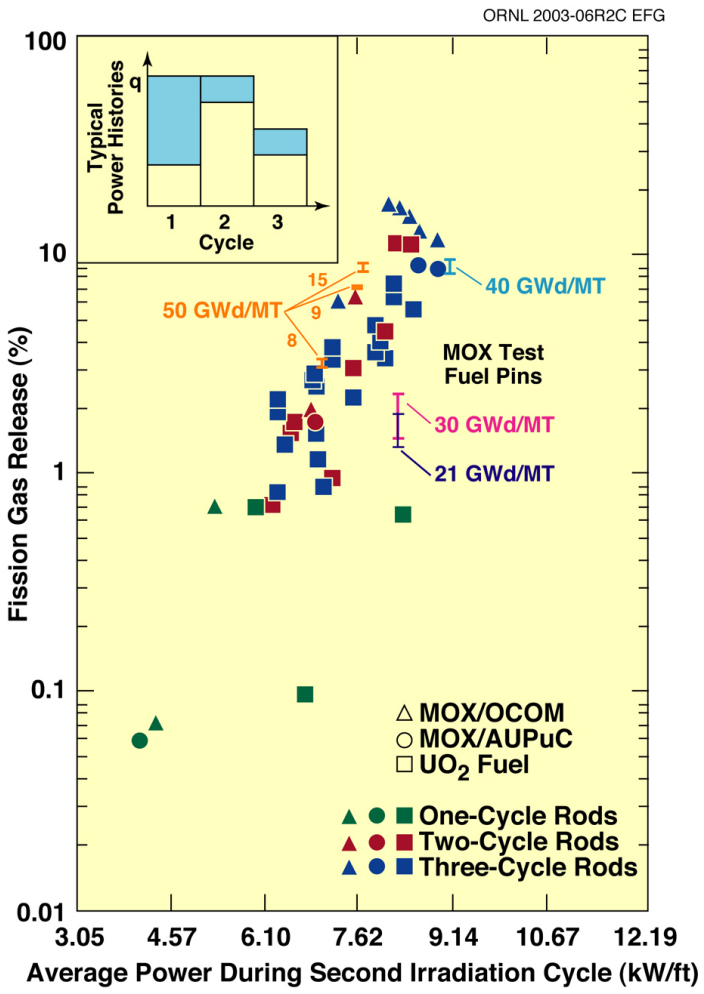

Fig. 3.2. Fission gas release ranges for Fuel Pins 8, 9, and 15 irradiated to 50 GWd/MT.

The point is sufficiently important to bear repeating. Both Fuel Pins 8 and 9, irradiated to 50 GWd/MT, exhibit lower fission gas release percentages than does Fuel Pin 7, irradiated to 40 GWd/MT. Figure 3.3 illustrates the lower fuel temperature traces associated with the two 50-GWd/MT pins. Of these, Fuel Pin 8 experienced lower fuel temperatures than Pin 9 and has a correspondingly lower gas release percentage. Thus, the effect of fuel temperature history in determining the fraction of fission gas released is amply demonstrated.

Finally, given that the fission gas releases exceed one percent for all fuel pins, it is of interest to compare the fuel temperatures with the Halden threshold to check if this is an expected result. The Halden Threshold, dating from 1979 and recently modified (lowered) for burnups greater than 22 GWd/MT, is an experimentally-derived curve of pellet centerline temperature vs burnup (discussed in Section 8.3.3). If a superimposed trace of predicted pellet centerline temperatures rises above this curve, then fission gas release fractions greater than 0.01 are to be expected. For the MOX test irradiation, the only fuel for which temperatures were not predicted to exceed the Halden threshold was that contained in Capsule 5 (Fuel Pin 8). Although Figure 3.2 confirms that the gas release percentage for Fuel Pin 8 is in line with the European experience for similar LHGRs, the fact remains that gas release exceeded one percent for a temperature trace that was not predicted to exceed the Halden threshold. The lesson learned with respect to the efficacy of the Halden threshold is discussed in conjunction with the post-PIE calculations for Capsule 5 as documented in Chapter 9.

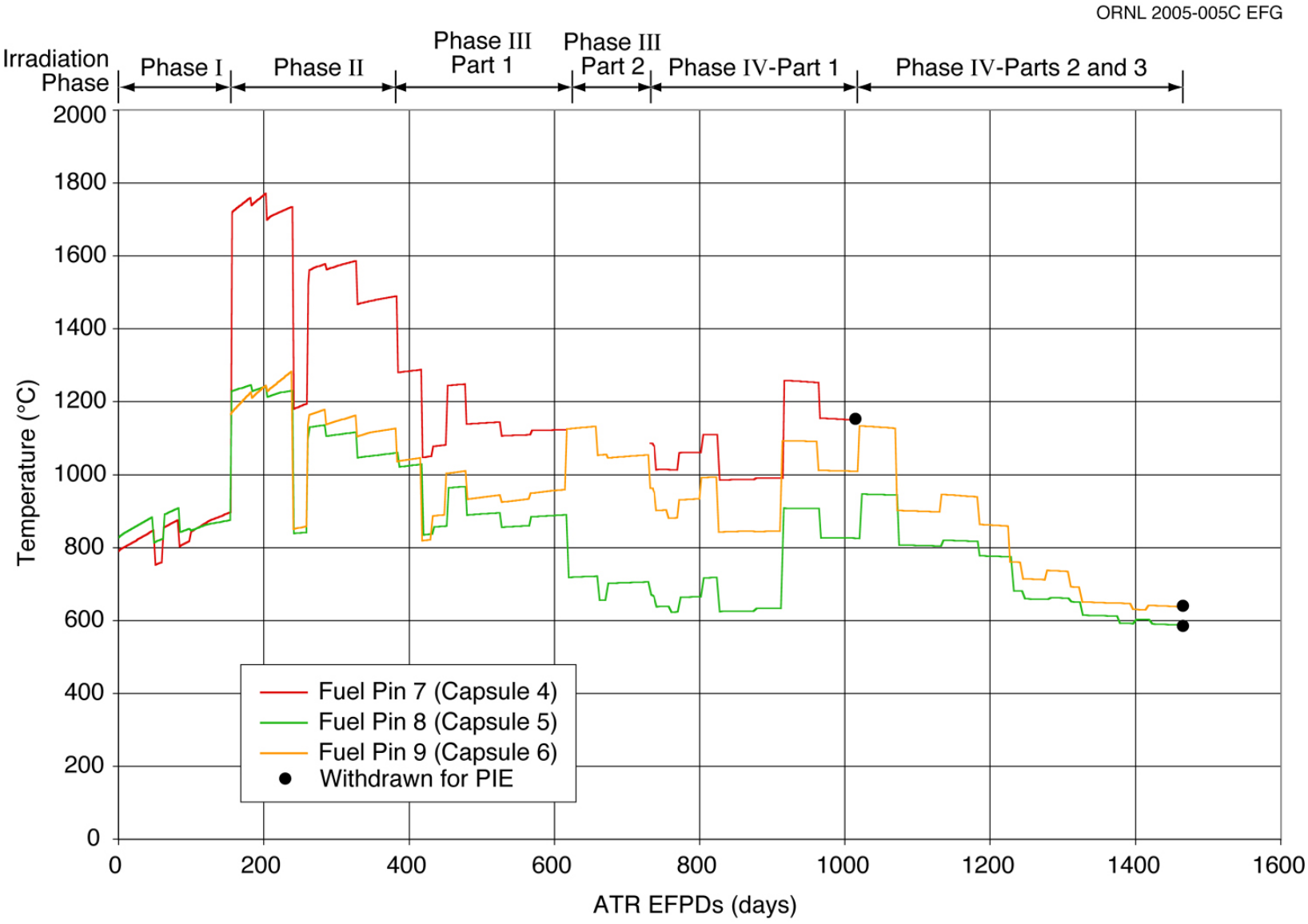

Fig. 3.3. Centerline temperature traces (as calculated by CARTS) for Fuel Pins 7, 8, and 9.

4. BEHAVIOR OF THE PLUTONIUM-RICH AGGLOMERATES

4.1 Introduction

This chapter addresses the plutonium-rich agglomerates in the MOX test fuel as observed for Fuel Pins 8, 9, and 15 (Capsules 5, 6, and 12). These three fuel pins had been irradiated to approximately 50 GWd/MT at the time of their withdrawal for PIE.

Following the Section 4.2 discussion of MOX fuel fabrication processes in general, Section 4.3 describes the structure of the weapons-derived MOX fuel that has been irradiated in the current test. The rationales found in the literature for placing limits on agglomerate size are discussed in Sections 4.4 (reprocessing) and 4.5 (reactivity insertion accidents). Examples of initial agglomerate size specifications proposed for application to MOX fuels for U.S. reactors (including the current test irradiation) are provided in Section 4.6.

The manner in which the structure of the plutonium-rich agglomerates changes with burnup is discussed in Section 4.7. Agglomerate restructuring effects upon fission gas retention are described in Section 4.8. Section 4.9 summarizes the agglomerate distributions and size as observed in the 50-GWd/MT PIE. Finally, Section 4.10 provides a synopsis of the main points and the conclusions of this chapter.

4.2 Background—MOX Fuel

The earliest method for producing MOX fuel was to obtain the desired fissile plutonium concentration by directly comilling the PuO_2 and UO_2 powders. The resulting fuel is heterogeneous, with the PuO_2 particles everywhere completely distinct from the UO_2. This "reference" process was used until about 1985, when it was generally abandoned due to inadequate solubility in nitric acid and the undesirable impact of this characteristic upon fuel reprocessing.

Several methods to improve the homogeneity of MOX fuels have been developed during the last two decades, including the Short Binderless Route (SBR) in England, the Optimized Co-Milling (OCOM) in Germany, and the MIcronized MASter blend (MIMAS) process in Belgium and France. The MOX fuel irradiated in the current test was prepared at Los Alamos National Laboratory (LANL) in a manner similar to the MIMAS process.

As explained in Reference 13, the MIMAS process is predicated on use of a master-mix combining all of the PuO_2 with a small fraction of the UO_2. These two components are milled together for several hours to develop an intimate mixing. The milling also modifies the physical characteristics of these powders. The comminution leads to self-agglomeration due to electrostatic forces, thereby producing agglomerates that although rich in plutonium, are not pure PuO_2. After sieving, the master-mix is blended with the remainder of the UO_2 to form the secondary blend, from which the pellets are pressed.

The fuel microstructure is influenced by the characteristics of the UO_2 powder, which determines both the porosity distribution and the master-mix distribution in the matrix (Reference 14). Pore size and distribution are affected in MIMAS by a proprietary pore-forming additive.

It is important to recognize that only a small portion of the UO_2 (that in the master-mix) undergoes milling in MIMAS. The physical characteristics (especially flowability) of the UO_2 powder introduced to surround the PuO_2-rich agglomerates in the secondary blend are not altered by milling. Thus, a free-flowing press feed for automated die fill is preserved.

European commercial fuels typically contain about 5 weight percent plutonium and comprise master-mix particles (plutonium-rich agglomerates with an average size <50 micron and 95% of the particle size <100 micron) regularly dispersed in the UO_2 matrix. Some larger particles, up to 200 microns can be found, irregularly dispersed in the UO_2 matrix (Reference 15). The microstructure produced by the master-mix process differs from the dual structure of a simple (pure PuO_2 particles embedded in a UO_2 matrix) mixture because the initial master-mix, typically prepared by milling a 30%–70% PuO_2/UO_2 powder combination, is diluted into a much larger (fivefold by mass) UO_2 matrix. Thus, the structure is more homogeneous since the plutonium content of the agglomerates is no more than 30%.

4.3 Structure of the MOX Test Fuel

The MOX fuel for this test irradiation was fabricated at LANL during 1997. The weapons-derived PuO_2 feedstock was obtained from Lawrence Livermore National Laboratory (LLNL). The baseline dry pyroprocess used at LLNL to convert the weapons components into the feed oxide powder was the three-step Hydrogen Oxidation (HYDOX) developed (Reference 16) by the Advanced Recovery and Integrated Extraction System (ARIES) project. This process avoids the simultaneous use of hydrogen and oxygen.

For the HYDOX metal-to-oxide conversion, plutonium metal is subjected to hydrogen diluted in an inert carrier gas. Unreacted metal is continuously exposed as plutonium hydride spalls from the surface. The plutonium hydride is collected and subsequently exposed to nitrogen gas, converting to plutonium nitride. The plutonium nitride is then oxidized through exposure to oxygen diluted in an inert carrier.

At Los Alamos, half of the weapons-derived PuO_2 feed received from LLNL was subjected to the TIGR treatment as described in Section 2.1.1. In addition to removing much of the gallium, the TIGR processing served to coarsen the powder, increasing the PuO_2 particle size and reducing the specific surface area.

The two PuO_2 powders (TIGR-treated and untreated) were milled with depleted UO_2 powder to form two separate master-mixes. The milling produced an intimate mixing, but also modified the powder physical characteristics (surface area, density, flowability), while electrostatic forces induced self-agglomeration. Each master-mix was then blended (not milled) into a much larger quantity of pure UO_2 powder to form a secondary blend, from which a pellet set was pressed. Thus, the two mixed-oxide test fuels differ only as to whether the PuO_2 in the master-mix was TIGR-treated or not.

Both MOX test fuels comprise 5% PuO_2 and 95% depleted UO_2, the latter converted by the ammonium diuranate (ADU) process. In each case, all of the PuO_2 was introduced as 31% of the master-mix. Stated another way to provide a better feel for the numbers, each 100 grams of MOX test fuel includes 5 grams of PuO_2 and 11.11 grams of UO_2 that were milled together to form the master-mix. The milling reduced the PuO_2 and UO_2 particle size while promoting a homogeneous dispersion of the PuO_2 particles in the UO_2. Employing a mixer/blender that does not alter particle characteristics (as does milling), these 16.11 grams of master-mix were then diluted and dispersed into the remaining 83.89 grams of depleted UO_2.

The plutonium-rich agglomerates are in essence clumps of master-mix. Most are very small, with equivalent diameters well below 100 microns. Nevertheless, the secondary blending (dilution) processes by which each master-mix was distributed into the matrix of depleted UO_2 were less effective than intended, in the sense that a few residual clumps (agglomerates) of the master-mix remained intact with equivalent diameters of more than 200 microns within the final blend.

It is of interest to compare the MOX test fuel with the MOX fuel currently fabricated for commercial purposes in European reactors by master-mix processes such as MIMAS or OCOM. The MOX test fuel

was fabricated with a MIMAS-type approach, in that a master-mix was prepared and then diluted into a secondary blend. However, there are important differences (Reference 17) in regard to the MOX test fuel used in this program. The depleted UO_2 was not of the free-flowing kind employed in the MIMAS process, the pore-forming additive was not employed, the mill and mixer were not of the same vintage as used in Europe, and the master blend was not sieved. Milling and mixing parameters were not the same as normally used with MIMAS because these were not known at LANL at the time the test fuel was made. Because of these differences, the MOX fuel prepared for this test irradiation project should not be considered as MIMAS mixed oxide, but rather as a test fuel fabricated with weapons-derived plutonium utilizing a MIMAS-type approach.

The plutonium concentration within the plutonium-rich agglomerates is higher than the MOX fuel average, but does not exceed that of the master-mix, which is 31%. Irradiation of the test fuel produces a heterogeneous fission distribution on a microscopic scale, with most fissions occurring within the agglomerates. The local burnup within the agglomerates is much higher than the average for the fuel, and internal accumulation of fission products (solids and gas) causes the agglomerates to swell against the constraining UO_2 matrix.

As burnup increases, the plutonium concentration within the agglomerates decreases because of depletion by fission and a limited diffusion into the surrounding matrix. Simultaneously, the plutonium concentration increases within the UO_2 matrix due both to creation by neutron capture in the ^{238}U nuclei and to a minor extent, diffusion from the agglomerates.

4.4 Rationales for Limiting Agglomerate Size

The two reasons most often cited in the literature for limiting the size of the plutonium-rich agglomerates are to facilitate dissolution during reprocessing and to reduce any detrimental effects that large agglomerate size may have with respect to increasing the release of fission product gases. The first of these will be discussed very briefly, since facility of reprocessing (fuel solubility) is not among the goals of the FMDP mission.

Reference 12 reports with respect to Siemens fuel that

> The irradiation experience of fuel assemblies with the MOX fuel, designated a “former standard”… was excellent. However, this MOX fuel did not satisfy reprocessing requirements, such as complete solubility of plutonium in pure nitric acid (>99%). This led to the development of new MOX powder preparation processes: the ammonium uranyl plutonyl carbonate (AuPuC) and optimized co-milling (OCOM) processes, which yield pellets with better plutonium solubility in pure nitric acid…

Similarly, Reference 13 (Chapter 5, Section 1.3.3) reports the French and Belgian experience:

> Up to 1985, the ‘reference’ process used (BELGONUCLEAIRE process) consisted of a direct PuO_2–UO_2 blend by comixing which resulted in a heterogeneous fuel (100% local PuO_2) … Fuel elements of this type have reached 50 GWd/tU+Pu …, but this process was abandoned because of reprocessing problems (bad solubility).
>
> The evolution of the ‘reference’ product led BELGONUCLEAIRE to the MIMAS process, which consists of the comilling of a mixture of PuO_2–UO_2 at 30% of maximum plutonium content, followed by a comixing of this first mixture with the UO_2 blend to obtain the nominal content …

> MIMAS MOX always keeps a certain plutonium distribution heterogeneity, nevertheless it is much improved compared to the 'reference MOX' (agglomerates at 30% of maximum plutonium content, size <100 micron).

In summary, although there were no performance problems with the early simple fuel mixtures, steps were taken to introduce a master-mix and to limit the size of the resulting plutonium-rich agglomerates in order to improve the solubility of the irradiated fuel for reprocessing purposes.

The second rationale for limiting agglomerate size, based on the supposition that large agglomerates may tend to increase fission gas release, is more pertinent to the current MOX test irradiation. Nevertheless, there has been no precise quantification of such an increase in European fuel (Reference 18), and Reference 15 reports no significant difference in fission gas release for two different agglomerate volume fractions and plutonium concentrations irradiated under the same conditions, or for different radial locations within the fuel. As for the current MOX test irradiation, although burnups have reached 50 GWd/MT and the agglomerates are large relative to those of modern European commercial fuel, there is no evidence of any detrimental effect upon fission gas release.

4.5 Large Agglomerate Effects in Reactivity Insertion Accidents (RIAs)

Transient power-burst tests to determine the effects of large pure PuO_2 microspheres were conducted at the SPERT reactor in 1969 and 1970. The following is taken from the "Summary and Conclusions" of the published results (Reference 19):

> Transient tests were conducted on nonirradiated oxide pellet-containing thermal recycle fuel pins at SPERT to investigate the possible effects of large single 550-μm-diam PuO_2 particles, which could possibly be present in the fabricated fuel, on the transient behavior. The results are compared with the results of similar tests conducted on pins containing enriched UO_2 and UO_2–PuO_2 pellet fuel that did not contain abnormally large PuO_2 particles.
>
> The results of these tests show that the effect of the large PuO_2 particles was to reduce slightly the cladding failure threshold energy … There were no indications of the effects of prompt fuel dispersal caused by the expulsion of the PuO_2 particles into the surrounding water when tested at these energy levels.
>
> Because the presence of single 550-μm-diam PuO_2 particles in mixed-oxide fuels does not appear to affect significantly the cladding failure threshold energy from that of mixed-oxide fuels with the normal PuO_2 particle size and distribution, product specifications that limit the maximum PuO_2 particle size to 550-μm diam do not appear warranted from the standpoint of transient fuel performance considerations. Specifications should be developed which limit the maximum PuO_2 particle size. These experiments have shown that such a limit is >550 μm diam.

It is important to recognize that the dimensions discussed in the SPERT results pertain to discrete PuO_2 particles, not to the overall size of plutonium-rich agglomerates. The more recent experiment described in Reference 20 also addresses the effects of pure PuO_2 particles in RIAs. Here, seven MOX test rods were prepared with PuO_2 particles of either 400 or 1100 μm equivalent diameter artificially embedded at one pellet surface. These rods were then subjected to rapid power bursts in the Nuclear Safety Research Reactor in Japan.

As described in Reference 20, "A PuO_2 particle located on the surface of a pellet can affect the failure threshold because a local peak of cladding temperature due to the particle can lead to fuel failure at lower energy disposition or the particle can act as a projectile moving at high velocity." What has not been established is the minimum particle size at which such effects occur. It is a conclusion of Reference 20 that "a PuO_2 particle up to 1100 μm on the surface of a pellet did not influence the failure behavior." It should be recognized that 1100 μm is a much greater equivalent diameter than is found in the largest of the plutonium-rich agglomerates of MOX fuels.

4.6 Technical Specifications: Plutonium-Rich Agglomerates

Pellet Technical Specifications normally include provisions with respect to plutonium-rich particles or agglomerate size. This section provides three examples of wording proposed for application to MOX fuel intended for irradiation in U.S. reactors.

4.6.1 American Society for Testing and Materials (ASTM)

The ASTM specification for mixed-oxide fuel (Reference 21) is as follows:

> The maximum equivalent diameter of plutonium-rich particles shall be less than 400 μm. The distribution of plutonium-rich particles shall satisfy either of the following requirements: (a) no more than 5% of the nominal PuO_2 shall be present in plutonium-rich particles with equivalent diameters of 200 μm or greater, or (b) no more than 5% of the plutonium-rich particles shall be greater than 100 μm in diameter and the average diameter of plutonium-rich particles will be less than 50 μm.

It should be noted that this draft specification is intended for "finished sintered (uranium-plutonium) dioxide pellets for use in thermal reactors" and "applies to uranium-plutonium dioxide pellets containing plutonium additions up to 15% by weight."

4.6.2 Framatome Technologies

Reference 22 includes the "plutonium-rich particle size" specification for the Fissile Materials Disposition Program mission fuel as follows:

> At least 95% of the plutonium-rich particles shall have an effective diameter of less than 100 μm. The mean plutonium rich particle distribution shall be less than 50 μm. No pure plutonium grain shall be greater than 400 μm.

It is of interest that this mission fuel specification invokes the important difference between plutonium-rich particles and pure plutonium grains. The plutonium content of the plutonium-rich particles in MIMAS-produced fuel is limited to that of the master-mix (sometimes denoted "primary blend").

4.6.3 Technical Specifications for the MOX Test Irradiation

Provisions with respect to agglomerate size are included in the Technical Specification for the MOX test pellets (Reference 23). Section 4.10 "Microstructure," Subsection 4.10.2 "Homogeneity" provides that

> No more than 5% of the nominal PuO_2 content shall be present in PuO_2-rich (having a plutonium content greater than 150% of the nominal bulk composition) particles of diameter greater than 200 μm. … Area percent and volume percent should be considered equivalent …

The "nominal PuO_2 content" for this test fuel is 5%, which, as explained in Section 4.3, is mixed with UO_2 to the extent that the resulting master-mix constitutes 16.11% of the total fuel mass. Within the final fuel, the master-mix is manifested as agglomerates, ranging in size from very small to quite large.

In applying the specification, it is assumed that the milling is sufficient to ensure that the PuO_2 is evenly distributed among the agglomerates. Given that the volume fraction is approximately equal to the mass fraction, and with the guidance that "area percent and volume percent should be considered equivalent," this specification provides that PuO_2-rich agglomerates with equivalent diameters larger than 200 μm should occupy no more than 0.0081 (5% of 16.11%) of the unirradiated fuel cross-sectional area. A review of the data measurements taken at Los Alamos following fuel fabrication indicates that plutonium-rich agglomerates greater than 200 μm occupied slightly more than 5% of the unirradiated fuel cross section. Although this exceeds the Specification, it is not of concern since fuel-reprocessing considerations are not of interest to this MOX test irradiation.

4.7 Agglomerate Growth and Restructuring During Irradiation

Most fissions occur within the plutonium-rich agglomerates, and although recoil and knockout processes cause a small portion of the fission products to migrate to the surrounding UO_2 matrix, most are retained within the agglomerates. Hence, these bodies swell as burnup increases due to the accumulation of both solid and gaseous fission products. An excellent discussion of the experimentally observed agglomerate states at various locations across pellet cross-sections and at various stages of burnup is found in Reference 12.

When evaluating the extent of irradiation for a mixed-oxide fuel prepared with a MIMAS-type fabrication process, it is important to recognize that two additional burnups, besides the fuel-average burnup, are appropriately defined. These are the burnup within the plutonium-rich agglomerates and the much smaller burnup within the surrounding matrix of depleted uranium. For the MOX test fuel in the earliest stages of irradiation, it is reasonable to make the approximation that all of the fissions occur within the agglomerates and none within the surrounding depleted UO_2 matrix. As explained in Section 4.3, 16.11% (about one-sixth) of the total fuel resides within the agglomerates. Since burnup (GWd/MTHM) is the ratio of energy release to fuel mass, the burnup rate within the agglomerates is initially about six times the fuel average. At 2 GWd/MT for the mixed oxide, the burnup within the agglomerates is approximately 12 GWd/MT.

The ratio of agglomerate burnup to fuel-average burnup is reduced as irradiation proceeds due to the creation of fissionable isotopes (principally ^{239}Pu) within the depleted uranium matrix. Calculations performed at INL (Reference 24) based on the MOX test fuel provide estimates of the agglomerate and matrix burnups as functions of the local fuel average burnup. The agglomerates reach 60 GWd/MT when the average burnup is about 18.3 GWd/MT. At a predicted fuel average burnup of 50 GWd/MT, the associated burnups are 110 GWd/MT for the agglomerates and 38 GWd/MT for the UO_2 matrix. The extents of burnup differentials among the components of other test fuels are discussed in References 12 and 15.

High burnup within the plutonium-rich agglomerates is accompanied by considerable local swelling induced by the accumulated solid and gaseous fission products. Whereas the solid fission products stay with an agglomerate throughout fuel life, the fate of the fission product gases depends upon the temperature during irradiation of the region in which the agglomerate is located. In this context, it is important to recognize that the temperature of an agglomerate is only slightly higher that that of its immediate surrounding matrix, as explained in Reference 25.

Agglomerates become highly visible when they have transformed into a "high burnup structure." This structure forms within fuel above a local irradiation threshold of about 60 GWd/MT, when the temperature is below about 1000°C (Reference 26—thermal restructuring and thermal fission gas release processes dominate at higher temperatures). The high burnup structure is formed by a process of recrystallization that produces small (<1-micron) grains with many accompanying pores for storage of fission gas. For the MOX test irradiation withdrawals at 21 GWd/MT and higher, the two conditions for formation of the high-burnup structure (>60 GWd/MT at low temperature) exist within agglomerates in the cooler outer region of the fuel cross-section. It is their high-burnup structures that have made the agglomerates in this region readily visible.

The overall volumetric swelling rate for fuel (MOX or LEU) due to retention of fission product solids and individual gas atoms in the fuel lattice is about 0.7% per 10 GWd/MT. Applying this rate to a fuel-average burnup of 50 GWd/MT, the calculated swelling is approximately 3.5%. Local swelling within the agglomerates, where most of the fissions occur, is much higher. The agglomerate swelling is accommodated by plastic deformation of the surrounding UO_2 matrix so that the net effect is a global swelling of MOX fuel.

Gas storage within the pores of the agglomerate high-burnup structure adds to the effects of the fission product insertions into the fuel lattice, thereby inducing additional local swelling. Reference 12 reports bubble diameters as large as 4 μm for agglomerate burnups near 200 GWd/MT, with coalescence enabled as the increasing bubble diameters approached the initial separation distance between bubbles. Agglomerates in the outer portion of the test pellets (where the high-burnup structure evolved) were observed to swell by an additional 20 to 40% "due to the development of porosity within the agglomerates."

Reference 12 also reports observations with respect to agglomerates located at or very near the pellet surface, such that they were not completely surrounded by the restraining UO_2 matrix. With the "lack of compression to hinder swelling," these can grow out of the fuel surface. Such protruding agglomerates were observed (Reference 12) to have reached heights of 6 to 8 μm above the pellet surface at fuel-average burnups above 20 GWd/MT.

4.8 Agglomerate High-Burnup Structure Effects Upon Fission Gas Retention

Most of the krypton and xenon generated in the 50-GWd/MT withdrawals was created by fissions occurring within the agglomerates. Within the fuel pellet, local temperature drives the local gas release because temperature "determines the diffusion of the fission gas to the grain boundaries with subsequent formation of release channels" (Reference 12). In the cooler outer regions of the pellet, much of the fission gas is retained in pores (large intragranular bubbles) within the high burnup structures of the transformed agglomerates. In the pellet central region, where agglomerates have not recrystallized, the higher temperatures cause most of the fission gas to exit the agglomerates via diffusion. In both regions, a significant portion of the fission gas transfers to the matrix grains surrounding the agglomerate, taking the form of very small intragranular bubbles occupying the nanometer-sized cavities in the UO_2 matrix.

That there is room within the surrounding fuel matrix for such accumulations of fission gas atoms is discussed in Section 5.4 of Reference 27, which explains (based on measurements for irradiated UO_2)

> *that the matrix contains a large population, ~10^{24} m^{-3}, of small nanometer-size cavities. These quickly attain their final density and size, which appear to be largely independent of burnup. … These cavities grow by the capture of gas atoms and are destroyed by fission fragments which return the gases to solution; a steady-state morphology results.*

For MOX irradiation, the fission fragments chiefly originate within the agglomerates and hence tend to establish a directed radial migration of gas atoms farther into the surrounding grains of the UO_2 matrix.

4.9 PIE Observations: Agglomerate Structure, Size, and Surrounding Halos

Agglomerates that have transformed to the high-burnup structure can be easily discerned in irradiated fuel displayed in metallographic mounts. Such agglomerates have been evident in the PIEs for all fuel withdrawn with burnups of 21 GWd/MT or higher. Observations for these PIEs with respect to agglomerate distribution and size are discussed in Section 4.9.1. Fission gas distributions in the vicinity of agglomerates are discussed in Section 4.9.2. Finally, Section 4.9.3 explains the absence of high-burnup structure at the pellet rim.

4.9.1 Agglomerate Structure and Size

The fuel mounts examined for Capsule 2 (Fuel Pin 5) and Capsule 9 (Fuel Pin 12) are documented in Chapter 5 of Reference 28. Four metallographic mounts were prepared representing the fuel cross-sections for Pellets 1 and 14, near the top and bottom of both fuel pin pellet stacks. At this approximately 21-GWd/MT average fuel burnup, agglomerate high-burnup structures were clearly visible as light gray patches, irregularly dispersed in the outer half of the pellet cross-section.

Each mount included 6 to 9 visible agglomerates with equivalent diameters in excess of 200 μm, the largest being about 420 μm. One mount exhibited an agglomerate at the pellet surface, which had apparently bonded during irradiation with the inner surface of the cladding. A separate (fifth) mount was prepared for Scanning Electron Microscope (SEM) and Electron Probe Micro-Analyzer (EPMA) examinations. Scanning over one of the agglomerates visible at pellet midradius and its surrounding UO_2 matrix confirmed the expected high degree to which plutonium is concentrated in the agglomerates.

Reference 4 documents the PIE of the 30-GWd/MT Capsules 3 and 10 (Fuel Pins 6 and 13). As discussed in Chapter 5 “Metallography,” four metallographic mounts were prepared for fuel cross-sections taken from Pellets 1 and 15 in both fuel pins. The visible agglomerates were distinguished by the light gray patch shapes that outline their high-burnup structure, including the large internal pores in which their fission gases are concentrated. Similar to the earlier PIE, these (visible) agglomerates were irregularly dispersed over the portion of the pellet cross-section about one-quarter-radius inward from the pellet rim.

The largest of the agglomerates at 30 GWd/MT had an equivalent diameter of about 600 μm, some 50% larger than the maximum seen at 21 GWd/MT. Several instances of sporadic bonding were evident between agglomerates at the pellet surface and the adjacent cladding.

There was virtually no evidence of high-burnup structure in the central (highest-temperature) regions of the fuel cross-section. Stated another way, the plutonium-rich agglomerates in the fuel inner regions were not visible due to the absence of transformed grains and local gas-filled pores.

The PIE of the 40-GWd/MT Capsules 4 and 13 (Fuel Pins 7 and 16) is documented in Reference 29, including discussion of the visible plutonium-rich agglomerates in Chapter 5 “Metallography.” For Fuel Pin 7, four metallographic mounts represented fuel cross-sections at Pellet 2 (upper end), Pellet 10 (upper end and middle), and Pellet 15 (upper end). Three mounts were taken from Fuel Pin 16—at Pellet 1 (lower end), Pellet 2 (upper end), and Pellet 15 (upper end).

The mounts containing fuel and surrounding cladding from the vicinity of the upper end of Pellet 2 in both fuel pins were examined by SEM and EPMA. It was necessary to limit the amount of fuel held in

these mounts to reduce the dose rate— the Fuel Pin 16 mount was the thicker of the two because the TIGR-treated fuel was more friable. Both mount surfaces were of excellent quality (very little pullout). Agglomerates in the outer regions of the fuel mount surfaces were clearly visible by virtue of their recrystallization to a high-burnup structure.

The 50-GWd/MT PIEs are discussed in the Volume 1 companions to this report. As usual, fuel mount metallography is the subject of Chapter 5 in both documents. Of the three MOX test capsules withdrawn at 50-GWd/MT burnup, only Capsule 12 (Fuel Pin 15) contained TIGR-treated fuel. All of the nondestructive steps were completed for Fuel Pin 15, including cladding profilometry and determination of the fission gas release fraction. Destructive PIE proceeded through pin segmentation and preparation of fuel cross-section metallographic mounts for Pellet 1 (lower end) and Pellet 15 (upper end). Following visual and photo-examination of these two mounts to confirm normal fuel performance, the PIE for Fuel Pin 15 was truncated.

Capsule 5 (Fuel Pin 8) and Capsule 6 (Fuel Pin 9) were both represented by fuel cross sections mounted for Pellet 1 (bottom end), Pellet 10 (both ends), and Pellet 15 (upper end) as well as a fuel axial section (2 1/2 pellets) mounted from the middle of Pellet 11 through the middle of Pellet 13. The fuel appears in excellent condition, with dish and chamfer regions clearly discernable and undistorted. As in the previous (40-GWd/MT) PIE, thin oxide regions are visible intermittently along the cladding inner surfaces, particularly in the vicinity of agglomerates at or near the fuel surface. Other than these normal corrosion patterns, the cladding inner walls are in pristine condition.

Fuel Pin 8 reached approximately the same burnup as did Pin 9, but was irradiated at lower temperatures, and correspondingly, more agglomerates are visible in the central regions of the fuel cross-sections.

Areas of particular interest in all mounts were the halos (fission gas storage regions discussed in Section 4.9.2) surrounding the large agglomerates, the absence of high-burnup structure within the depleted UO_2 matrix at the pellet rim (discussed in Section 4.9.3), and the nature of the corrosion layers intermittently located along the pellet-cladding interface (discussed in Chapter 5).

4.9.2 Halos

As fission gas accumulates within the UO_2 grains abutting the agglomerates, an optical effect in the form of halos becomes visible in the fuel cross section photographs. Each halo is comprised of a high density of very small gas bubbles within the UO_2 matrix grains. Agglomerates of widely varying sizes all display the halo, a clear region distinct from both the UO_2 matrix and the high burnup structure. First prominent in the 40-GWd/MT PIE, these regions are visible because the athermal (concentration gradient and fission recoil) diffusion of fission gas from the agglomerate has altered the adjacent matrix to a form that responds differently to polishing. The presence of xenon within the halos was confirmed by EPMA measurements in both the 40- and 50-GWd/MT PIEs.

Halo thickness is on the order of a few fission fragment recoil distances (10–50 μm). Because the amount of gas generated is proportional to agglomerate volume, it follows that the halos are of nearly uniform thickness with volumes proportional to the agglomerate surface area.

The halos are in essence gas storage sites that collect the athermal diffusion from the agglomerates. The gas within the halo regions is eligible for eventual release to the pin free volume by absorption/ejection from cavity to cavity until the process of random diffusion carries the individual gas atoms to a grain boundary and into a relatively large intergranular bubble.

4.9.3 Absence of High-Burnup Structure at the Pellet Rim

The flux spectrum experienced by the MOX test fuel in the ATR reflector was softer than that encountered by fuel in a commercial PWR. The softer spectrum served to increase the effective fission cross section by a factor of about 4, meaning that fuel irradiated in the ATR reflector could sustain the same linear power with about one-fourth the thermal flux that would be necessary in a commercial PWR (Reference 24). The ^{238}U capture cross section is, however, only slightly increased in the softer spectrum.

With one-fourth the thermal flux, the buildup of ^{239}Pu at the pellet rim is much slower in the ATR reflector than for fuel at the same axial power level in a commercial PWR. With less local buildup of fissile material, the rim burnup will be closer to the UO_2 matrix average. This explains the absence of high-burnup structure around the pellet rims in the MOX test fuel.

4.10 Discussion and Conclusions

Mixed-oxide fuels currently fabricated for commercial purposes in European reactors by master-mix processes such as MIMAS or OCOM typically contain about 5 weight percent plutonium and include master-mix clumps (plutonium-rich agglomerates with an average size of <50 micron and 95% of the particle size is <100 micron) regularly dispersed in the UO_2 matrix. Some larger particles, up to 200 μm can be found irregularly dispersed in the UO_2 matrix (Reference 15). The master-mix, prepared by milling a 30% PuO_2–70% UO_2 powder combination, is diluted into a much larger (fivefold by mass) UO_2 matrix. The final blend is more homogeneous than the dual structure of a simple (pure PuO_2 particles embedded in a UO_2 matrix) mixture because the plutonium content of the agglomerates is no more than 30%. When irradiated, this MOX fuel develops both high-burnup (agglomerates) and low-burnup (UO_2 matrix) regions.

The fuel microstructure is influenced by the UO_2 powder characteristics, which determine both the porosity distribution and the master-mix distribution in the matrix (Reference 14). Pore size and distribution are affected in MIMAS by a proprietary pore-forming additive. The MOX test fuel was fabricated with a MIMAS-type approach, in that a master-mix was milled and then diluted into a secondary blend. However, the depleted UO_2 was not of the free-flowing kind, the pore-forming additive was not employed, the mill and mixer were not the same, and the master blend was not sieved. Because of these differences, the MOX fuel prepared at LANL for this project should not be considered as MIMAS mixed oxide, but rather as a test fuel fabricated with gallium-containing weapons-derived plutonium utilizing a MIMAS-type approach.*

The MOX test fuel comprises 5% PuO_2 derived from a weapons component and 95% depleted UO_2 (CAMECO powder) converted via the ammonium diuranate (ADU) process. The secondary blending was not as effective as desired in dispersing the (unsieved) master-mix into the UO_2 matrix so that relatively large master-mix clumps (agglomerates) are evident in the final fuel. The Pellet Processing Data packages prepared at Los Alamos subsequent to the test fuel fabrication indicate an average measured area fraction of about 1.5% for plutonium-rich agglomerate equivalent diameters greater than 400 microns. During irradiation, these agglomerates swell due to the accumulation of both solid and gaseous fission products. At burnups of 40 and 50 GWd/MT, the largest of the visible agglomerates have equivalent diameters in the 500- to 600-micron range.

*This MOX test irradiation was initiated before the mission fuel was selected. It was never intended that this test fuel should be prototypic of the mission fuel, since this is the role that the lead test assemblies will play. The purpose of this test irradiation is to demonstrate the use of MOX fuel prepared with weapons-derived plutonium.

Literature values for postirradiation agglomerate maximum equivalent diameters in modern European commercial fuels range from 250 to 400 microns for fuel average burnups in the vicinity of 45 GWd/MT. Thus, the current PIE results (and the measured preirradiation sizes) confirm that this test fuel began irradiation with a greater proportion of large agglomerates than is normally encountered in modern mixed-oxides. Nevertheless, the subsequent swelling during irradiation has been as expected for the current burnup, and there have been no performance problems with this fuel. As discussed in Chapter 3, fission gas release has been no greater than that expected from the European experience.

Fission gas storage in the vicinity of high-burnup structure is discussed in Reference 27. Fission gas initially collects in three locations: in solution in the fuel matrix, in very small (nanometer) intragranular bubbles, and in relatively large intergranular bubbles at the grain boundaries. As irradiation proceeds, a fourth gas collection category comprises the large intergranular pores within regions in which the fuel has transformed into its high burnup structure. Whereas the large bubbles are visible by microscope, very small bubbles must be detected by EPMA, to which the larger gas collections are invisible. Stated another way, EPMA shows the fission gas in solution or in the very small intragranular bubbles, but the larger intergranular and high-burnup structure bubbles must be viewed by SEM. (See Reference 30.)

In general, a high-burnup structure (small grains with a few large pores) evolves during irradiation when the local temperature is less than 1000°C and the local burnup exceeds about 60 GWd/MT. Prior to transformation, much of the fission gas is stored in nanometer-size cavities within the approximately 10-micron fuel grains. Subsequent to transformation, the grains are in the 0.5- to 1.0-micron range, in a structure interspersed with relatively large gas storage pores. The steps in the development of this structure are discussed in Reference 26. Much of the gas displaced from the very small intragranular cavities is collected (at high pressure) in the facetted pores of the recrystallized microstructure.

Agglomerates in the outer regions of the MOX test fuel metallographic mount surfaces are clearly visible due to their high-burnup structure. The halos around these agglomerates are fission gas that has entered the surrounding UO_2 grains, either by diffusion prior to transformation or by displacement when the high-burnup structure was formed. Faint agglomerate outlines discerned in the central regions of these fuel mount surfaces at 40 GWd/MT are supplanted by bolder outlines at 50 GWd/MT—these flag the ongoing transformations to high-burnup structure. Transformation of the agglomerates in the central region was delayed due to local temperatures greater than 1000°C earlier in the irradiation.

No indications of recrystallization have been found in the UO_2 matrix around the pellet circumference. Although the rim area experienced temperatures well below 1000°C during the irradiation, local burnups obviously have not reached 60 GWd/MT. This is attributed to the relatively soft flux spectrum seen by the test assembly in the ATR reflector, which serves to increase the effective fission cross section about fourfold (Reference 24). This means that fuel irradiated in the ATR reflector can sustain the same linear power with about one-fourth the thermal flux that would be necessary in a commercial PWR. The U^{238} cross section is, however, only slightly enhanced in the softer spectrum. With one-fourth the thermal flux, the buildup of ^{239}Pu at the pellet rim is much slower in the ATR reflector, and with less local buildup of fissile material, the rim burnup lies closer to the UO_2 matrix average. This explains the absence of high-burnup structure at the pellet rim in the MOX test fuel at 50 GWd/MT.

5. CLADDING INNER SURFACE OXIDATION

5.1 Introduction

This chapter addresses the MOX test fuel cladding inner surface oxidation as observed for Fuel Pins 8, 9, and 15 (Capsules 5, 6, and 12). These three fuel pins had been irradiated to approximately 50 GWd/MT at the time of withdrawal for PIE.

The fissioning of heavy metal oxides releases oxygen atoms within the fuel matrix. Most of this freed oxygen is taken up by fission products or in increasing the oxygen potential of the remaining heavy metal oxides, but a small fraction promotes cladding inner surface corrosion. There is no oxidation of the cladding outer surfaces in this test since these surfaces remained in a helium atmosphere throughout the irradiation.

The observed oxidation patterns are reviewed in Section 5.2. Section 5.3 describes the means by which oxygen released in fuel reaches the cladding inner surface. The European experience with cladding inner surface oxidation is discussed in Section 5.3. Finally, Section 5.4 provides a synopsis of the main points and conclusions of this chapter.

5.2 Oxidation Patterns

The PIE observations for the 50-GWd/MT burnup fuels are documented in the Volume 1 companions to this report. In both cases, Chapter 5, "Metallography," includes descriptions of the oxide layers as observed at the cladding inner surfaces. Pellet-cladding interface regions are illustrated both as circles surrounding fuel cross-section mounts and as straight runs down both sides of axial (half pellet- pellet-half pellet) mounts. In all cases, the oxide layers are intermittent and never penetrate more than a few microns into the cladding surface.

The nature of the corrosion layers intermittently located along the pellet-cladding interfaces is of interest to the evaluation of cladding performance. The fuel cross section mounts generally show short arcs of relatively thick oxidation, while the majority of the pellet-cladding circumference carries either light or spotty oxidation or is clean. Where oxidation is present, it is much thicker over locations where agglomerates are embedded at or very near the fuel surface. Typically, a 10- to 20-micron oxide thickness directly over an agglomerate decreases to no more than 5–10 microns over the immediately adjacent UO_2 matrix.

In general, oxidation along the edges of the axial mounts is more prevalent on one side of the cladding than on the other. Moreover, on the less-oxidized side of the axial section, even the areas over the surface agglomerates show little oxidation.

In some of the thicker oxidation regions, it is evident that a portion of the fuel that bonded to the cladding during irradiation remained adhered to the cladding when the pellet contracted (more than the cladding) upon cooldown. Where this has occurred, cracks are observed within the fuel roughly parallel to the cladding surface.

5.3 Oxygen Sources

Almost no oxygen was present in the MOX test fuel pin atmospheres at the time the fuel pins were sealed. Procedures at Los Alamos specified a glove box atmosphere of 99.995% helium purity with less than 10 ppm oxygen and less than 1.0 ppm moisture. Measured oxygen levels were between 0.40 and

1.65 ppm while the pellet stacks were loaded and between 0.4 and 0.8 ppm when the pin upper end caps were welded. Moisture was always recorded as less than 0.1 ppm.

A great deal of oxygen is, of course, stored in the UO_2 and PuO_2 molecules of the fuel. Each fission thereby frees two atoms of oxygen. To give a feel for the numbers, the Fuel Pin 9 burnup of 50.0 GWd/MT implies 9.44E21 fissions releasing 15.67E-3 gram-moles O_2, sufficient to produce a substantial partial pressure in the approximately 1-cm^3 fuel pin atmosphere if the oxygen remained free. This pressurization does not occur because the thermodynamics of the $(U,Pu)O_2$ system preclude the existence of free oxygen in contact with these compounds. Virtually all of the released oxygen that is not bound to solid fission products (primarily rare earths, zirconium, molybdenum) is consumed by boosting the oxygen potential of the UO_2 slightly.

Chapter 5, "Oxide Chemistry," of Reference 13 explains that whereas UO_2 readily becomes hyperstoichiometric in the presence of excess oxygen, PuO_2 cannot. [The oxygen-to-metal (O/M) ratio for PuO_2 cannot exceed 2.0.] Furthermore, PuO_2 fission is more oxidizing, in the sense that a lower proportion of the fission product mix can take up oxygen. In other words, more oxygen is released into the fuel lattice because more of the fission products are noble metals, which do not oxidize.

As UO_2 becomes slightly hyperstoichiometric, its oxygen potential increases dramatically. Reference 31 explains for MOX fuels that the oxygen potential "exhibits its maximum variation with O/M when the O/M = 2. Here, the anion vacancies are all just filled and any additional oxygen incorporated into the lattice must then enter interstitial positions, thereby accounting for the large increase in (oxygen potential) at this point."

5.4 European Experience—Inner Surface Corrosion

Cladding inner surface oxidation has been observed in PIEs of the MOX fuel irradiated for commercial purposes in European reactors. An excellent discussion is found in Section 5.5 of Reference 25, where comparison is made of two oxide layers at a fuel-average burnup of 44.5 GWd/MT, one over a surface agglomerate and the other over a length of UO_2 matrix. The oxide layer over the agglomerate is more than twice as thick and contains slightly higher solid fission product concentrations. Both oxygen layers appear similar to their counterparts as observed for the MOX test fuel in the current PIE.

Surface agglomerates actually protrude above the pellet surface during irradiation, pressing hard against the overlying cladding in some cases. Figure 6 of Reference 25 features the marks left on the cladding inner surface by raised MOX agglomerates during irradiation to 44.5 GWd/MT.

There is nothing in the PIE observations for the MOX test fuel that would tend to contradict the cladding internal oxidation process scenario proposed by L. Desgranes in Reference 32. Basically, the oxygen is passed from fuel to cladding by solid-state athermal diffusion promoted by the energy release of fission products. (Transport by thermal diffusion is specifically discounted.) The athermal diffusion requires that the fissioning fuel be in either close range (within about 10 microns) or direct contact with the cladding inner surface. Energy release by the fission products slowing down in the fuel creates secondary recoil atoms, including oxygen, which then reach (and are implanted in) the cladding.

The prerequisite that the fuel be in close proximity to the cladding also explains the European experience that cladding internal corrosion thicknesses of about 5 microns appear quite suddenly, when fuel burnups have reached about 25 GWd/MT. Until the cladding becomes "in-range," the oxygen freed by fission is consumed by occupying interstitial positions in the UO_2 lattice and thereby rendering the fuel hyperstoichiometric. The interstitial oxygen is more lightly bound, and when the pellet-cladding gap is sufficiently narrowed, this excess oxygen is unloaded into the cladding, causing a very rapid initial

formation of the corrosion layer. Subsequently, the layer thickness increases slowly as additional oxygen is freed.

Fission products that penetrate the cladding inner surface by direct recoil also play a role in preparing the surface for oxidation. This concept is buttressed by the interesting experiment described in Reference 33. The in-reactor corrosion rates of Zircaloy-4 were found to be significantly accelerated by trace levels of fissile impurities "due to irradiation-enhanced diffusion of the oxidizing species as a result of fissioning within the oxide along with easier diffusion paths created by the fission tracks." "Fissioning of the fissile impurities yields energetic fission fragments that tear through the growing oxide and affect the corrosion process by (1) accelerating the pre-transition and post-transition corrosion rates and (2) delaying the transition…"

5.5 Discussion and Conclusions

There was no indication of cladding inner surface corrosion in the early (9-GWd/MT) PIE. An isolated instance of surface agglomerate—clad bonding was observed (Figure 5.9 of Reference 28) in the intermediate (21-GWd/MT) PIE. Additional instances of bonding over surface agglomerates were noted at 30 GWd/MT (Figures 5.7 and 5.8 in Reference 4). Widespread bonding over agglomerates and sporadic areas of general corrosion in the absence of agglomerates were first seen in the 40-GWd/MT PIE (Reference 29) and again in the current (50-GWd/MT) fuel mount examinations.

Based on the European literature, cladding inner surface corrosion requires that excess oxygen be available and that the fuel be in contact with the cladding to provide a path for solid-state thermal (fission-fragment-induced) diffusion of the oxygen atoms. Excess (interstitially located) oxygen becomes increasingly available as the oxygen freed by fission brings the UO_2 to a hyperstoichiometric state. Thus, the amount of loosely bound oxygen available for athermal diffusion to the cladding inner surface increases with burnup.

The extent to which pellet surface is in contact with the cladding is not easily characterized. Pellet hourglassing due to a greater axial thermal expansion along the pellet centerline distorts the initial fuel shape. For the MOX test fuel, this brought the pellet ends into contact with the cladding on initial heatup. Subsequent cracking (both radial and axial) brought fuel fragments located more toward the pellet midplane into one-sided or point contact with the cladding. In general, wherever a portion of fuel surface approached the cladding, contact was first made over any surface agglomerates, since these protrude above the surrounding pellet surface during irradiation.

Thus, the uneven and noncontiguous nature of the observed corrosion is simply a matter of the haphazard manner in which the pellet fragments came into contact with the surrounding cladding during irradiation. The thicker corrosion over the agglomerates follows directly from the locally narrow fuel-cladding gaps when these agglomerates are swollen during irradiation. It is concluded that the cladding corrosion patterns observed in the MOX test fuel are in accordance with expectations based on the documented European experience.

6. MOX FUEL DENSIFICATION AND SWELLING

6.1 Introduction

Three metallographic mounts were prepared from Capsule 1 (Fuel Pin 2) after Phase I of the MOX test; see Reference 34 (8-GWd/MT PIE final report). Following completion of Phase II, two mounts were prepared from Capsule 2 (Fuel Pin 5) and two from Capsule 9 (Fuel Pin 12); descriptions of the sample preparation, polishing and etching techniques are presented in Chapter 5 of Reference 28 (21-GWd/MT PIE final report). Following completion of Phase III, two mounts were prepared from Capsule 3 (Fuel Pin 6) and two from Capsule 10 (Fuel Pin 13); see Chapter 5 of Reference 4 (30-GWd/MT PIE final report). After completion of Phase IV, Part 1, five mounts were prepared from Capsule 4 (Fuel Pin 7) and three from Capsule 13 (Fuel Pin 16); see Chapter 5 of Reference 29 (40-GWd/MT PIE final report). After completion of Phase IV, Parts 2 and 3, five mounts were prepared from Capsule 6 (Fuel Pin 9) and two from Capsule 12 (Fuel Pin 15); see Chapter 5 of Reference 35 (50-GWd/MT PIE final report for Capsules 6 and 12); also, five mounts were prepared from Capsule 5 (Fuel Pin 8); see Chapter 5 of Reference 36 (50-GWd/MT PIE final report for Capsule 5).

Altogether, thirty-one metallographic mounts of diametral cross-sections have been prepared from fuel pins withdrawn after Phases I; II; III; IV, Part 1; and IV, Parts 2 and 3 of the weapons-derived MOX test irradiation. The mount identification numbers, fuel type, and axial locations are given in Table 6.1. (Pellet 1 is located adjacent to the fuel pin gas plenum; fuel type B was TIGR-treated.)

In addition to the diametral metallographic mount cross-sections, four axial metallographic mounts have been prepared. MET Mount 6167 was prepared from Phase III, Fuel Pin 13 comprising Pellets 7 through 9; MET Mount 6221 was prepared from Phase IV, Part 1, Fuel Pin 7 comprising Pellets 11 through 13; MET Mount 6257 was prepared from Phase IV, Parts 2 and 3, Fuel Pin 9 comprising Pellets 11 through 13; and MET Mount 6266 was prepared from Phase IV, Parts 2 and 3, Fuel Pin 8 comprising Pellets 11 through 13. All axial mounts indicate stable fuel behavior with distinct pellet dishing and chamfer clearly visible; also, no significant pellet/cladding interaction effects are seen except at the pellet-to-pellet interfaces.

The PIE metrology of the Phase I, capsules (1 and 8), and fuel pins (2 and 11) is contained in Chapter 4 of Reference 34. The Phase II, capsules (2 and 9), and fuel pins (5 and 12) PIE metrology is given in Chapter 4 of Reference 28. The Phase III, capsules (3 and 10), and fuel pins (6 and 13) PIE metrology is given in Chapter 4 of Reference 4. The Phase IV, Part 1, capsules (4 and 13), and fuel pins (7 and 16) PIE metrology is given in Chapter 4 of Reference 29. The Phase IV, Parts 2 and 3, capsules (6 and 12), and fuel pins (9 and 15) PIE metrology is given in Chapter 4 of Reference 35. The Phase IV, Parts 2 and 3, Capsule 5, and Fuel Pin 8 PIE metrology is given in Chapter 4 of Reference 36.

Subsequent to issue of the Phase II final PIE report and before the Phase III PIE, an innovative Fuel Pin Measuring Apparatus (FPMA) was developed (Reference 37) for precise measurement of the outer cladding surface profile. Additionally, an improved dial indicator and V-block type apparatus was employed for the Phase III quick-look PIE report (Reference 38). Both the V-block and the FPMA were calibration-verified before and after measuring the Phase III fuel pins. The V-block reproduced the calibration standard within 0.0002 in. and the FPMA within 0.0001 in. Also, for the Phase III fuel pin measurements, there was excellent correspondence between the two methods of measurement (agreement within the apparatus uncertainties at all measurement locations).

Table 6.1. Fuel pin metallographic mount identification

Irradiation phase	Met. mount ident. number	Capsule	Fuel Pin	Fuel type	Axial location (pellet number)	Comments
I	6139	1	2	A	5	
I	6140	1	2	A	5/6 interface	
I	6141	1	2	A	6	
II	6143	9	12	B	1	
II	6144	9	12	B	14	
II	6145	2	5	A	1	
II	6146	2	5	A	14	
III	6161	3	6	A	1	
III	6162	3	6	A	15	
III	6163	10	13	B	1	
III	6164	10	13	B	15	
IV, Part 1	6217	4	7	A	Bottom of 1	Excessive pull-outs, not used
IV, Part 1	6218	4	7	A	Top of 2	
IV, Part 1	6219	4	7	A	Top of 10	
IV, Part 1	6220	4	7	A	Middle of 10	
IV, Part 1	6222	4	7	A	Top of 15	
IV, Part 1	6223	13	16	B	Bottom of 1	
IV, Part 1	6225	13	16	B	Top of 15	
IV, Part 1	6240	13	16	B	2	
IV, Parts 2 & 3	6254	6	9	A	Bottom of 1	
IV, Parts 2 & 3	6255	6	9	A	Top of 10	
IV, Parts 2 & 3	6256	6	9	A	Middle of 10	
IV, Parts 2 & 3	6258	6	9	A	Top of 15	
IV, Parts 2 & 3	6276	6	9	A	Top of 2	Excessive pull-outs, not used
IV, Parts 2 & 3	6260	12	15	B	Bottom of 1	
IV, Parts 2 & 3	6261	12	15	B	Top of 15	
IV, Parts 2 & 3	6263	5	8	A	Bottom of 1	
IV, Parts 2 & 3	6264	5	8	A	Top of 10	
IV, Parts 2 & 3	6265	5	8	A	Middle of 10	
IV, Parts 2 & 3	6267	5	8	A	Top of 15	
IV, Parts 2 & 3	6268	5	8	A	Top of 2	

The FPMA profilometry measurements of the Phase III; Phase IV, Part 1; and Phase IV, Parts 2 and 3 fuel pins (approximately 300 axial points per pin over the 6-in. fuel length) indicate localized diametral peaks ("primary ridging") of the cladding overlying the pellet-to-pellet interfaces. This ridging is caused by hard pellet-to-clad interactions due to differential axial thermal expansion within the fuel pellet during power operation; engineering models and calculations illustrating this "hourglassing" phenomena are presented in Chapter 6 of the 30-GWd/MT PIE Implications report (Reference 39). After ridging was observed in the Phase III fuel pins, long segments of the archived Phases I and II fuel pins were defueled and then measured via the FPMA. These measurements also show ridges indicating that hard pellet-to-clad contact (sufficient to cause local yielding) occurred early in the irradiation, during the initial heatup in the ATR.

FPMA takes two sets of measurements on a fuel pin. Each measurement consists of four diametral measurements 90 degrees apart for each of several hundred axial positions. The second set of diametral measurements is taken after rotating the fuel pin 45 degrees from the first set (same axial locations). This

allows the determination of the fuel pin diameter and circumferential distortion of the clad. To date, no cladding ovality or distortion has been discerned, even with the Phases I and II fuel pin cutting and defueling operations. The fact that the fuel pins could be easily withdrawn from their very close fitting capsules provides mechanical verification that there are no gross fuel pin distortions.

The FPMA profilometry of the fuel pins provides reproducible diametral measurements, much more accurate than the dial indicator and V-block type metrology apparatus employed in the Phases I and II PIEs. Furthermore, the FPMA can automatically collect large amounts of data in a short time and is not as susceptible to the operational and mechanical difficulties of manual operations in a hot cell as is the V-block metrology device. Because of these advantages, FPMA profilometry of the fuel pins has been used exclusively since the 40-GWd/MT PIE and is now the method of choice. The ability to collect large amounts of accurate data has made the detailed analysis of the fuel pin ridging and creep possible.

This chapter performs a reassessment of the MOX fuel densification and swelling given the additional data from the 50-GWd/MT PIEs. (The previous assessment is found in Chapter 5 of Reference 40.)

The capsule and fuel pin metrological results and measurements made directly from photographic enlargements of the metallographic mounts are employed in this chapter to determine

- the fuel pin Zircaloy cladding thickness and internal diameter,
- the free area within the fuel pin (that is, the peripheral gap between the fuel and the clad, and the internal cracks within the fuel pellet), and
- the fuel pellet equivalent outer diameter (representing all internal cracks as closed, with their areas added as part of the corresponding pellet-clad gap).

These quantities are determined for each of the Phase IV, Parts 2 and 3 metallographic mounts using the imaging software Image-Pro Plus, Version 5.1 (Reference 41).

These data are presented as functions of fuel burnup in Section 6.2. Conclusions are discussed in Section 6.3. These data are used as described in Section 6.4 to assess the fuel densification assumptions currently employed with the CARTS code fuel swelling models.

6.2 Capsule Component Dimensions

Note: This section describes in detail the measurement methods (metrology) used and the actual data analyses performed to determine the cladding and pellet dimensions from observations of the irradiated fuel metallographic (MET) mounts. Readers not interested in the pursuit of such detail are encouraged to skip ahead to Section 6.3, where the results are summarized.

6.2.1 As-Built Dimensions

A compilation of the as-built MOX capsule and fuel pin dimensions, taken from the ORNL component inspection reports and the LANL fuel QA reports, is provided in Table 6.2. Also included are the construction tolerances for these components. Per the construction drawings, the MOX pellet outer diameter, the capsule and cladding inner and outer diameters, and the capsule and cladding inner and outer diameter concentricities are specified. The cladding thickness and pellet-to-clad gaps are derived values based on the construction or as-built component ranges.

Table 6.2. MOX capsule and fuel pin dimensions

Item	Construction tolerance (in.)	As-built range[a] (in.)	As-built mean and uncertainty (in.)
Capsule OD	0.4640–0.4650	0.4643–0.4649	0.4646 ± 0.0003
Capsule ID	0.3830–0.3835	0.3830–0.3835	0.38325 ± 0.00025
Cladding OD	0.3805–0.3810	0.3805–0.3808	0.38065 ± 0.00015
Cladding ID	0.3290–0.3295	0.3290–0.3294	0.3292 ± 0.0002
Cladding concentricity	Radius 0.0010	Radius 0.00045[b]	
MOX pellet OD	0.3260–0.3270	0.3260–0.3265	0.32625 ± 0.00025
Cladding thickness (calculated)	0.0245–0.0270	0.02510–0.02635[c]	0.02573 ± 0.00063
Pellet to cladding radial gap (calculated)	0.0010–0.00175	0.00125–0.0017	0.00148 ± 0.00023
Cladding to capsule radial gap (calculated)	0.0010–0.0015	0.0011–0.0015	0.0013 ± 0.0002

[a]For the eleven withdrawn capsules (irradiated during Phases I; II; III; IV, Part 1; and IV, Parts 2 and 3).
[b]Maximum observed.
[c]As-built range for cladding thickness includes cladding concentricity.

6.2.2 Capsule Outer Diameter

The preirradiation value for the stainless steel capsule outer diameter for Capsules 1–6, 8–10, 12, and 13 is reported as 0.4643-to-0.4649 in. (Table 6.2). Here 0.4643 in. is the minimum measured outer diameter, while 0.4649 in. is the maximum measured outer diameter.

The postirradiation hot cell capsule measurements are given in Table 6.3. The estimated accuracy of the hot cell capsule diametral measurement is ±0.0005 in.; these measurements were performed with a dial indicator and V-block type apparatus.

Table 6.3. Measured capsule outer diameters

Irradiation phase	Capsule number	Meas. capsule surf. temp./ hot cell ambient temp. (°C)	Calc. capsule diameter range (in.)	Meas. (hot cell) capsule dia. (av. of 6 obs.) (in.)	Standard dev. about the mean (mils)
I	1	40.4/28.8	0.46445–0.46505	0.46462	0.16
I	8			0.46515	0.12
II	2	51.8/30.0	0.46453–0.46513	0.46532	0.17
II	9	53.2/30.2	0.46454–0.46514	0.46510	0.18
III	3	47.5/29.8	0.46450–0.46510	0.46557	0.12
III	10	47.8/30.0	0.46450–046510	0.46498	0.10
IV, Part 1	4	56.5/30.0	0.46456–0.46516	0.46550	0.23
IV, Part 1	13	56.8/29.8	0.46456–0.46516	0.46542	0.10
IV, Parts 2&3	6	44.6/27.6	0.46447-0.46507	0.46585	0.23
IV, Parts 2&3	12	42.9/26.6	0.46446-0.46506	0.46613	0.14
IV, Parts 2&3	5	42.7/27.0	0.46446-0.46506	0.46590	0.18

As shown in Table 6.3, using the preirradiation dimensions for the stainless steel capsule, the measured capsule temperature (at the midpoint, within the fueled region) in the hot-cell and the thermal linear expansion formulation for 304 stainless steel (from CARTS), the calculated hot-cell capsule outer diameter lies in the range from 0.46445-to-0.46516 in. This range essentially spans the observed measurements (with uncertainties); there is no observed change in the measured capsule outer diameter that can not be explained simply by thermal expansion and the capsule measurement uncertainties.

6.2.3 Fuel Pin Cladding Outer and Inner Diameters

The nominal as-constructed outer diameter of the fuel pin Zircaloy cladding is 0.3810 in. (with tolerances of +0.0000 and –0.0005 in.). The preirradiation value for the Zircaloy cladding outer diameter for Fuel Pins 2, 5–9, 11–13, 15, and 16 is reported as 0.3805-to-0.3808 in. (Table 6.2).

The PIE metrology results for the cladding outer diameter include positions outside the 6-in. fueled region, which extends from 1 to 7 in. as measured from the top of the fuel pin. Table 6.4 contains averages of the FPMA fuel pin diameter measurements taken within the fueled region during the PIEs conducted to date.*

Table 6.4. Measured fuel pin outer diameters

Irradiation phase	Burnup (radio. chem.) (GWd/MT)	Burnup (MCNP[a]) (GWd/MT)	Burnup (FRAPCON-3[b]) (GWd/MT)	Fuel Pin	Clad average outer diameter (in.)	Standard dev. about the mean (mils)
I	7.95[c] ± 0.40	8.63 ± 0.30	8.553 (+1.197/–0.253)	2	0.38073	0.07
I	NA[k]	8.54 ± 0.30	8.493 (+1.197/–0.253)	11	0.38090	0.15
II	22.2[c] ± 1.11 21.3[d] ± 1.07	20.90 ± 0.73	20.853 (+3.747/–1.073)	5	0.38084	0.14
II	21.5[d] ± 1.08	20.95 ± 0.73	20.935 (+3.755/–1.075)	12	0.38096	0.16
III	27.6[e] ± 1.38	29.66 ± 1.04	29.068 (+4.452/–1.898)	6	0.38104	0.11
III	27.8[e] ± 1.39 26.9[f] ± 1.35	29.61 ± 1.04	29.603 (+4.547/–1.933)	13	0.38118	0.11
IV, Part 1	41.8[g] ± 2.09 38.7[h] ± 1.94 38.0[i] ± 1.90 41.1[d] ± 2.06	38.98 ± 1.36	38.921 (+2.979/–0.511)	7	0.38148	0.11
IV, Part 1	41.9[g] ± 2.10 39.2[j] ±1.96 41.1[d] ± 2.06	38.98 ± 1.36	38.920 (+3.700/–0.930)	16	0.38176	0.12

*The FPMA was developed subsequent to the PIEs for Irradiation Phases I and II. Thus, full-length metrology for Fuel Pins 2, 5, 11, and 12 is not available. For these pins, FPMA measurements were taken (during the Phase III PIE) on the cladding segments that had been retained for later clad ductility testing.

Table 6.4. (continued)

Irradiation phase	Burnup (radio. chem.) (GWd/MT)	Burnup (MCNP[a]) (GWd/MT)	Burnup (FRAPCON-3[b]) (GWd/MT)	Fuel Pin	Clad average outer diameter (in.)	Standard dev. about the mean (mils)
IV, Parts 2&3	49.6[g] ± 2.48 48.1[h] ± 2.40 50.1[i] ± 2.50 53.0[d] ± 2.65	49.96 ± 1.75	49.975 (+4.125/–2.005)	9	0.38158	0.11
IV, Parts 2&3	NA[k]	50.21 ± 1.76	50.230 (+3.080/–0.620)	15	0.38178	0.12
IV, Parts 2&3	50.5[g] ± 2.52 49.8[h] ± 2.49 50.2[i] ± 2.51 49.8[d] ± 2.49	49.45 ± 1.73	49.372 (+2.668/–1.012)	8	0.38140	0.17

[a]LHGR-estimated burnup from MCNP calculations performed by G. Chang at INEEL.
[b]R-Z FRAPCON-3 model with 15 axial segments (one for each MOX pellet in fuel stack); based on MCNP calculated cycle-average LHGRs and axial peaking, and actual cycle EFPDs.
[c]Pellet number 2 (from fuel pin gas plenum).
[d]Pellet number 15.
[e]Pellet number 10.
[f]Pellet number 9.
[g]Pellet number 1.
[h]Pellets numbers 2 through 9.
[i]Pellet number 11.
[j]Pellets numbers 2 through 14.
[k]No radioactive chemical analyses performed.

Figure 6.1 shows how the average irradiated cladding outer diameters measured at hot cell temperature during the sequential PIEs increase with burnup. Applying the thermal linear expansion formulation for Zircaloy (from CARTS) with the measured cladding temperatures, the diameters of the fuel pins would range from 0.38054-to-0.38084 in. as measured in the hot cell. The average cladding outer diameters (including the computed uncertainty) plotted in Figure 6.1 for the 30-, 40-, and 50-GWd/MT withdrawal fuel pins are greater than this range of values, and hence cannot be accounted for by thermal expansion alone.

The FPMA profiles of all withdrawn fuel pins (all PIEs to-date) contain "peaks" (ridges corresponding to pellet-to-pellet interfaces) and "valleys" (corresponding to the low points over the pellet midplanes). The profilometry of Fuel Pin 7, illustrating the peaks and valleys, is shown in Figure 6.2.

The Fuel Pin 7 average outer diameter plotted in Figure 6.1 (for Phase IV, Part 1, average burnup of ~39 GWd/MT) is the average of the outer diameters (from 0.618-to-6.038 in. along the fuel pin length, excluding the distortions caused by the weldments of the upper and lower fuel pin plugs) including the peaks and valleys. As shown in Figure 6.2, there is a difference of approximately 0.27 mils between the average peak height and the average valley. Figure 6.1 can be expanded, as shown in Figure 6.3, to indicate the trends for the peaks and valleys for all withdrawn fuel pins.

The peaks or ridging are caused by hard pellet-clad interactions due to differential axial thermal expansion within the fuel pellet during irradiation. Ridging has been observed in all of the withdrawn fuel pins via the FPMA measurements. This indicates that hard pellet-clad contact occurred early in the irradiation, at the initial heatup for the first cycle in the ATR.

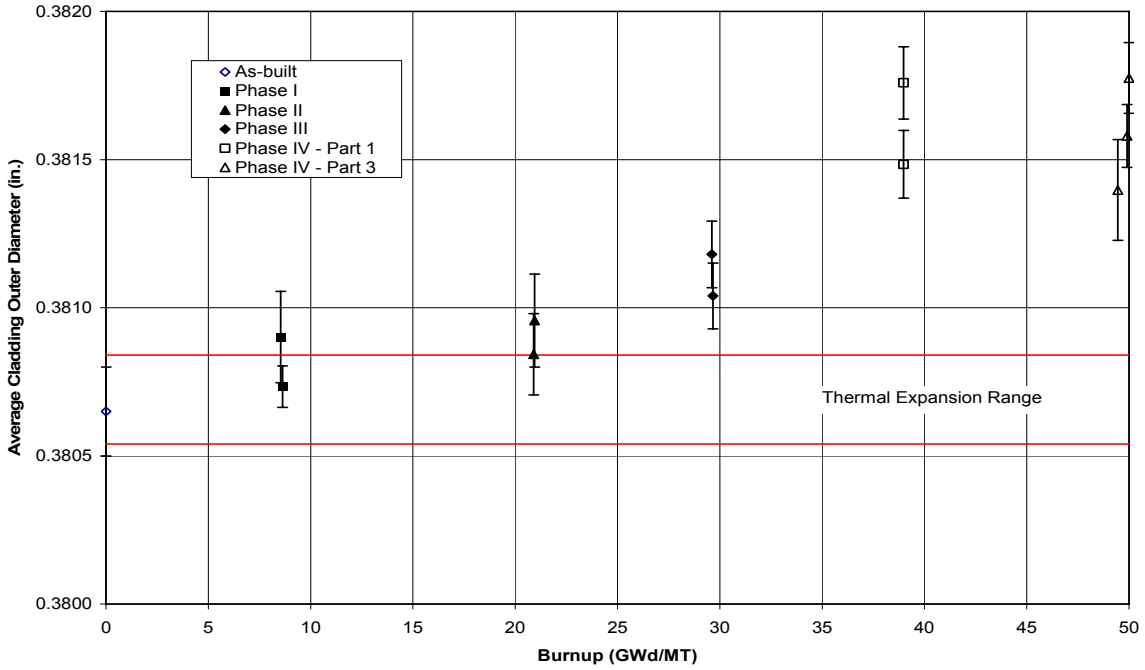

Fig. 6.1. Cladding outer diameter vs burnup—cold dimensions.

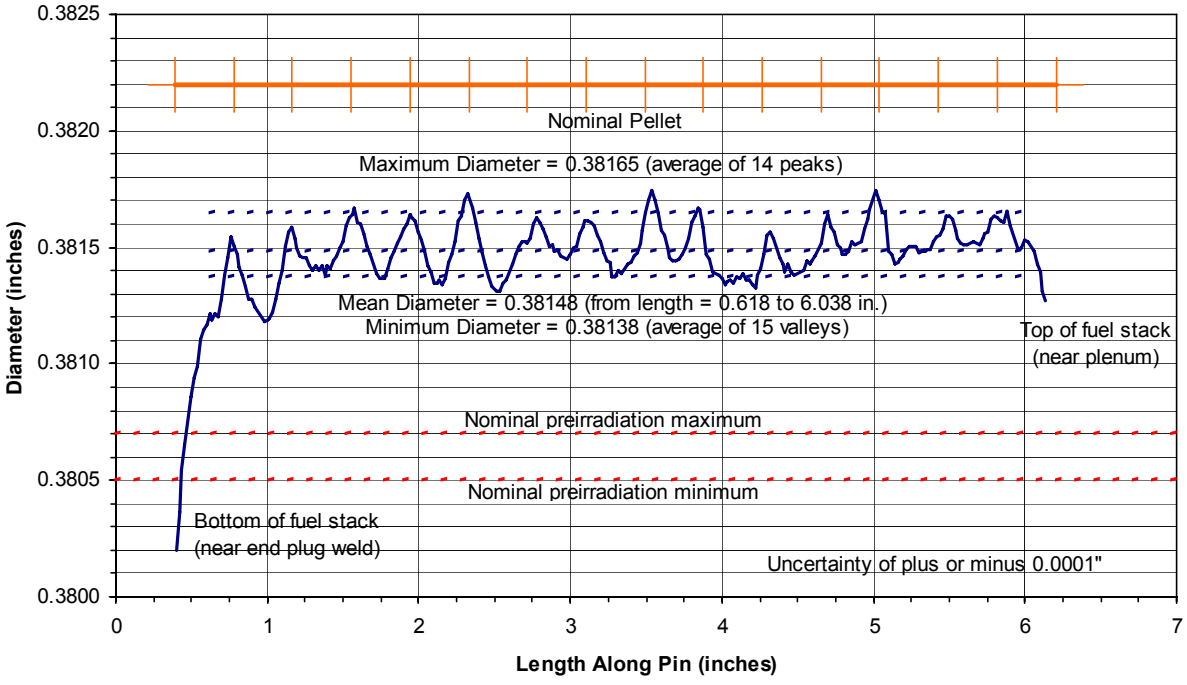

Fig. 6.2. Fuel Pin 7 (average burnup of ~39 GWd/MT) profilometry—cold dimensions.

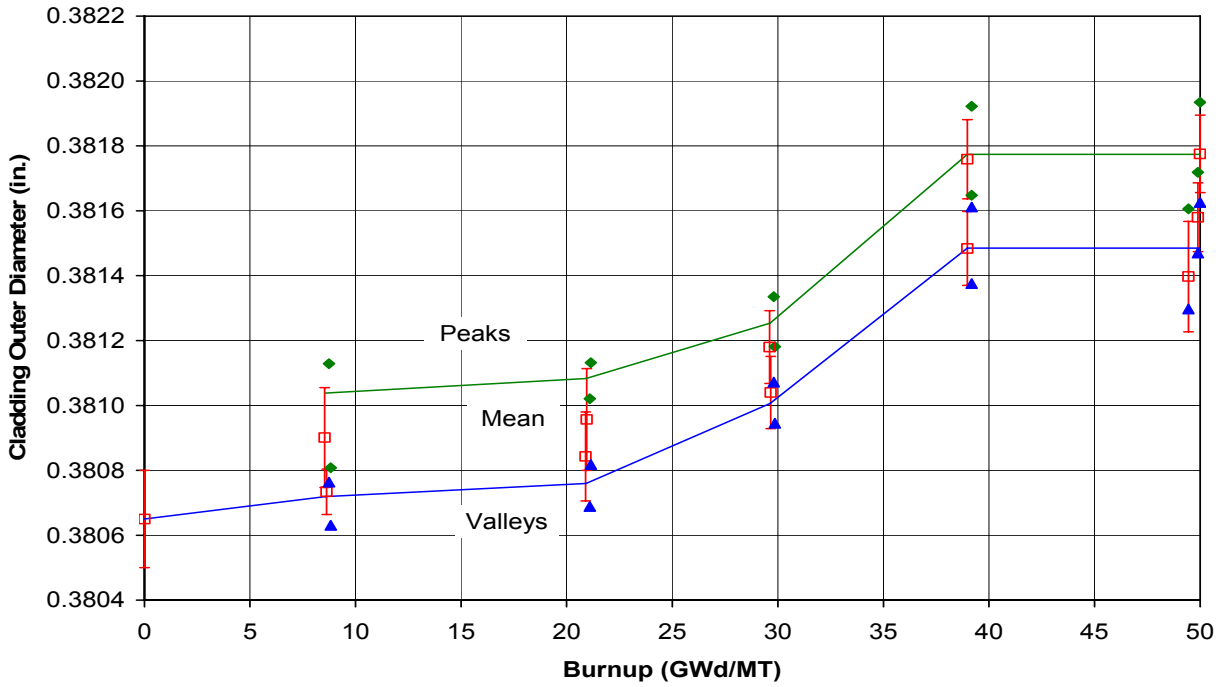

Fig. 6.3. Cladding outer diameter with "peaks" and "valleys" vs burnup—cold dimensions.

In the 30-GWd/MT PIE Implications report, it was stated that the observed outward cladding expansion was greater than would be expected for irradiation creep under the low (~1- to 2-MPa) wall tensile stresses calculated for the Phase III fuel pins. It was also conjectured that the major contributing factor must be mechanical dragging due to pellet hourglassing, which forces the cladding outward at points overlying the pellet-pellet interfaces. As shown in Figure 6.3, the relative difference between the "peaks" and "valleys" is approximately the same for all withdrawn MOX fuel pins. The apparent cladding creep outward is not a function of the formation of the cladding ridges; as shown in Figure 6.3, the valleys at burnups of 9 and 21 GWd/MT are within the as-built outer diameter tolerances.

With increased irradiation exposure and higher fuel pin internal pressures (due to additional fission gas release), the valleys of the 30-, 40-, and 50-GWd/MT fuel pins are greater than the as-built outer diameter tolerances. Furthermore, Figure 4.26 of Reference 29 clearly shows that small wall tensile stresses (~5 MPa) in the pressurized Fuel Pin 16 produced a measurable increase (0.2–0.3 mil) in the FPMA-determined fuel pin outer diameter (as compared with the unpressurized fuel pin).

Irradiation-induced growth in anisotropic materials such as Zircaloy requires no applied stress to produce a shape change at constant volume (Reference 13, pp. 176–177). Cold-working purposefully orients the hexagonal lattice such that the major <c> axis is normal to the axial direction of the cladding tube. Irradiation then produces a contraction in the <c> direction and expansion normal to this direction. The cladding tube lengthens slightly, while the wall thins to maintain constant volume.

In contrast, the outward cladding creep occurring during the MOX test irradiation is the product of an applied wall stress. It is believed that the valley diameters are representative of the extent of outward relocation. (The ridges, caused by pellet hourglassing, are independent of creep.) All the ingredients for creep are present: neutron irradiation, cladding wall tensile stress; and a cladding temperature during irradiation of 320°–400°C.

Chapter 6 of Reference 40 discusses the observed cladding creep for these fuel pins and develops an appropriate empirical correlation (a function of the integral of the product of the cladding wall stress and exposure) relevant for these test irradiations through a burnup of 40 GWd/MT. This correlation is compared with Halden creep data and literature creep correlations. However, in general, literature values are usually derived from PWR experience, where the creep is inward, not outward. Where outward clad creep experiments have been performed, the tensile wall stresses are almost always 60 MPa or greater. Chapter 7 of this report performs a reassessment of the cladding creep correlation given the additional data from the 50 GWd/MT PIEs.

There is slightly greater creep-out of the cladding for the TIGR-treated fuel; this behavior is illustrated in Figure 6.4. As shown in Table 3.1, the fission gas releases in the fuel pins with TIGR-treated fuel were always higher than those for their untreated counterparts. With a greater wall hoop stress, additional creep is to be expected. The post-PIE CARTS calculations (Chapters 8 and 9) employ empirical models for the cladding creep histories shown in Figure 6.4, as functions of fuel type and burnup.

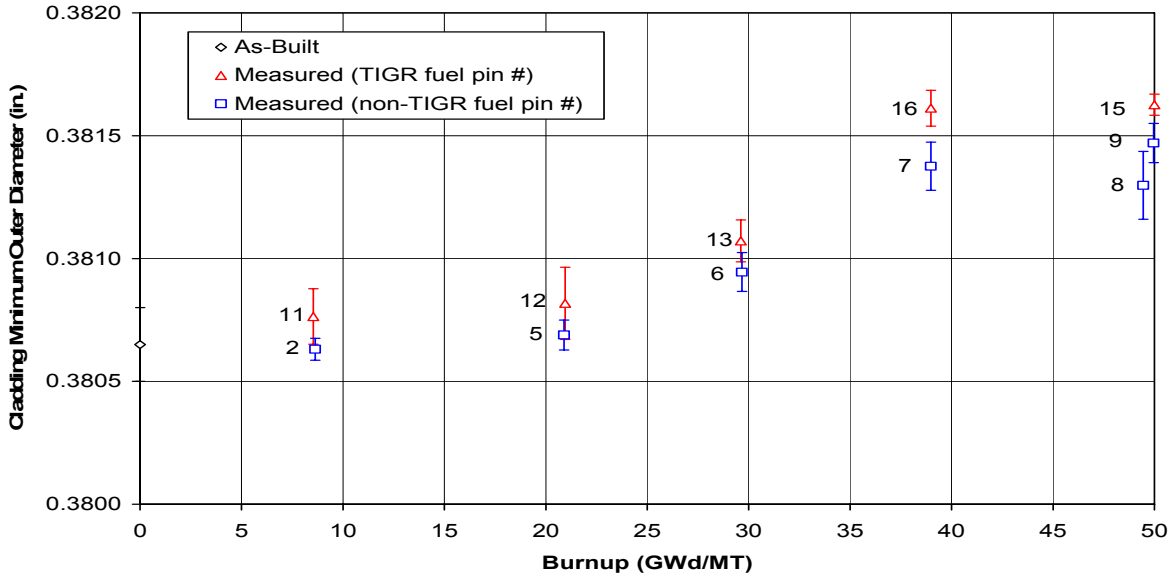

Fig. 6.4. Cladding outer diameter valleys as functions of fuel type and burnup.

The fuel pin cladding inner diameter will now be considered. The nominal construction inner diameter of the Zircaloy cladding is 0.3290 in. (with tolerances of +0.0005 and –0.0000 in.). The preirradiation value for the cladding inner diameter for Fuel Pins 2, 5–9, 11–13, 15, and 16 is reported as 0.3290-to-0.3294 in. (Table 6.2).

The postirradiation inner diameter is obtained from the PIE measurement of the outer diameter by subtracting the cladding thickness as measured directly from photographic enlargements of the metallographic mounts. For the 30-, 40-, and 50-GWd/MT PIE MET mounts, the original location of the mount face is precisely known; therefore, the cladding outer diameter is known within the uncertainty range of the FPMA measurement. However, for the 9- and 21-GWd/MT mounts, diametral measurements cannot be precisely correlated with the original locations of the mount faces. Hence, the average of the FPMA measurements for these fuel pins is used as the cladding outer diameter, from which the inner

diameter is calculated. Finally, the uncertainties* in the cladding outer diameter and cladding thickness are propagated inward to yield the uncertainty in the inner diameter.

A compilation of the mean measured cladding thickness for each metallographic mount is given in Table 6.5 and plotted versus fuel burnup in Figure 6.5. As shown, the measured cladding thicknesses of all mounts lie within the preirradiation as-built values plus uncertainties.

With both cladding growth and the observed outward creep, the cladding thickness should decrease with burnup. Considering constant volume with the maximum observed creep (Fuel Pin 16, Table 6.4, and Figure 6.1), the associated decrease in cladding thickness is about 0.09 mil. The uncertainties listed for the thickness measurements in Table 6.5 are generally 2–4 times this value. In other words, the measurement uncertainties are much greater than the expected decrease in the cladding thickness.

Table 6.5. Fuel pin cladding thickness

Irradiation phase	Met. mount ident. number	Capsule	Fuel Pin	Clad thickness (in.)	Uncertainty in clad thickness (mils)
I	6139	1	2	0.02592	0.31
I	6140	1	2	0.02581	0.45
I	6141	1	2	0.02582	0.37
II	6143	9	12	0.02573	0.44
II	6144	9	12	0.02580	0.39
II	6145	2	5	0.02570	0.33
II	6146	2	5	0.02565	0.31
III	6161	3	6	0.02569	0.20
III	6162	3	6	0.02546	0.11
III	6163	10	13	0.02554	0.19
III	6164	10	13	0.02536	0.18
IV, Part 1	6218	4	7	0.02575	0.15
IV, Part 1	6219	4	7	0.02559	0.13
IV, Part 1	6220	4	7	0.02557	0.15
IV, Part 1	6223	13	16	0.02562	0.18
IV, Part 1	6225	13	16	0.02537	0.07
IV, Parts 2&3	6254	6	9	0.02567	0.49
IV, Parts 2&3	6255	6	9	0.02579	0.33
IV, Parts 2&3	6256	6	9	0.02564	0.67
IV, Parts 2&3	6258	6	9	0.02581	0.33
IV, Parts 2&3	6260	12	15	0.02586	0.29
IV, Parts 2&3	6261	12	15	0.02560	0.29
IV, Parts 2&3	6263	5	8	0.02572	0.22
IV, Parts 2&3	6264	5	8	0.02583	0.48
IV, Parts 2&3	6265	5	8	0.02547	0.35
IV, Parts 2&3	6267	5	8	0.02581	0.25
IV, Parts 2&3	6268	5	8	0.02588	0.46

*Because their mount faces may represent anywhere between valley and peak, the uncertainties stated in Table 6.4 for the cladding outer diameters of Fuel Pins 2, 11, 5, and 12 are probably underestimated. Referring to Figure 6.3, the average difference between peak and valley is about 0.3 mil, which is as much as four times greater than the uncertainties listed in Table 6.4. The difference between the average and the average peak and average valley is assumed to be the uncertainty for these fuel pins.

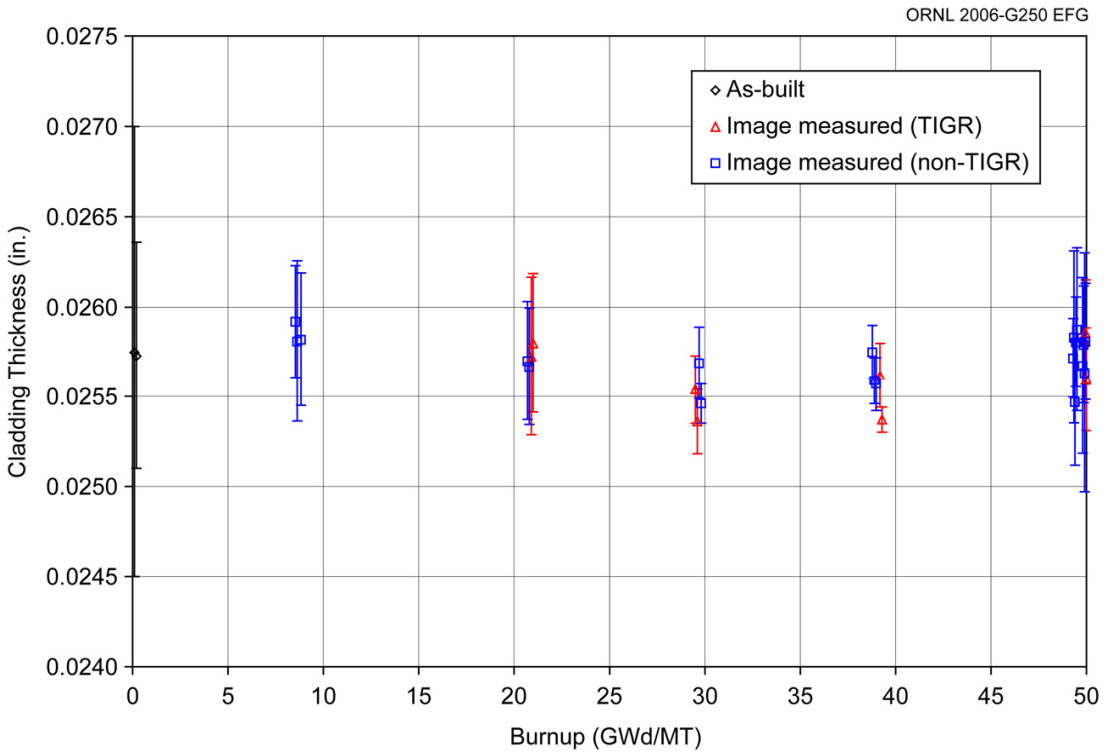

Fig. 6.5. Cladding thickness vs burnup—cold dimensions.

The calculated cladding inner diameter and associated uncertainty for each metallographic mount are presented in Table 6.6.

The cladding inner diameters are shown as a function of burnup in Figure 6.6. The derivation of the pellet diameters is discussed in the next two sections. However, it is of interest to consider these in conjunction with the cladding diameters, so the pellet diameters are shown in the lower portion of Figure 6.6.

In previous "Implications" reports (References 39 and 40), the figure similar to Figure 6.6 showed a decrease in the pellet equivalent diameters from the unirradiated state to the Phase I burnup (~9 GWd/MT), then an increase in diameter (at ~21 GWd/MT burnup) followed by another decrease (at ~29.6 GWd/MT). Obviously, if taken literally, the behavior suggested by the 21-GWd/MT data would be contrary to expected fuel response. Fuel densification and swelling occur simultaneously in the early phases of fuel irradiation; and with the rate of densification being greater than the swelling rate, the pellet equivalent diameter will decrease. Once densification is complete (by about 10- to 15-GWd/MT burnup), solid and gaseous fission product induced fuel swelling will increase monotonically with irradiation. For these early Implications reports, a graphical technique had been employed to analyze the 9- and 21-GWd/MT MET mounts, and subsequent (30- and later) MET mount analyses had used the imaging software (Reference 41). These earlier PIE MET mounts have been reanalyzed with the Image-Pro software, and these data (for the 9- and 21-GWd/MT MET mounts) are employed in this chapter.

The data shown in Figure 6.6 represent fuels irradiated at different axial positions relative to the ATR core at different LHGRs and should be treated as independent observations. R. N. Morris (ORNL) has assessed the data in Table 6.6 assuming an uncertainty of 0.5% for the diameter measurements. With this uncertainty, he is able to pass a smooth curve representative of densification followed by swelling through all data ranges. His results are close to those obtained by CARTS and discussed in Section 6.4,

Table 6.6. Fuel pin cladding inner diameter

Irradiation phase	Met. mount ident. number	Capsule	Fuel Pin	Clad inner diameter (in.)	Uncertainty in inner diameter (mils)
I	6139	1	2	0.32890	0.63
I	6140	1	2	0.32911	0.90
I	6141	1	2	0.32909	0.74
II	6143	9	12	0.32951	0.90
II	6144	9	12	0.32936	0.80
II	6145	2	5	0.32944	0.68
II	6146	2	5	0.32950	0.68
III	6161	3	6	0.32958	0.42
III	6162	3	6	0.33007	0.24
III	6163	10	13	0.33007	0.38
III	6164	10	13	0.33068	0.37
IV, Part 1	6218	4	7	0.33006	0.31
IV, Part 1	6219	4	7	0.33035	0.27
IV, Part 1	6220	4	7	0.33018	0.32
IV, Part 1	6223	13	16	0.33060	0.37
IV, Part 1	6225	13	16	0.33066	0.17
IV, Parts 2&3	6254	6	9	0.33015	0.98
IV, Parts 2&3	6255	6	9	0.33017	0.66
IV, Parts 2&3	6256	6	9	0.33038	1.34
IV, Parts 2&3	6258	6	9	0.32954	0.66
IV, Parts 2&3	6260	12	15	0.32993	0.59
IV, Parts 2&3	6261	12	15	0.33068	0.58
IV, Parts 2&3	6263	5	8	0.32973	0.45
IV, Parts 2&3	6264	5	8	0.32979	0.97
IV, Parts 2&3	6265	5	8	0.33056	0.71
IV, Parts 2&3	6267	5	8	0.32995	0.51
IV, Parts 2&3	6268	5	8	0.32941	0.92

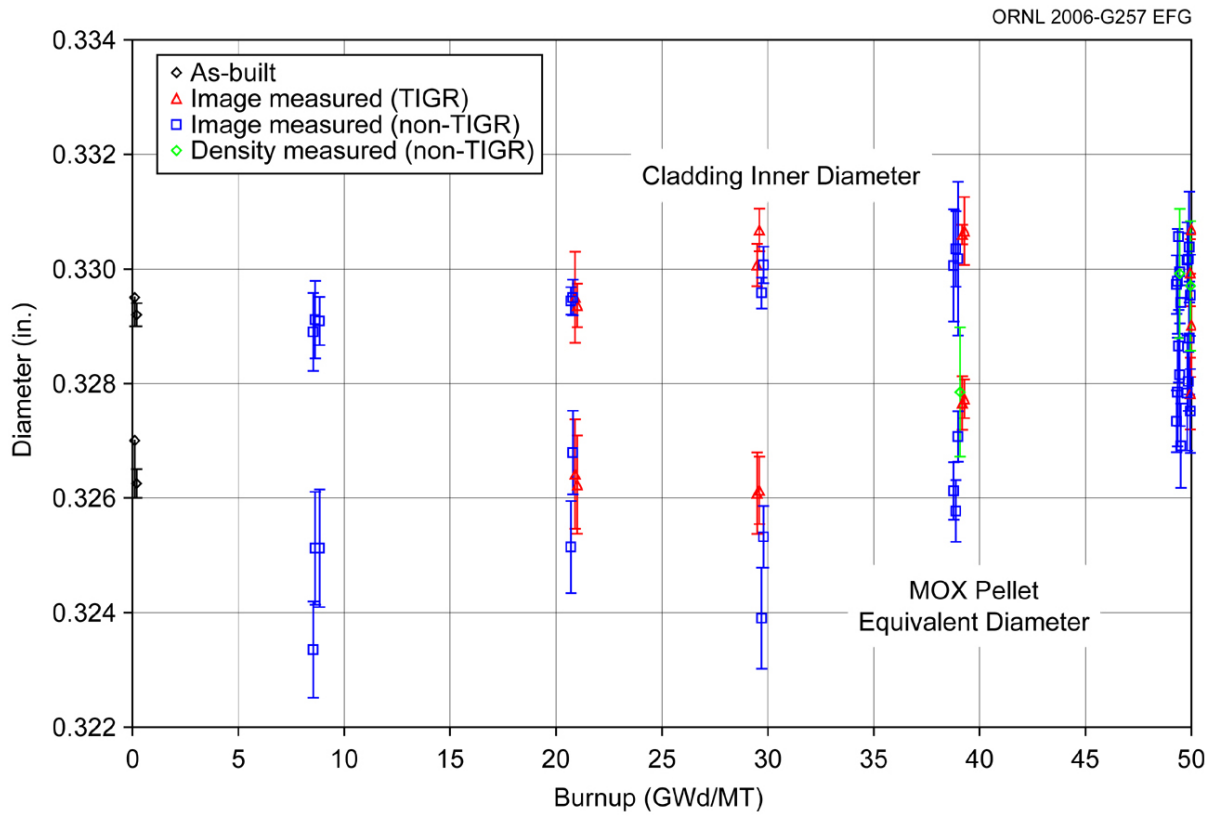

Fig. 6.6. Clad and pellet diameters vs burnup—cold dimensions.

with a slightly lower extent and period of densification, and a swelling rate of 0.07% as compared with the 0.077% used with CARTS and FRAPCON-3.

Section 6.4 assesses the "general" trends in the fuel densification and swelling behavior.

6.2.4 Fuel to Clad Radial Gap

Reviewing the metallographic mounts illustrated for the 50-GWd/MT withdrawals in Chapter 5 of References 35 and 36, the appearance of the fuel is normal (with cracks caused by thermal stresses during ATR operation and thermal cycling, i.e., startups and shutdowns) and is consistent with the appearances of MET mounts prepared during previous PIEs.

Under hot cell conditions, there is less than 1°C difference between capsule surface and fuel centerline temperatures, both of which are within 25°C of the hot cell ambient temperature (about 30°C). At such low temperatures, there is little thermal expansion of the capsule components; thus, existing cracks within the fuel and the peripheral gaps between fuel and cladding are all larger than during reactor operation. High fuel temperatures during operation and the associated thermal expansion tend to close the internal cracks and peripheral gaps.

From the enlarged photographs of the metallographic mounts, the free area within the fuel pin (gaps and cracks) can be estimated. This free area does not include the porosity within the fuel or the "pullouts" in the mounts (which did not exist during irradiation and were subsequently caused by loss of friable material during mount preparation).

Generally, the portion of the free area within the cracks (at hot cell conditions) for these metallographic mounts is greater than the portion in the peripheral gap. The total free area can be used to calculate an equivalent peripheral gap (that is, an adjusted gap between the fuel and cladding which includes all the free area within the fuel pin). In effect, the pellet segments are considered to be pushed together so that the internal cracks disappear. This approach is consistent with the manner in which fuels codes treat the gap and cracks within the fuel pin. This equivalent gap can then be compared with the predictions of the fuels codes (such as CARTS).

The adjusted fuel-to-clad peripheral gap and uncertainty for each metallographic mount are listed in Table 6.7.

The fuel-to-clad radial gap is shown as a function of burnup in Figure 6.7. Prior to irradiation, the construction tolerances allow the radial gap to range from 1.00 to 1.75 mils. This construction range and also the smaller as-built range are illustrated at the zero burnup point in Figure 6.7.

As shown in Figure 6.7, the gap at ~8.6 GWd/MT burnup is wider than the gap at BOL. This behavior is prototypic of commercial fuel; that is, the fuel densifies (i.e., shrinks in volume) in the early phase of irradiation.

Table 6.7. Fuel to clad radial gap

Irradiation phase	Met. mount ident. number	Capsule	Fuel Pin	Adjusted gap (mils)	Uncertainty in gap (mils)
I	6139	1	2	2.78	0.28
I	6140	1	2	2.00	0.20
I	6141	1	2	1.99	0.36
II	6143	9	12	1.55	0.16
II	6144	9	12	1.57	0.16
II	6145	2	5	2.15	0.22
II	6146	2	5	1.36	0.14
III	6161	3	6	2.84	0.38
III	6162	3	6	2.38	0.24
III	6163	10	13	2.00	0.30
III	6164	10	13	2.28	0.23
IV, Part 1	6218	4	7	1.97	0.20
IV, Part 1	6219	4	7	2.29	0.23
IV, Part 1	6220	4	7	1.55	0.16
IV, Part 1	6223	13	16	1.47	0.15
IV, Part 1	6225	13	16	1.47	0.15
IV, Parts 2&3	6254	6	9	1.16	0.12
IV, Parts 2&3	6255	6	9	1.07	0.11
IV, Parts 2&3	6256	6	9	0.79	0.08
IV, Parts 2&3	6258	6	9	1.01	0.10
IV, Parts 2&3	6260	12	15	1.05	0.11
IV, Parts 2&3	6261	12	15	0.83	0.08
IV, Parts 2&3	6263	5	8	1.19	0.12
IV, Parts 2&3	6264	5	8	0.97	0.10
IV, Parts 2&3	6265	5	8	0.96	0.10
IV, Parts 2&3	6267	5	8	0.90	0.09
IV, Parts 2&3	6268	5	8	1.25	0.13

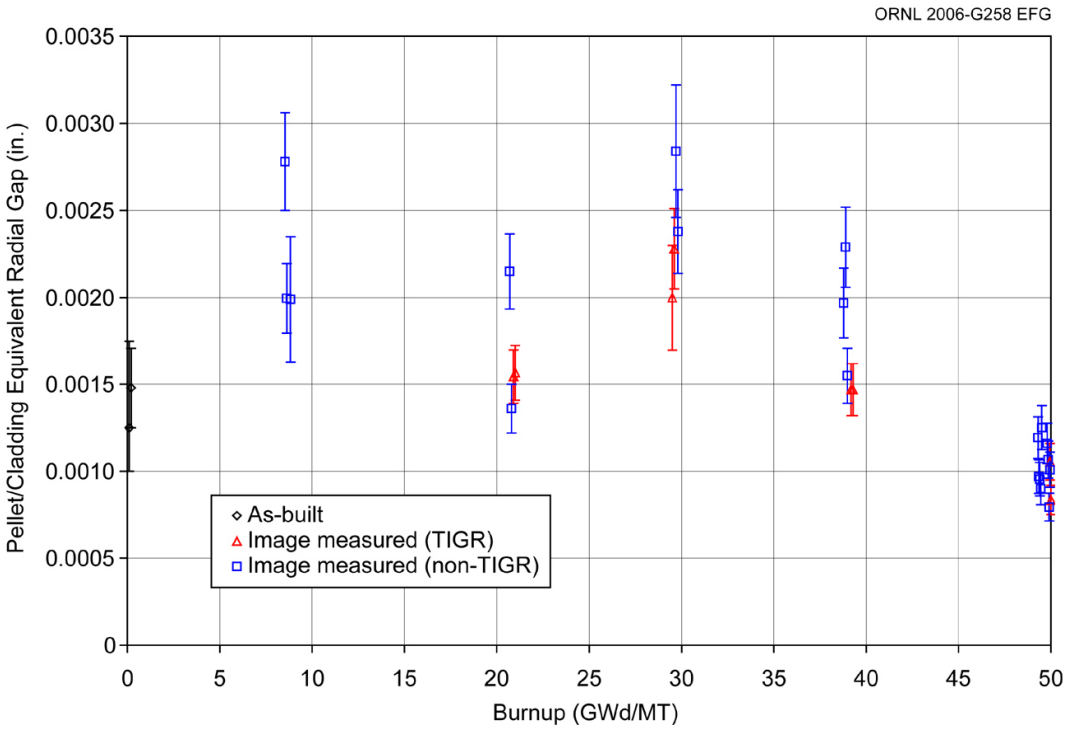

Fig. 6.7. Equivalent radial gap vs burnup—cold dimensions.

The fuel densification and swelling phenomena are discussed in Reference 42 (Chapter 6), including an excellent graphical presentation (Figure 6.1) of commercial fuel (Siemens) densification and swelling. In general, densification is very rapid in the first 10 GWd/MT of burnup and is complete by 10–15 GWd/MT. Fuel densification and swelling are essentially competing effects; early in the irradiation densification dominates and the fuel volume shrinks; but after densification is complete, swelling continues in direct proportion to the burnup.

As noted near the end of Section 6.2.3, the irradiation histories and axial positions relative to the ATR core midplane are different for the fuel pins withdrawn after each irradiation phase. These independent observations should be treated as test data. Section 6.4 assesses the general trends in the observed fuel behavior.

6.2.5 Fuel Pellet Outer Diameter

Given the Zircaloy cladding inner diameter (from Section 6.2.3) and the equivalent peripheral gap between fuel and cladding (from Section 6.2.4), the fuel outer diameter (i.e., in the absence of internal cracking) can be calculated by subtracting the latter from the former. The fuel pellet outer diameter and uncertainty for each metallographic mount are given in Table 6.8.

The range of pellet equivalent diameters is shown as a function of burnup in Figure 6.8. Prior to irradiation, the construction tolerances allow a range in the pellet diameter of 0.3260 to 0.3270 in. This is the initial range shown at zero burnup.

During the Phase IV, Part 1 PIE, a device [Fuel Pin Volume Measuring Apparatus (FPVMA), see Reference 43] was developed to determine the fuel pin free volume via a gas-back-fill technique. An adaptation of this device also allows the determination of a specimen volume. The volume of a small sample (~0.5 in.) of cladding and fuel from Fuel Pin 7 was measured; and, given the sample mass, the

Table 6.8. Fuel outer diameter

Irradiation phase	Met. mount ident. number	Capsule	Fuel Pin	Fuel pellet outer diameter (in.)	Uncertainty in diameter (mils)
I	6139	1	2	0.32335	0.84
I	6140	1	2	0.32512	0.98
I	6141	1	2	0.32512	1.03
II	6143	9	12	0.32642	0.95
II	6144	9	12	0.32623	0.86
II	6145	2	5	0.32514	0.81
II	6146	2	5	0.32679	0.73
III	6161	3	6	0.32390	0.88
III	6162	3	6	0.32532	0.54
III	6163	10	13	0.32608	0.71
III	6164	10	13	0.32613	0.59
IV, Part 1	6218	4	7	0.32612	0.50
IV, Part 1	6219	4	7	0.32577	0.54
IV, Part 1	6220	4	7	0.32707	0.44
IV, Part 1	6223	13	16	0.32766	0.47
IV, Part 1	6225	13	16	0.32773	0.34
IV, Parts 2&3	6254	6	9	0.32783	1.01
IV, Parts 2&3	6255	6	9	0.32804	0.70
IV, Parts 2&3	6256	6	9	0.32879	1.35
IV, Parts 2&3	6258	6	9	0.32752	0.69
IV, Parts 2&3	6260	12	15	0.32782	0.63
IV, Parts 2&3	6261	12	15	0.32901	0.61
IV, Parts 2&3	6263	5	8	0.32734	0.52
IV, Parts 2&3	6264	5	8	0.32785	0.98
IV, Parts 2&3	6265	5	8	0.32865	0.74
IV, Parts 2&3	6267	5	8	0.32815	0.54
IV, Parts 2&3	6268	5	8	0.32691	0.95

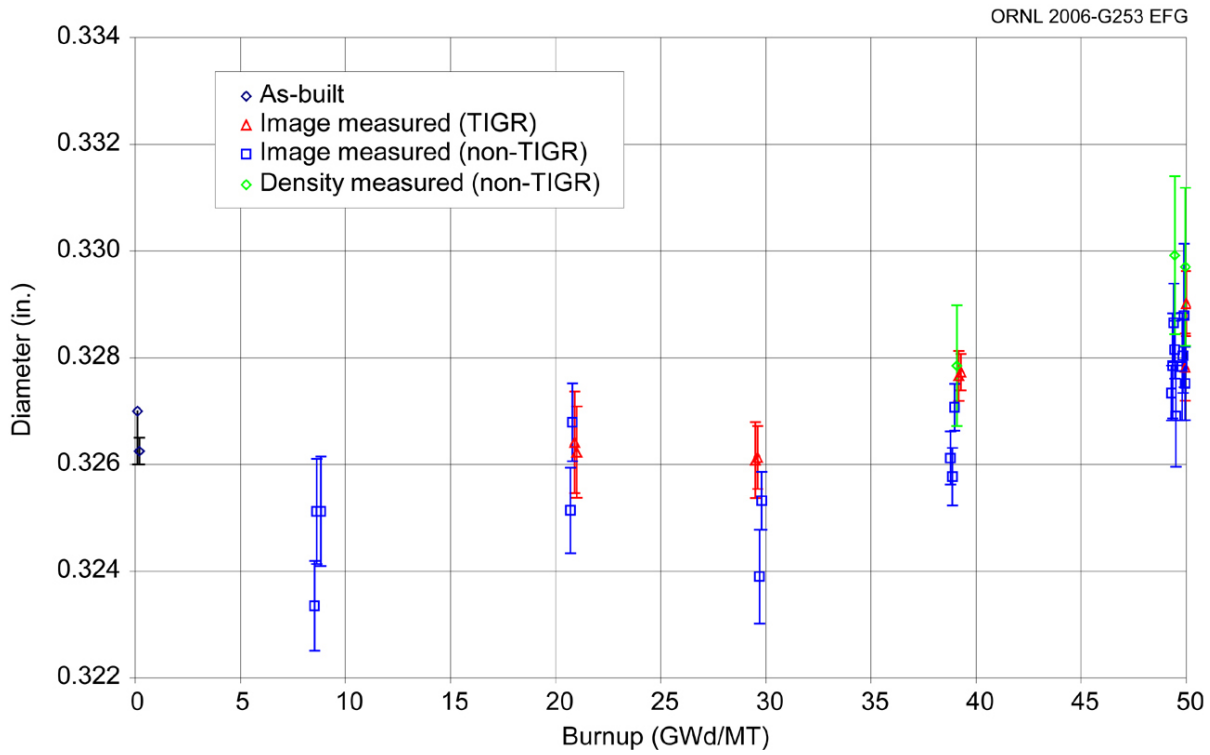

Fig. 6.8. MOX pellet equivalent diameter vs burnup—cold dimensions.

fuel density was determined to be 10.2 g/cm^3. This irradiated fuel density (at a burnup of ~40 GWd/MT) compares with an initial unirradiated density of 10.4 g/cm^3. Given the irradiated fuel density of 10.2 g/cm^3 and data from the LANL QA report on the non-TIGR treated fuel pellets, the pellet diameter can be estimated. The density-based pellet diameter is 0.32785 in. (±1.1 mils). The FPVMA was also employed with samples from Fuel Pins 8 and 9.

These pellet diameters determined via these fuel density measurements (one at 40- and two at 50-GWd/MT burnups) are plotted (green symbols) in Figure 6.8 and agree very well with the pellet diameters determined via the FPMA and MET mount measurements.

As explained previously, Figure 6.8 demonstrates the initial fuel densification. After the initial densification phase, pellet expansion (due to fuel swelling, which is directly proportional to burnup) will continue until the irradiation is stopped.

6.3 Conclusions from Dimensional Inspections of the Metallographic Mounts

Three primary conclusions can be drawn from the PIE metrological results and the dimensional inspections of the fuel pin metallographic mounts:

- Outward creep of the fuel pin Zircaloy cladding in the MOX test irradiation is conclusive. For the 30GWd/MT withdrawal fuel pins [6 and 13, Reference 39)], the cladding diameter (at hot-cell conditions) had expanded by about 0.45 mil (an increase of 0.12%). The 40-GWd/MT withdrawal fuel pins (7 and 16, Reference 40) are found to be expanded by ~0.24% (or 0.94 mils). The 50-GWd/MT withdrawal fuel pins (8, 9, and 15, this report) are found also to be expanded by ~0.24%.

- By contrast, the valleys along the 9- and 21-GWd/MT withdrawal fuel pin surfaces were within the as-built tolerances of the unirradiated cladding. Cladding creep must be included in the predictive analyses of the fuels codes (and especially the CARTS analyses) for this MOX test irradiation.

- A cladding creep model for these test irradiations and a comparison with literature data for Zircaloy creep is presented in Chapter 7.

- Taken literally, the data ranges corresponding to 9- and 21-GWd/MT burnups in Figures 6.6 and 6.7 might be interpreted to indicate an unexpected variation in the extent of fuel swelling. However, it is believed that the associated measurement uncertainties have been underestimated. These data and uncertainties have been reassessed and are included in this chapter. It has been demonstrated that with uncertainty increased to just 0.5% for these fuel pins, a smooth curve representative of the expected densification and swelling can be passed through all data ranges.

- The fuel behavior (cracking, densification, and swelling) of the MOX test fuel is normal and prototypic of commercial fuel.

6.4 Assessment of MOX Fuel Densification and Swelling

The CARTS code employs two fuel densification and swelling models (as selected by user input):

- the first is from ESCORE (Reference 44), which is an industry-derived code approved by the U.S. NRC;
- the second is from FRAPCON-3 (Reference 45), which is the NRC's audit code.

Both models have been used in the CARTS safety analyses conducted previously for the MOX test irradiation. The only degrees of freedom in applying these models are the amount of fuel densification and the period during which the densification occurs, both user-input.

In the 30-GWd/MT PIE Implications report (Reference 39), the CARTS code was employed in simulating the MOX test Phase I, Phase II, and Phase III irradiations. For these simulations, a fuel densification and swelling model (either ESCORE or FRAPCON) was selected, and then the ultimate fuel densification and the densification period were varied until a best fit to the measured data was accomplished. For the ESCORE model, this best fit was obtained with 4.0% densification complete by 15 GWd/MT. For the FRAPCON model, the best fit was obtained with 2.0% densification complete by 10 GWd/MT.

The ESCORE fuel swelling model is different for constrained and unconstrained fuel/clad configurations; in Reference 39, this resulted in a cross-over of the predicted fuel pellet equivalent diameters for the CARTS simulations [(1) dimensions predicted for maximum initial gas gaps and (2) dimensions predicted for minimum initial gas gaps, see Figure 5.8 in Reference 39]. Given this unusual model behavior and the very high "best fit" fuel densification of 4% for the ESCORE model, the decision was made to use only the FRAPCON-3 fuel densification/swelling model in subsequent CARTS calculations. In addition, the "best fit" value of 2.0% densification (complete by 10 GWd/MT) for the FRAPCON-3 model is very reasonable with respect to the commercial LWR fuel experience (where 1–2% fuel densification is normally observed).

The data developed in Sections 6.2.4 and 6.2.5 permit a reassessment of the MOX test fuel densification, based on PIE observations, that is appropriate when applying the FRAPCON model in CARTS in describing the MOX fuel behavior. The CARTS simulations employ a model (discussed in Chapter 7) for the actual cladding creep as illustrated in Figure 6.4.

For this reassessment of the fuel densification, the CARTS code has been employed in simulating the MOX test Phase I; Phase II; Phase III; Phase IV, Part 1; and Phase IV, Part 3 irradiations. For these simulations, only the FRAPCON-3 fuel densification and swelling model is used. The ultimate fuel densification and densification period are then varied until a best fit to the test data (i.e., Figures 6.7 and 6.8) emerges. For the FRAPCON model, the best fit value is 2.0% with densification complete by 10 GWd/MT [the same as obtained for the 30-GWd/MT withdrawals (Reference 39) and the 40-GWd/MT withdrawals (Reference 40)].

The results of these simulations and model predictions using these values are illustrated in Figures 6.9, 6.10, and 6.11. The two dashed lines represent the results of CARTS simulations employing the FRAPCON-3 fuel swelling model for minimum and maximum initial gas gaps. As shown, the predicted pellet diameters and the pellet-to-clad gaps for the two gas gap extremes are essentially parallel throughout the irradiation.

The FRAPCON-3 fuel swelling model is relatively simple because it includes a constant swelling rate (solid fission product induced) of 0.77% per 10 GWd/MT; there are no model components for (1) gaseous fission products, (2) temperature dependence, or (3) constrained/unconstrained fuel. The FRAPCON-3 model represents a least squares fit to experimental and industrial data.

In addition to the CARTS simulations, the ORNL version of FRAPCON-3 (version 1.3, modified at ORNL for MOX usage) was executed for the MOX test Phases I; II; III; IV, Part 1; and IV, Part 3 irradiations. The FRAPCON-3 models contain 15 axial segments (one per fuel pellet) and use the axial power peaking factors (as a function of burnup) calculated by G. Chang at INL (Reference 46). The results of these FRAPCON-3 calculations are presented in Figures 6.9, 6.10, and 6.11. (Note: FRAPCON-3 does not have a model for cladding creep-out.) Since the axial power in the fuel rod is determined via the mean LHGR and the axially-dependent peaking factors, the burnup of each individual pellet is different; the burnup ranges are given in Table 6.4 and illustrated in Figures 6.9, 6.10, and 6.11.

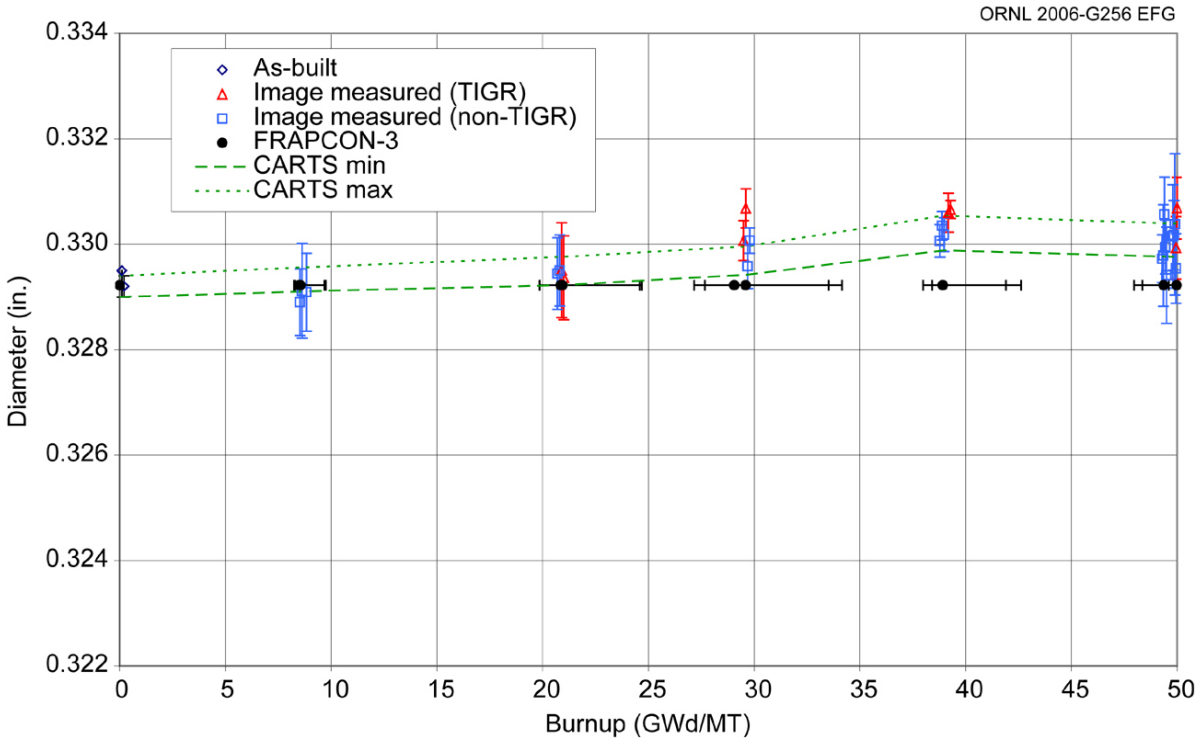

Fig. 6.9. Clad inner diameters vs burnup—cold dimensions.

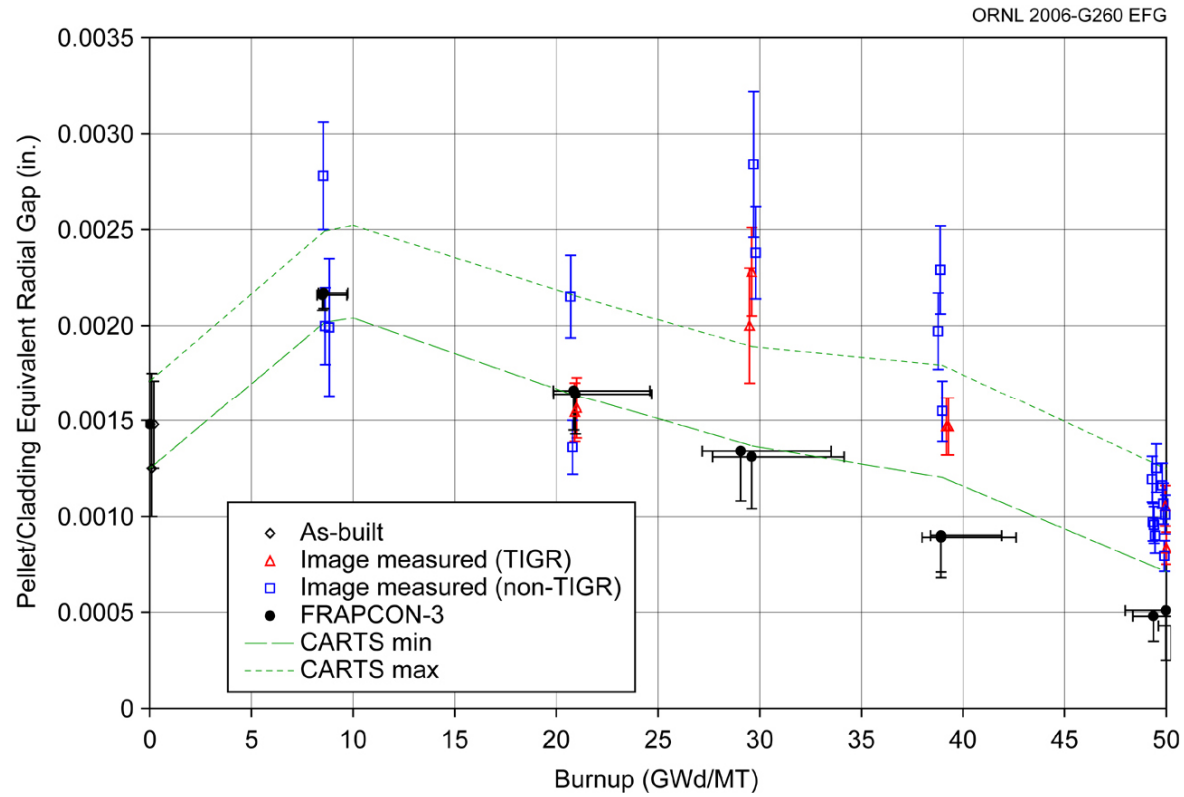

Fig. 6.10. Equivalent radial gap vs burnup—cold dimensions.

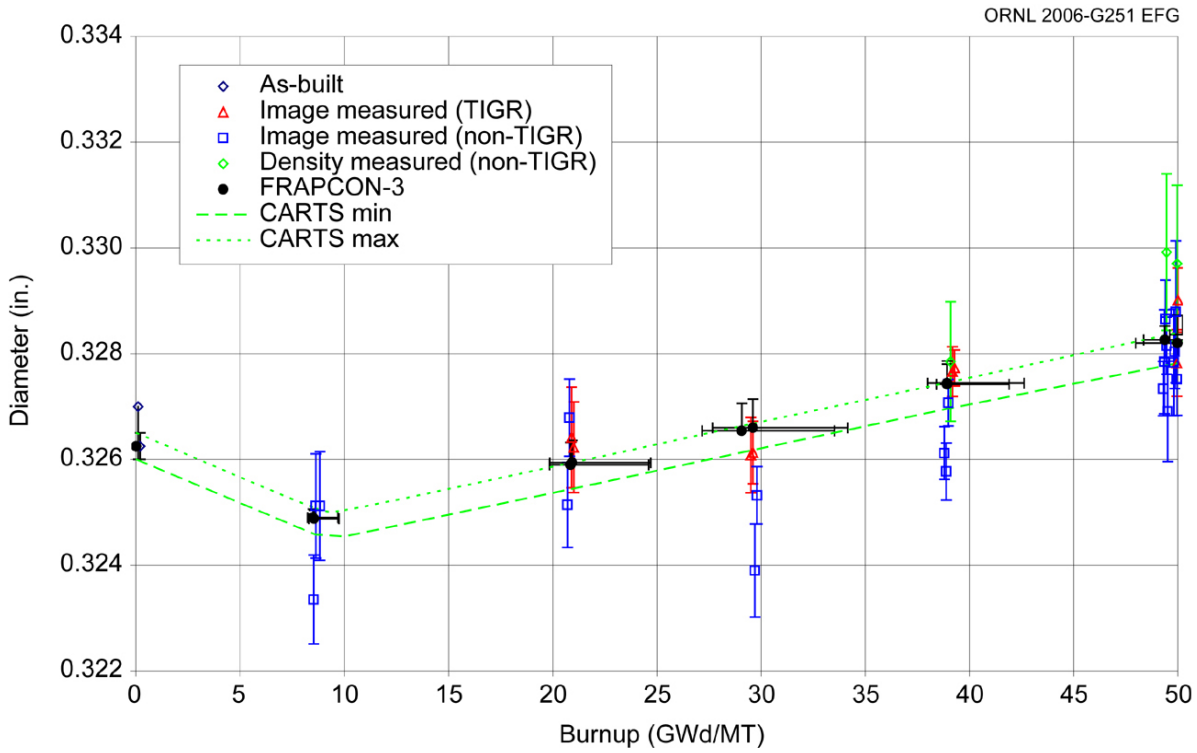

Fig. 6.11. MOX pellet equivalent diameter vs burnup.

The FRAPCON-3 code does not have a model for cladding creep-out, as used in CARTS; thus, as shown in Figure 6.9, the inner diameter remains constant (which reduces the computed pellet-to-cladding gap as given in Figure 6.10). The FRAPCON-3 prediction of the fuel pellet diameter (using 2.0% fuel densification) reasonably reflects the MOX test results (see Figure 6.11) and is very close to the CARTS predictions.

Comparisons of the CARTS and FRAPCON-3 simulation results for Capsule 6/Fuel Pin 9 and Capsule 12/Fuel Pin 15 are given in Sections 8.3.2 and 8.3.5, respectively. Also, comparisons of the CARTS and FRAPCON-3 simulation results for Capsule 5/Fuel Pin 8 are given in Section 9.3.2.

7. MODEL FOR OUTWARD CLADDING CREEP

7.1 Introduction

Two types of permanent deformations are observed in the MOX fuel cladding: (1) ridges located at axial positions adjacent to the pellet-to-pellet interfaces and (2) irradiation-enhanced outward creep.

In Chapter 6 of the 30-GWd/MT PIE implications report (Reference 39), cladding ridges were found to be caused by differential thermal expansion of the fuel pellets in the axial direction. At hot conditions during reactor operation, the MOX pellets warp into hourglass shapes, and localized contact with the cladding occurs with sufficient force to cause yielding of the cladding at locations adjacent to the pellet-to-pellet interfaces. Because of the unique design of the MOX test fuel pins with small initial gap widths between the MOX pellets and the cladding, this yielding occurs on initial heatup before initiation of any pellet densification or swelling.

Further information on pellet hourglassing and the finite element (ABAQUS code) analyses performed for the pellet/cladding/capsule wall interactions can be found in the discussion in Chapter 6 of Reference 39. These clearly demonstrate the high cladding stresses (>yield) imposed by pellet-clad mechanical interaction at the pellet-to-pellet interfaces. Subsequent ABAQUS analyses (with component relocations associated with yielding) predicted permanent plastic deformations (ridges) overlying the pellet ends, while low cladding stresses prevailed at the pellet midplane.

The other type of permanent cladding deformation, irradiation-enhanced creep, is discussed in this chapter [model development originally presented in Chapter 6 of the 40-GWd/MT PIE implications report (Reference 40)]. Because the MOX test fuel pins are contained inside of stainless steel capsules, they are exposed to low pressure on the outer surfaces of their cladding, rather than the high pressures that exist on the outside of commercial light water reactor fuel. As fuel pin internal pressures increase during the MOX test irradiations (primarily because of fission gas releases, but also enhanced by helium releases), the MOX cladding experiences small tensile hoop stresses and slow outward creep, rather than the more normal compressive hoop stresses and inward creep-down of commercial fuel. In addition to cladding hoop stresses, other parameters that affect creep rates include fast neutron flux and cladding temperatures.

The measurements and calculations performed to determine the outward creep of the MOX test cladding are presented in Section 7.2. These measurements are then compared in Section 7.3 with similar data found in the literature. Finally, a revised empirical cladding creep correlation for use in the CARTS code is presented in Section 7.4.

7.2 MOX Cladding Outward Creep Measurements

A summary of the measured outer diameters of the MOX test cladding has been provided in Section 6.2.3. Figure 6.2 shows an example of an outer profile measured along the length of Fuel Pin 7. This profile results from the combined effects of ridging caused by pellet hourglassing and irradiation-enhanced creep. In order to separate the amount of creep from the ridging effects, an average value was calculated for the minimum diameters of the 15 valleys visible in the Figure 6.2 profile. The average minimum diameter of 0.38138 in. for Fuel Pin 7 is then plotted in Figure 6.4 along with diameters calculated in similar manners for the other fuel pins. Figure 6.4 therefore displays the measured cladding creep in the absence of ridging effects as a function of burnup.

One observation about Figure 6.4 is that there is negligible cladding creep at low burnup. The uncertainty bands at burnups of 8 and 21 GWd/MT overlap the uncertainty band associated with the drawing and as-built tolerances at zero burnup. A second observation about Figure 6.4 is that the fuel pins with

TIGR-treated pellets undergo more cladding creep than the non-TIGR fuel pins. This second observation is consistent with the measured fission gas release ranges and fuel pin internal pressures presented in Table 3.1. At each burnup level in Table 3.1, the fission gas releases and internal pressures are greater for the TIGR-treated fuel (Fuel Pins 12, 13, 16, and 15) than for the non-TIGR fuel. The higher internal pressures generate higher tensile hoop stresses in the cladding, which increases the outward cladding creep.

Traditional creep theory splits the process into the two stages illustrated in Figure 7.1: an initial period with a rapid (but declining) creep rate (called primary creep) followed by a second period with a lower constant creep rate (called secondary creep). For cladding that is exposed to a constant hoop stress, the inelastic creep strain ε as a function of exposure time t is typically expressed with the following equation:

$$\varepsilon = \varepsilon_p\left(1 - e^{-a\,t}\right) + \dot{\varepsilon}_s\,t \quad , \tag{7.1}$$

where ε_p is the total primary strain, $\dot{\varepsilon}_s$ is the constant secondary strain rate, and a is a decay constant.

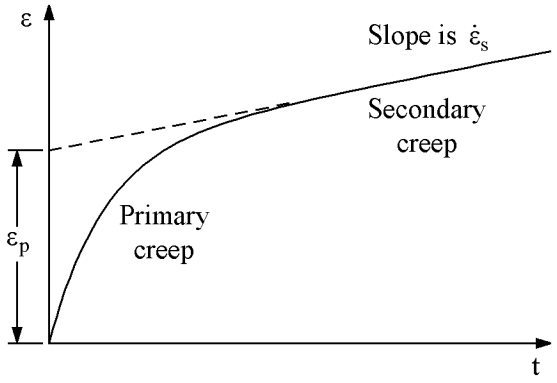

Fig. 7.1. Illustration of traditional creep theory with process divided into primary and secondary creep regions.

Special treatment is necessary for applying Equation (7.1) to the MOX cladding measurements (discussed at the beginning of this section) because the fuel pin internal pressures P_{fp} and associated cladding hoop stresses S_h increase during the MOX test irradiations, and these stresses are not measured at the hot conditions during reactor operation. First, the CARTS code is used to estimate the cladding hoop stresses as a function of exposure time during the irradiations using the following equation:

$$S_h = \frac{P_{fp}\,ID - P_c\,OD}{OD - ID} \quad , \tag{7.2}$$

where P_c is the capsule internal pressure, and ID and OD are the inner and outer cladding diameters, respectively. The CARTS calculations are described in Section 7.4; the predicted results used for this creep analysis are those representing the mean initial gas gap widths. Other relevant input parameters for the individual CARTS calculations were selected such that the predicted results best match the fission gas releases and fuel pin pressures measured in the ORNL hot cell after completion of the irradiations.

Then Equation (7.1) is converted into a special form by combining the effects of cladding hoop stress and exposure time together into a "cumulative cladding stress × exposure product" y as follows:

$$y = \int_0^t S_h \, dt \quad , \tag{7.3}$$

$$\varepsilon = \varepsilon_p \left(1 - e^{-b\,y} \right) + c\,y \quad , \tag{7.4}$$

where b and c are similar to a and $\dot{\varepsilon}_s$ in Equation (7.1), but have different units.

CARTS calculations were performed for Fuel Pins 5, 12, 6, 13, 7, 16, 9, 15, and 8, and values for the cumulative cladding stress times exposure products are listed in Table 7.1. Table 7.1 also lists the cladding inelastic hoop strains calculated from the measured minimum outer diameters shown in Figure 6.4. When the last two columns of Table 7.1 are plotted in Figure 7.2, the shape resembles the curve in Figure 7.1.

7.3 Outward Creep Data Found in Literature

Limited creep data are available in the literature for cladding with tensile (rather than compressive) hoop stresses caused by high internal pressures. Other factors that also have a significant impact on cladding creep include (1) fast neutron flux, (2) cladding temperature, and (3) the type and initial state of the cladding (preirradiated, stress relieved, etc.). The MOX test cladding is fresh (not previously irradiated), stress-relieved annealed (SRA) Zircaloy-4. During the MOX fuel irradiations, cladding temperatures range from 200 to 400°C and fast neutron fluxes are about 2×10^{13} neutron/(cm^2•s).

Three sources of outward creep data were located for cladding and operating conditions similar to the MOX test irradiations. Reference 47 provides creep data measured in a dedicated test rig in the Halden Reactor in Norway. Of particular interest is Figure 6 in Reference 47, which is for fresh SRA Zircaloy-4 cladding irradiated at a constant tensile hoop stress of 52 MPa for an exposure time of 208 effective full-power days. Other relevant Halden parameters are a cladding temperature of 375°C and a fast neutron flux of 4.3×10^{13} neutron/(cm^2•s). Figure 6 in Reference 47 also provides a curve fit of the creep data in the form of Equation (7.1). This curve fit was converted into the form of Equation (7.4) [using

Table 7.1. MOX test cladding stress and strain parameters

Fuel Pin No.	Total exposure (effective-full-power days)	Maximum cladding hoop stress (MPa)	Cumulative cladding stress × exposure product (MPa•day)	Cladding inelastic hoop strain
5	383	0.66	114	0.000102
12	383	0.86	137	0.000441
6	615	1.01	276	0.000775
13	615	1.40	351	0.001109
7	904	6.26	1885	0.001907
16	904	7.31	2132	0.002527
9	1307	7.21	3533	0.002154
15	1307	8.79	4268	0.002564
8	1462	3.01	1747	0.001702

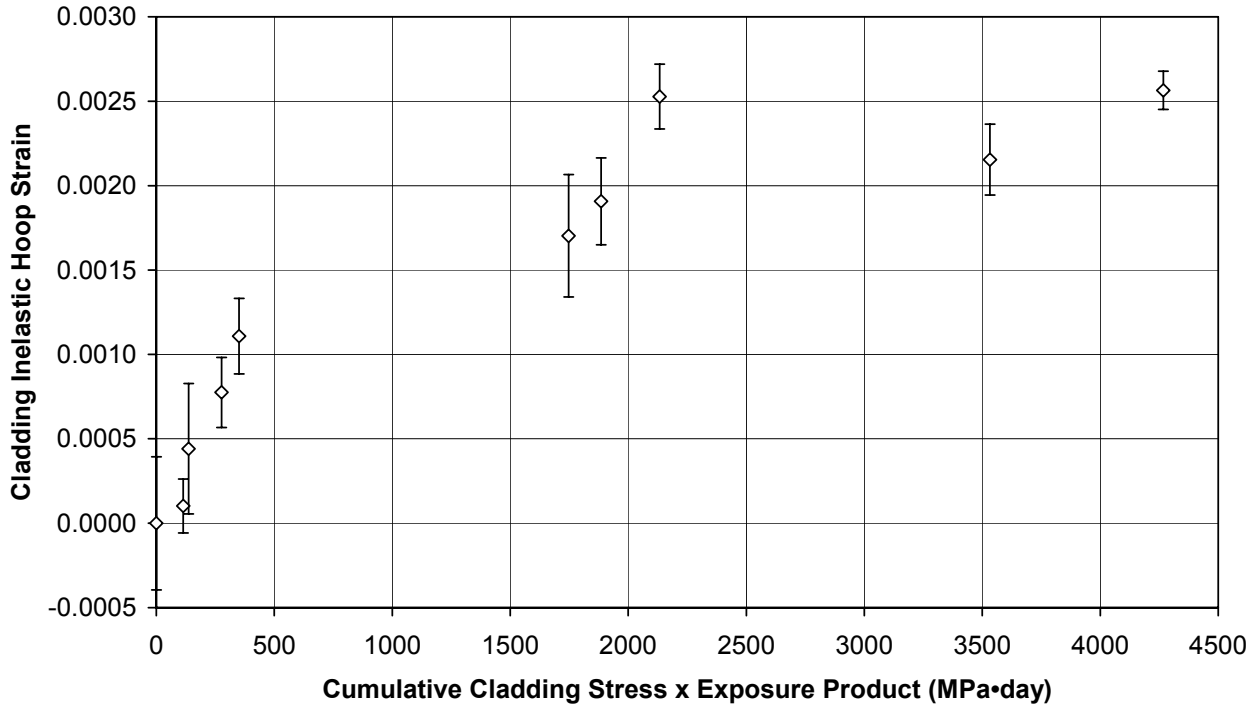

Fig. 7.2. MOX test cladding outward creep with error bars indicating measurement uncertainties.

Equation (7.3)], and the Halden data are plotted in Figure 7.3 along with the MOX test cladding data from Figure 7.2. Although there is a large difference in the hoop stresses associated with the Halden data (52 MPa) and the MOX data (<7.4 MPa), the use of the cumulative cladding stress times exposure product appears to provide a good way for correlating the creep strains.

Reference 48 by Soniak et al. contains outward creep data measured at the SILOE Test Reactor in France for SRA low-tin Zircaloy-4 cladding exposed to constant tensile hoop stresses ranging from 60 to 120 MPa. Two of the 60-MPa-stress data sets were selected for comparison with the measured MOX cladding outward creep. The first Soniak et al. data set is for a cladding temperature of 380°C and a fast neutron flux of 2.08×10^{14} neutron/(cm^2•s); the other data set is for a cladding temperature of 350°C and a fast neutron flux of 1.65×10^{14} neutron/(cm^2•s). The relevant creep data were obtained from Figure 4 of Reference 48, and then converted into a format suitable for plotting with the other data in Figure 7.3. Although the lowest-exposure points of the Soniak et al. data only overlap the highest-exposure points of the MOX test data, the Soniak et al. data for the 350°C cladding temperature appear to be in better agreement with the MOX data.

A detailed correlation for outward cladding creep is presented by Limback and Andersson in Reference 49. This correlation was calibrated against an extensive series of thermal and in-reactor creep tests for both Zircaloy-2 and Zircaloy-4 claddings. This Limback/Andersson correlation has been used (with proper SRA Zircaloy-4 input parameters) to calculate cladding creep strains for the Halden and Soniak et al. test conditions (cladding hoop stress, temperature, and fast neutron flux) described in the preceding paragraphs. The predicted results from the Limback/Andersson correlation are plotted in Figure 7.3, and generally good agreement is observed with the respective test data. Note that the Limback/Andersson correlation could not be directly applied for the MOX test conditions because the low cladding hoop stresses (<7.4 MPa) are below the range for which the correlation was calibrated.

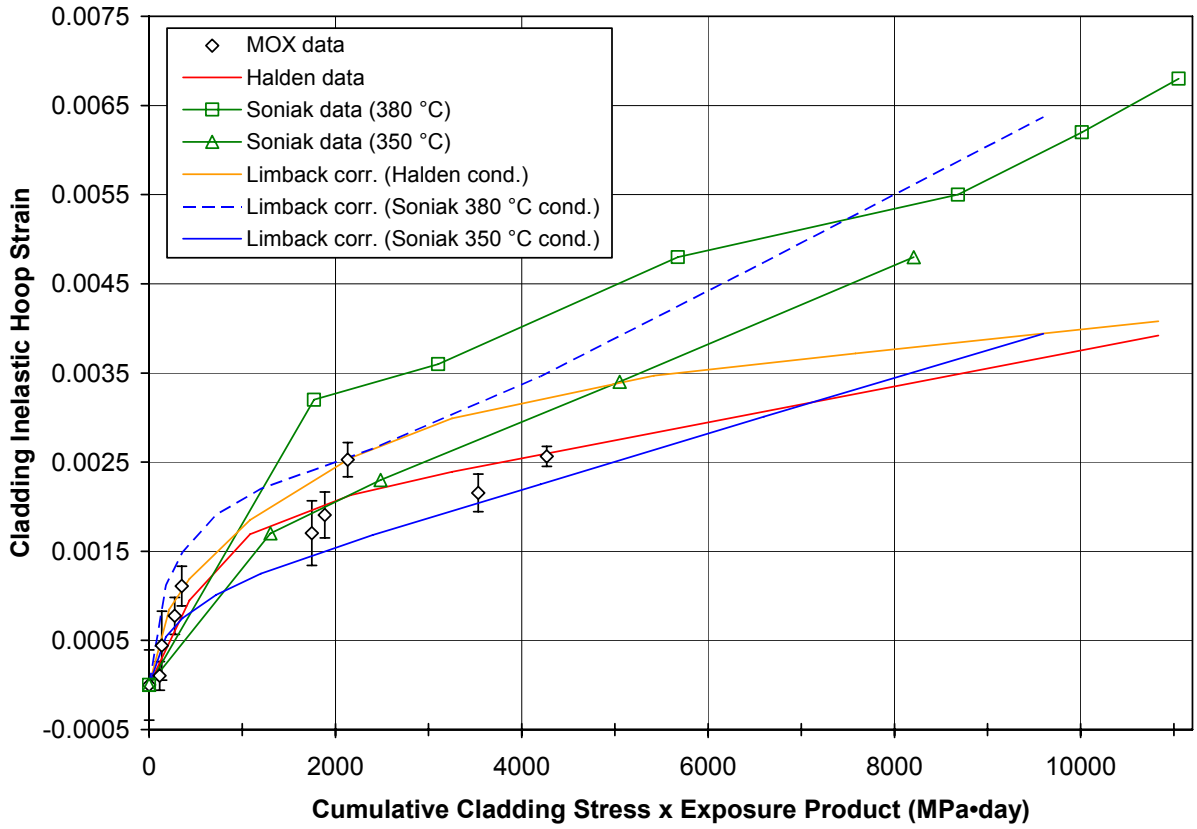

Fig. 7.3. Comparison of MOX test measurements with other outward creep data for SRA Zircaloy-4 claddings.

7.4 CARTS Outward Creep Empirical Correlation

Figure 7.3 provides strong evidence that Equations (7.3) and (7.4) can be used to accurately represent the cladding outward creep that occurs during the MOX test irradiations. The 21- and 30-GWd/MT MOX data points are located in the primary creep region, the two points for burnups of 40 GWd/MT and the Fuel Pin 8 50-GWd/MT data appear to be near the transition between the primary and secondary creep regions, and the remaining 50-GWd/MT data are in the secondary creep region.

An empirical correlation based upon Equation (7.4) that fits the MOX test outward creep data through the 40 GWd/MT burnup data (reported in Reference 40) is

$$\varepsilon = 0.0018\left(1 - e^{-0.00181\,y}\right) + 2.5(10)^{-7}\,y \quad , \tag{7.5}$$

where the inelastic creep strain is unitless, and y is the cumulative cladding stress times exposure product [defined in Equation (7.3)] with units of MPa•day.

Given the additional 50-GWd/MT data, the empirical correlation has been revised as follows:

$$\varepsilon = 0.0015\left(1 - e^{-0.0022\,y}\right) + 2.1(10)^{-7}\,y \quad . \tag{7.6}$$

Figure 7.4 illustrates the empirical correlations given by Equations (7.5) and (7.6) and also shows the MOX test and other experimental data in greater detail for the low exposures. The parameters of Equation (7.6) were determined to best fit all of the MOX test data points.

This empirical correlation applies for limited conditions: SRA Zircaloy-4, tensile hoop stresses, and cladding temperatures and fast neutron fluxes similar to the MOX irradiation conditions. Also, because the time-dependent cladding hoop stresses upon which the correlation is based were estimated from CARTS code calculations, this correlation is only considered applicable for use within CARTS.

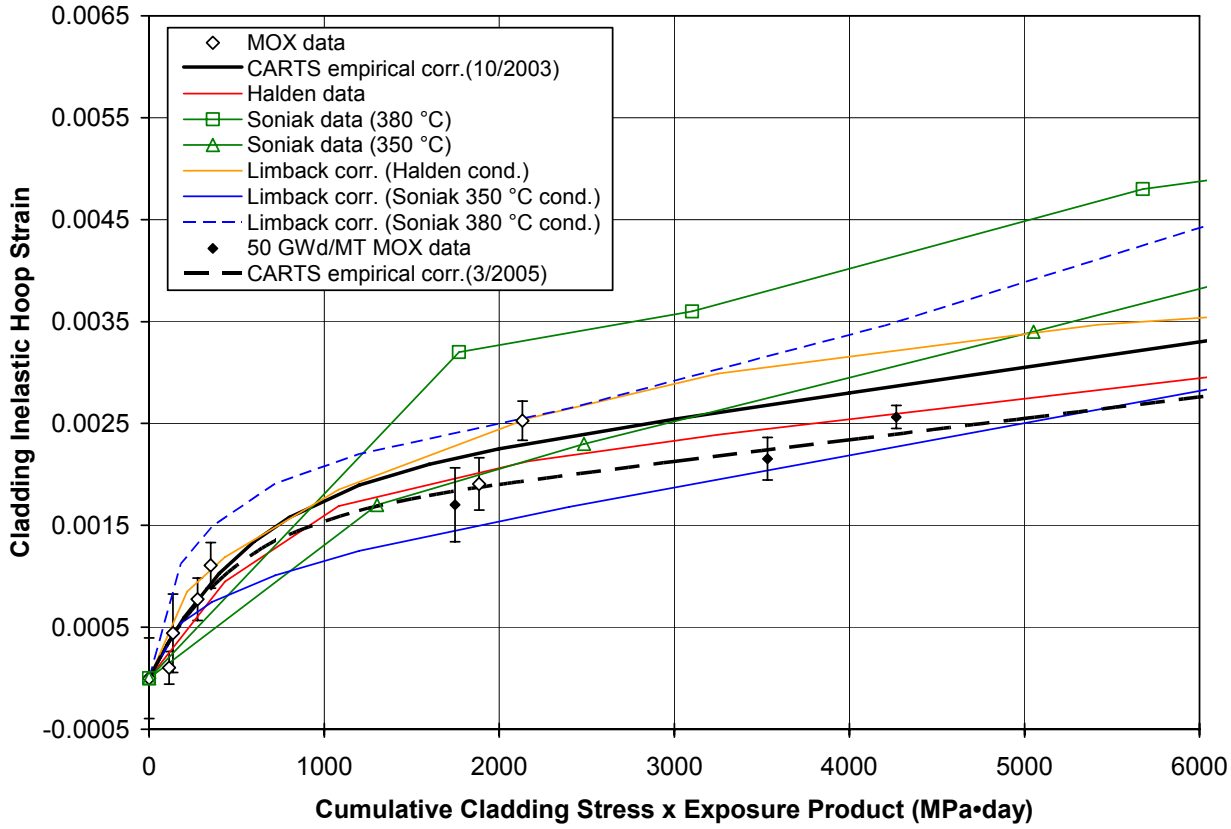

Fig. 7.4. Empirical correlation used in CARTS code for MOX test cladding outward creep.

8. POST-PIE CODE CALCULATIONS OF CAPSULES 6 AND 12 IRRADIATION RESPONSE

8.1 Introduction

The CARTS and FRAPCON-3 calculations for Capsules 6 and 12 presented in Chapter 2 of the 50-GWd/MT Quick Look Report (Reference 50) were performed in advance of the PIE. Given the re-assessment of the MOX fuel densification and swelling through a burnup of 50 GWd/MT presented in Section 6.4, the changes in the cladding creep model discussed in Section 7.4, and the final PIE fission gas release determinations for Capsules 6 and 12 (Table 3.7), it is desirable to determine the extent to which these modeling changes (fuel densification, length of densification period, cladding creep during irradiation, fission gas release) affect the predicted behavior of Capsules 6 and 12. These post-PIE analyses are presented in this section, together with a comparison to the earlier predictions.

These CARTS and FRAPCON-3 calculations for Capsules 6 and 12 are based upon the actual burnup accumulations and corresponding average LHGRs experienced during ATR cycles 118A through 132C (Phases II–IV). As described in the previous sections, these capsules occupied a series of paired test assembly locations, symmetric with respect to the ATR core. Hence, their irradiation histories are similar.

The CARTS calculations predict the conditions at the pellet midplane as a function of increasing burnup and do not include representation of pellet cracking and relocation or pellet end-effects such as hourglassing.

FRAPCON-3 simulations require (1) the capsule irradiation history (same as CARTS) and (2) the time-dependent cladding surface temperatures predicted by CARTS as a boundary condition.

8.2 Differences in Pre- and Post-PIE Modeling Assumptions

The cold, unirradiated capsule and fuel pin dimensions employed in the Reference 50 analyses and in this Chapter are based on the as-built component dimensional ranges given in Table 6.2.

The irradiation histories for Capsules 6 and 12 were provided in Sections 2.2 to 2.6 of Reference 50; the final version of the irradiation histories is given in Sections 3.2 to 3.6 of Volume 1 (Reference 35). There are no differences in these histories.

As noted in Chapters 6 and 7, cladding creep (outward) is occurring during the MOX test irradiation. For the pre-PIE analyses, the assumed creep-out of the cladding followed the empirical model given by Equation (7.5) (based on the irradiation data through the 40-GWd/MT PIEs). The post-PIE calculations employ the empirical fit [Equation (7.6)] to all the MOX test data through the 50-GWd/MT PIEs.

As shown in Figure 7.4, the post-PIE creep model [Equation (7.6)] predicts less cladding expansion than the pre-PIE formulation [Equation (7.5)]; thus, there is potential for the width of the predicted pellet-to-clad gas gaps to decrease, with a concomitant decrease in fuel temperatures due to higher gap conductances.

CARTS modeling of fuel densification requires user-input of the degree of densification, and the length of the densification period. The pre-PIE parameters are based on the assessment given in Section 5.4 of Reference 40, while the post-PIE parameters are based on the reassessment given in Section 6.4 of this report. It develops that these densification parameters are the same for both the pre- and post-PIE CARTS calculations, as follows:

- FRAPCON-based models: a maximum of 2% fuel densification achieved during the period of 0–10 GWd/MT burnup.

The cumulative fission gas release affects the gap conductance throughout the CARTS calculation and is controlled via a code input parameter specifying the percent released at 45 GWd/MT. The best estimate values considered for the pre-PIE analyses, based on the European experience and the average LHGRs during Phase II, were 1.3% for Capsule 6 and 1.5% for Capsule 12. Per the CARTS algorithm, this corresponds to releases at 50 GWd/MT of 1.6% and 1.8%, respectively.

The fission gas release percentages employed in the post-PIE calculations for Capsules 6 and 12 correspond to the PIE-measured 7.23% and 8.61%, respectively (see Table 3.7). These fission gas releases are much higher than used in the pre-PIE calculations; thus, the pellet-cladding gap conductance will be lower, resulting in higher fuel temperatures.

Other than these noted differences, all CARTS and FRAPCON-3 code inputs and models for the pre- and post-PIE calculations are the same.

8.3 Post-PIE Results for Capsule Conditions During the Irradiation

In addition to the CARTS simulations, the ORNL version of FRAPCON-3 (version 1.3, modified at ORNL for MOX usage) and the official PNL released version of FRAPCON-3 for MOX (version 2.0) were executed for Capsules 6 and 12.

The CARTS simulations are one-dimensional; the code uses the average LHGR for the 15-pellet stack and therefore does not recognize local variations in power due to axial flux peaking. The FRAPCON-3 model contains 15 axial segments or nodes (one per fuel pellet) and uses the axial power peaking factors (as a function of burnup) calculated by G. Chang at INL (Reference 46). Because the local axial power in the fuel is determined via the mean LHGR and the axially-dependent (and burnup-dependent) peaking factors, the burnup of each individual pellet is different; the calculated and measured axial-burnups given in the PIE Observations Report for Capsule 6 (Reference 35) and shown in Figure 8.1 are in excellent agreement and clearly demonstrate the expected end-peaking in the pellet stack.

There are two notable differences between CARTS and FRAPCON-3 fuel pin modeling: first, FRAPCON-3 does not predict cladding creep-out, while CARTS has specific models for creep-out (based on PIE results); secondly, FRAPCON-3 has models for fuel cracking and relocation, whereas CARTS does not. Both of these code-modeling differences affect the calculated fuel temperatures. It is concluded in Chapter 5 of Reference 40 that the CARTS/FRAPCON-3 predictions provide, respectively, upper and lower bounds for the actual fuel temperature history for these MOX test irradiations.

Also, it should be noted that CARTS specifically accounts for the helium created within and released from the MOX fuel. Although both codes account for the helium charged when the fuel pin is sealed, FRAPCON-3 has no models for helium generation or release.

CARTS was originally developed at ORNL for the MOX test irradiations in the ATR because no available fuels-modeling code (including FRAPCON-3) is applicable for the fuel pin/capsule double-containment configuration utilized in this test irradiation. However, given the time-dependent cladding thermal boundary condition (calculated by CARTS), FRAPCON-3 can simulate these fuel pin irradiation histories. (This assumption of a single temperature over the 6-in. cladding length is acceptable in view of the very small actual axial variation.)

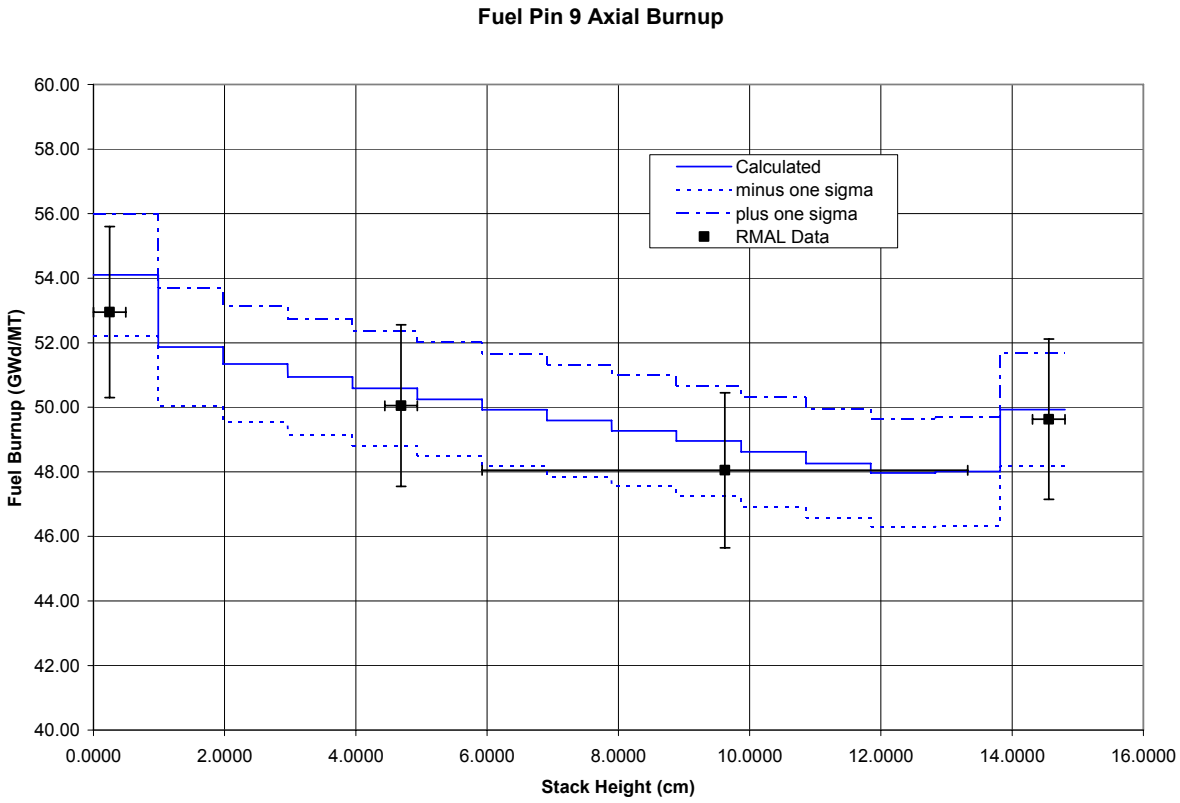

Fig. 8.1. FRAPCON-3 axial burnup predictions for Capsule 6/Fuel Pin 9.

As noted above, each capsule surrounds a fuel pin containing 15 MOX pellets. Each pellet has unique dimensions within the specified fabrication tolerances, so that a spectrum of initial pellet-to-clad gaps exists within each fuel pin. In the following discussions, CARTS results are reported for the minimum, mean, and maximum initial gap widths as defined by the measured fuel pin inner diameter and the tolerance range for initial pellet outer diameter.

Before proceeding to the conditions predicted for the capsule components in the hot cell, it is of interest to first consider the variations in pellet temperatures and diametral gaps as calculated for the period of irradiation, with particular attention to the conditions at the end of Phase IV, Part 3, just prior to removal of the 50-GWd/MT capsules for PIE.

Pre-PIE calculated results are italicized in parenthesis for comparison purposes.

8.3.1 CARTS Results for Capsule 6

Figure 8.2 illustrates the cycle-by-cycle LHGRs as calculated by the MCNP code for Capsule 6, with the corresponding CARTS predictions of pellet mean and centerline temperatures and variations in pellet-clad diametral gap. These parameters are plotted against the integrated internal energy release per unit heavy metal mass. The integrated energy release within the fuel includes power contributions other than fission (such as gamma heating by the ATR core) and thereby differs slightly from fuel burnup. In the interest of avoiding unnecessary clutter, the LHGR trace does not include spikes to near zero to mark the between-cycle reactor outages.

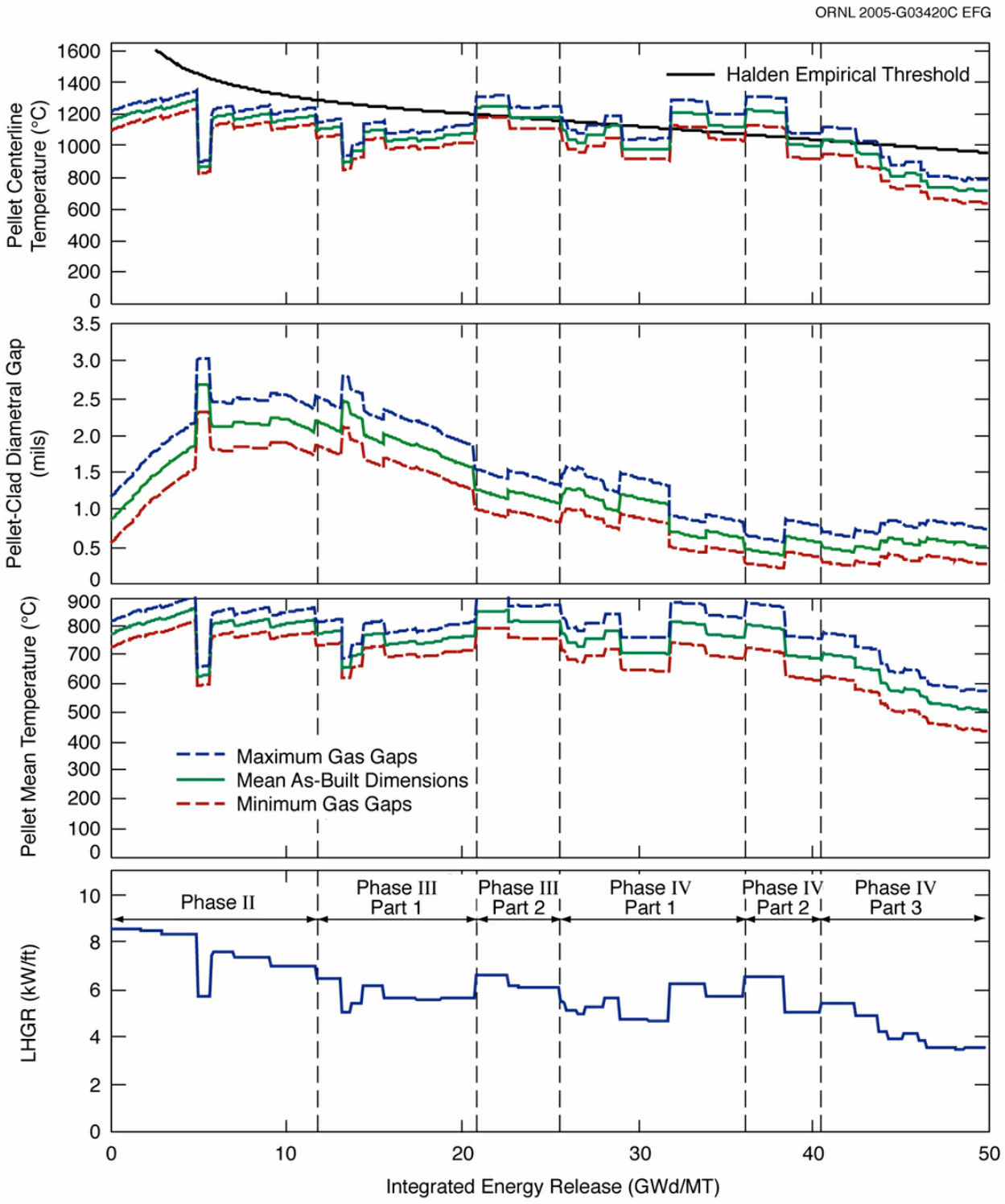

Fig. 8.2. CARTS post-PIE predictions for Capsule 6/Fuel Pin 9. Individual traces show results for maximum, mean, and minimum initial pellet-clad and clad-capsule gap widths.

Three traces are shown in each of the temperature and diametral gap plots, illustrating results as calculated for minimum, mean, and maximum initial pellet-to-clad gap widths. As indicated, the diametral gap is predicted to have remained open throughout the irradiation, with a closest approach to closure (for the case of minimum initial gap) of about 0.22 (*0.26*) mil near the end of cycle 127C (first cycle in Phase IV, Part 2).

Unless otherwise stated, the following discussion will reflect the mean-value traces as shown in Figure 8.2. The ranges between the minimum and maximum traces on the temperature and diametral gap plots indicate the variations associated with pellet-specific differences in the initial pellet-clad gap width.

The highest LHGR experienced by Capsule 6 (8.65 kW/ft) was imposed during its first irradiation cycle, at the beginning of Phase II. As indicated in Figure 8.2, the accompanying pellet thermal expansion corresponds to an initial pellet-clad gap of 0.88 mils. With a progressive pellet densification of 2.0 percent (completed before burnup reaches 10.0 GWd/MT), the pellet diameter begins to decrease, remaining smaller than its initial value throughout Phase II. This pellet shrinkage combined with outward cladding creep causes the predicted pellet-clad diametral gap to more than double [from 0.88 to 2.25 (*2.26*) mils] as Phase II progresses. The maximum gap of 2.69 (*2.74*) mils occurs in the low power cycle 119A-1 in Phase II (at ~5-GWd/MT burnup). The gap width remains greater than its initial value until cycle 126A in Phase IV, Part 1 (integrated energy release of 31.9 GWd/MT).

The increased LHGRs during the last two cycles of Phase IV, Part 1 are due to the shift of the test assembly to the Southwest I-hole. The higher thermal expansion of the fuel (due to the increased LHGRs) during these and the succeeding cycle reduce the gap width to its smallest value during the irradiation.

As shown in Figure 8.2, there are periods during which the calculated pellet temperatures increase while the LHGR remains constant during the Phase II irradiation cycles. This reflects the decreases in gap thermal conductance that accompany both an increasing gap width and the increasing inventories of low-conductivity fission gases.

The predicted temperatures are consistently higher for the calculation based on maximum initial pellet–clad gaps. This follows from the lower effective thermal conductance associated with wider gaps. Figure 8.2 shows that the highest predicted pellet centerline temperature [1351 (*1336*)°C] occurs at the end of the third irradiation cycle of Phase II (4.8 GWd/MT). Because this is more than 1000°C below the melting temperature of the MOX fuel, there is no concern for the possibility of fuel melting.

In the pre-PIE calculations with a predicted fission gas release of 1.6%, the calculated fuel centerline temperature slightly exceeded the Halden empirical threshold (for FGR releases greater than 1%) only in cycles 126B (31.9–34.0 GWd/MT) and 127C (36.2–38.4 GWd/MT). However, for the post-PIE simulations that employ the measured FGR of 7.23%, the fuel centerline temperatures exceed the Halden criteria (see Figure 8.2) for the majority of the irradiation for Phases III, Part 2; IV, Part 1; and IV, Part 2 (a period from 22.7 to 43.9 GWd/MT). Thus, it should be expected that the FGR would significantly exceed 1%. From 15-GWd/MT burnup to the end of the irradiation, the post-PIE fuel centerline temperatures are 10–17% (80–140°C) higher than the pre-PIE calculated temperatures. The lower gap conductance due to the higher fission gas release increases the calculated fuel temperatures.

The post-PIE creep model [Equation (7.6)] predicts less cladding expansion than the pre-PIE formulation [Equation (7.5)] for the same kernel value [y in both Equations (7.6) and (7.5), the cumulative cladding stress × exposure product]; thus, there is potential for the width of the predicted pellet-to-clad gas gaps to decrease, with a concomitant decrease in fuel temperatures due to higher gap conductances. However, with the increased fission gas release in the post-PIE fuel pin simulations, the kernel value is higher (due

to the higher fuel pin pressure); thus, there is more clad creep. As a result, the gap size (Figure 8.2) is nearly the same as the pre-PIE calculations.

No contact between fuel pin and capsule is predicted at any time during the irradiation.

8.3.2 FRAPCON-3 Results for Capsule 6 with Comparisons to CARTS Predictions

A comparison of the CARTS (mean gap) and FRAPCON-3 (versions 1.3 and 2.0) post-PIE calculated fuel centerline temperatures for Capsule 6/Fuel Pin 9 is given in Figure 8.3.

In Figure 8.3, the FRAPCON-3 and CARTS simulations employs mean initial capsule dimensions. As discussed in Section 8.3, the CARTS calculation is one-dimensional; the code uses the average LHGR for the 15-pellet stack and therefore does not recognize local variations in power due to axial peaking. The FRAPCON-3 model has 15 axial nodes (numbered from bottom to top) and does represent the axial power variation. Three FRAPCON-3 axial node centerline temperature plots are included in Figure 8.3: pellet 7 (local LHGR less than average—Node 8), pellet 1 [top pellet (next to gas plenum)—Node 15], and pellet 15 (bottom pellet—Node 1).

The FRAPCON-3 simulations in Figure 8.3 clearly illustrate the end-peaking in the fuel stack (top and bottom) through ~860 days (a burnup of approximately 36 GWd/MT); thereafter, the nodal temperature plots essentially converge as the burnup increases and end-peaking decreases. Capsule 6 was located at the middle or in the upper test assembly positions throughout the irradiation; hence, the highest burnup accumulated in the lower portion of the pellet stack (as shown in Figure 8.1).

There is good agreement between the CARTS and FRAPCON-3 results through approximately 350 reactor-days (~16 GWd/MT burnup). Subsequently, the FRAPCON-3 computed temperatures become increasingly lower than the CARTS predictions. The lower FRAPCON-3 temperatures are

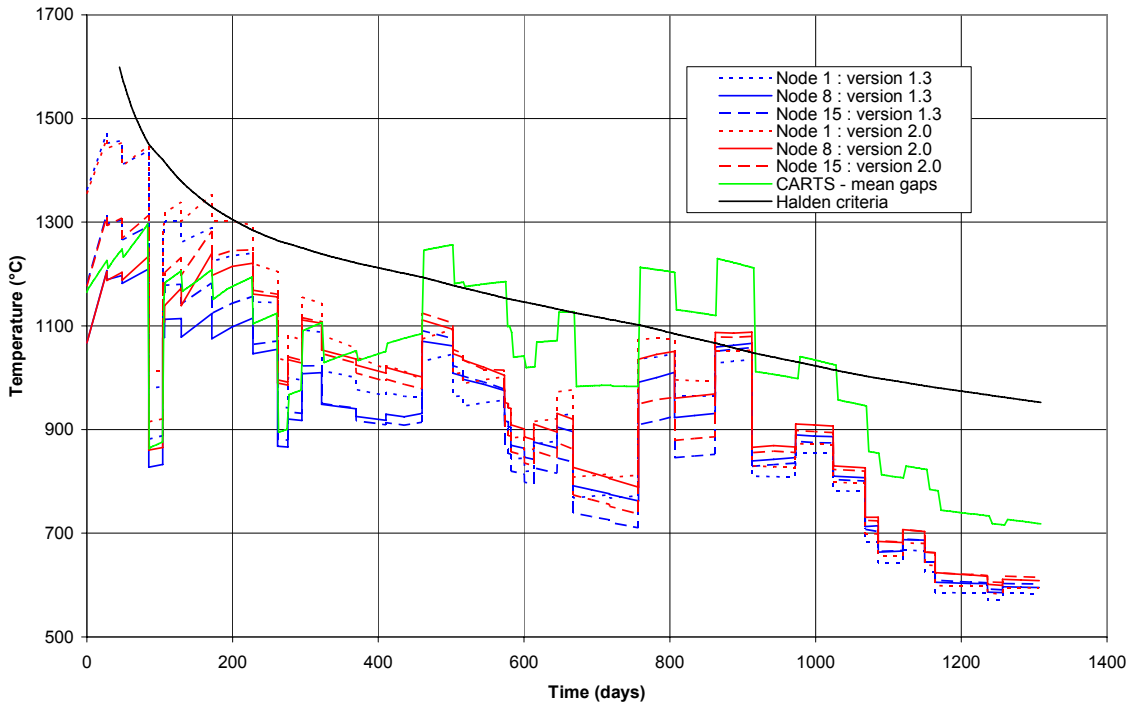

Fig. 8.3. Comparison of CARTS/FRAPCON-3 calculated centerline temperatures for Capsule 6/Fuel Pin 9.

caused by two factors, both contributing to a higher calculated gap thermal conductance: first, CARTS accounts for cladding creep outward, and FRAPCON-3 does not; and, secondly, FRAPCON-3 employs a model for fuel cracking and segment relocation (essentially closing the pellet-to-clad gap), while CARTS does not.

Local temperature less than about 1000°C promotes the transformation of the fuel matrix to the high-burnup structure. For Capsule 6, the maximum fuel centerline temperature (1472°C, FRAPCON-3, Node 1) occurred early at the end of the first cycle and the centerline remained below 1000°C for times greater than 914 reactor-days (average fuel burnups above 38.5 GWd/MT). Burnup within the agglomerates is much higher than the fuel average, and hence the onset of high-burnup structure formation is expected to be visible within the agglomerates in the fuel central region.

The performance of Capsule 6 has been simulated with FRAPCON-3 (version 1.3, modified at ORNL for MOX usage) and FRAPCON-3 (version 2.0, PNL released version applicable for LEU and MOX). There is very close agreement between the predicted fuel temperatures for these two versions through cycle 119A-1 (~104 days in Figure 8.3); thereafter, version 2.0 temperature predictions diverge from version 1.3's. PNL modified the fission gas release model for MOX fuels in version 2.0 and, as shown in Figure 8.4, the predicted FGR for version 2.0 closely matches the PIE data. Version 2.0's FGR prediction is significantly higher than the version 1.3 simulation results after ~104 days; hence, the gap conductance is lower, due to the increased fission gas release, and the resulting fuel temperatures are higher for the version 2.0 predictions. Comparing Figures 8.3 and 8.4, the fission gas release "bursts" (at 100–230, 460, 760, and 860 days) occur when the fuel temperature approaches (or exceeds) the Halden threshold.

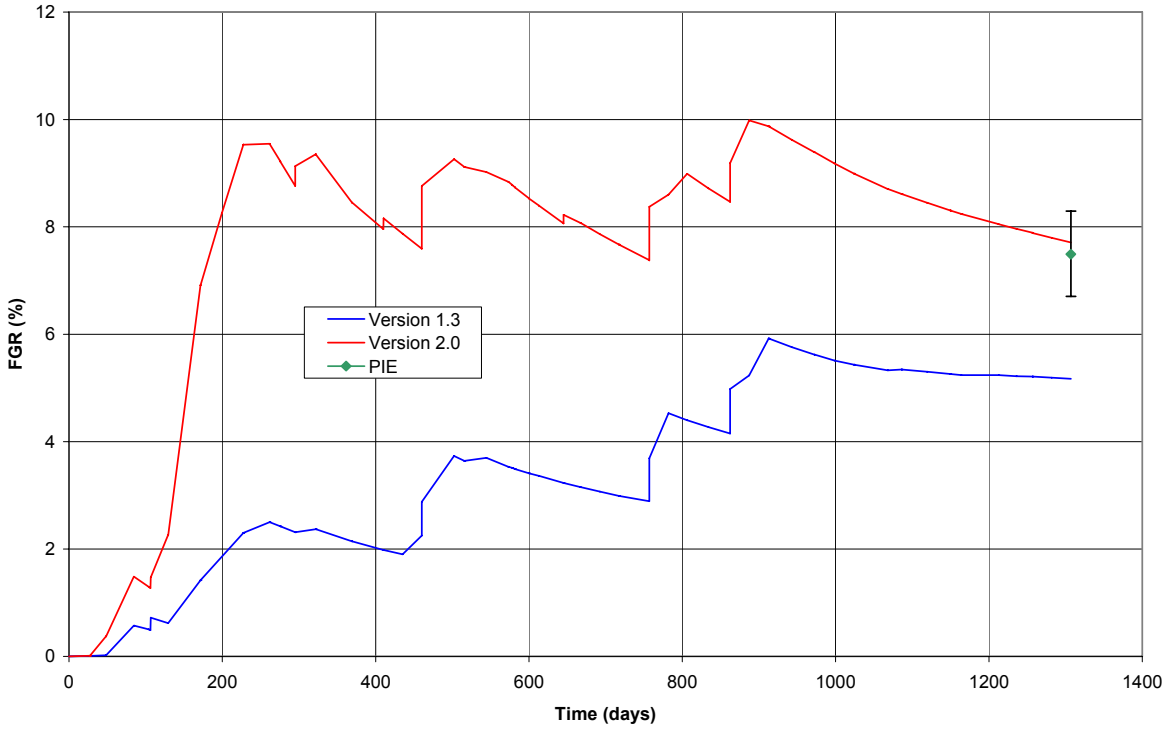

Fig. 8.4. Comparison of FRAPCON-3 calculated fission gas release for Capsule 6/Fuel Pin 9 with PIE data.

8.3.3 The Halden Threshold for Fission Gas Release

The Halden empirical threshold for exceeding one percent fission gas release (described in References 51 and 52) has generally been found applicable to MOX as well as to the UO_2 fuel for which this criterion

was originally developed. The Halden threshold is the burnup BU (GWd/MTHM) curve defined by the relations

$$BU = 0.00567e^{9800/Tc} \quad \text{for burnups} \leq 20 \text{ GWd/MT and}$$
$$BU = 0.120818\,(1365.3 - Tc) \quad \text{for burnups} > 20$$

where Tc is the pellet centerline temperature. For example, for burnups of 10.65 GWd/MT (or greater), fission gas release in excess of one percent is expected if pellet centerline temperature exceeds 1300°C.

8.3.4 CARTS Results for Capsule 12

The CARTS predictions of pellet mean and centerline temperatures and variations in pellet-clad diametral gap for Capsule 12 are shown in Figure 8.5. The three traces shown in each of the temperature and diametral gap plots illustrate results as calculated for minimum, mean, and maximum initial pellet-to-clad gap widths. Similar to the results for Capsule 6, the diametral gap is predicted to have remained open throughout the irradiation, with a closest approach to closure (for the case of minimum initial gap) of 0.21 (*0.25*) mil near the end of cycle 127C (first cycle in Phase IV, Part 2).

Although Capsules 6 and 12 were irradiated in symmetric positions, they have been represented by independent CARTS calculations with separate input data sets based on the specific (measured) fuel pin and capsule dimensions and the individual LHGRs as calculated by the MCNP code at INL. Capsule 12 contains TIGR-treated fuel, and previous PIEs have suggested a difference in fission gas release between the TIGR and non-TIGR fuel.

The differences in the irradiation histories for Capsules 6 and 12 are small. The following discussions for Capsule 12 will reflect the mean-value traces as shown in Figure 8.5. The ranges between the minimum and maximum traces on the temperature and diametral gap plots indicate the variations associated with pellet-specific differences in the initial pellet-clad gap width.

The highest LHGR experienced by Capsule 12 (8.71 kW/ft) was imposed at the beginning of Phase II. As indicated in Figure 8.5, the accompanying pellet thermal expansion produces an initial pellet-clad gap of 0.88 mils. With pellet densification increasing to 2.0% before burnup reaches 10.0 GWd/MT, the pellet diameter initially decreases and remains smaller than its initial value throughout Phase II. This pellet shrinkage combined with outward cladding creep causes the predicted pellet-clad diametral gap to more than double [from 0.88 to 2.18 (*2.22*) mils] during Phase II. The gap width remains greater than its initial value until cycle 126A in Phase IV, Part 1 (integrated energy release of 32 GWd/MT).

The increased LHGRs during the last two cycles of Phase IV, Part 1 are due to the shift of the test assembly to the Southwest I-hole. The higher thermal expansion of the fuel during these and the succeeding cycle reduces the gap width to its smallest value during the irradiation.

As shown in Figure 8.5, the calculated pellet temperatures increase during periods, while the LHGR remains constant during the Phase II irradiation cycles. This reflects the decreases in gap thermal conductance that accompany both an increasing gap width and the increasing inventories of low-conductivity fission gases.

The highest predicted pellet centerline temperature [1354 (*1335*)°C] shown in Figure 8.5 occurs for the case of maximum initial gaps at the end of the third irradiation cycle of Phase II (4.8 GWd/MT). Essentially the same as predicted for Capsule 6, this is more than 1000°C below the melting temperature of the MOX fuel, imposing no concern for fuel melting.

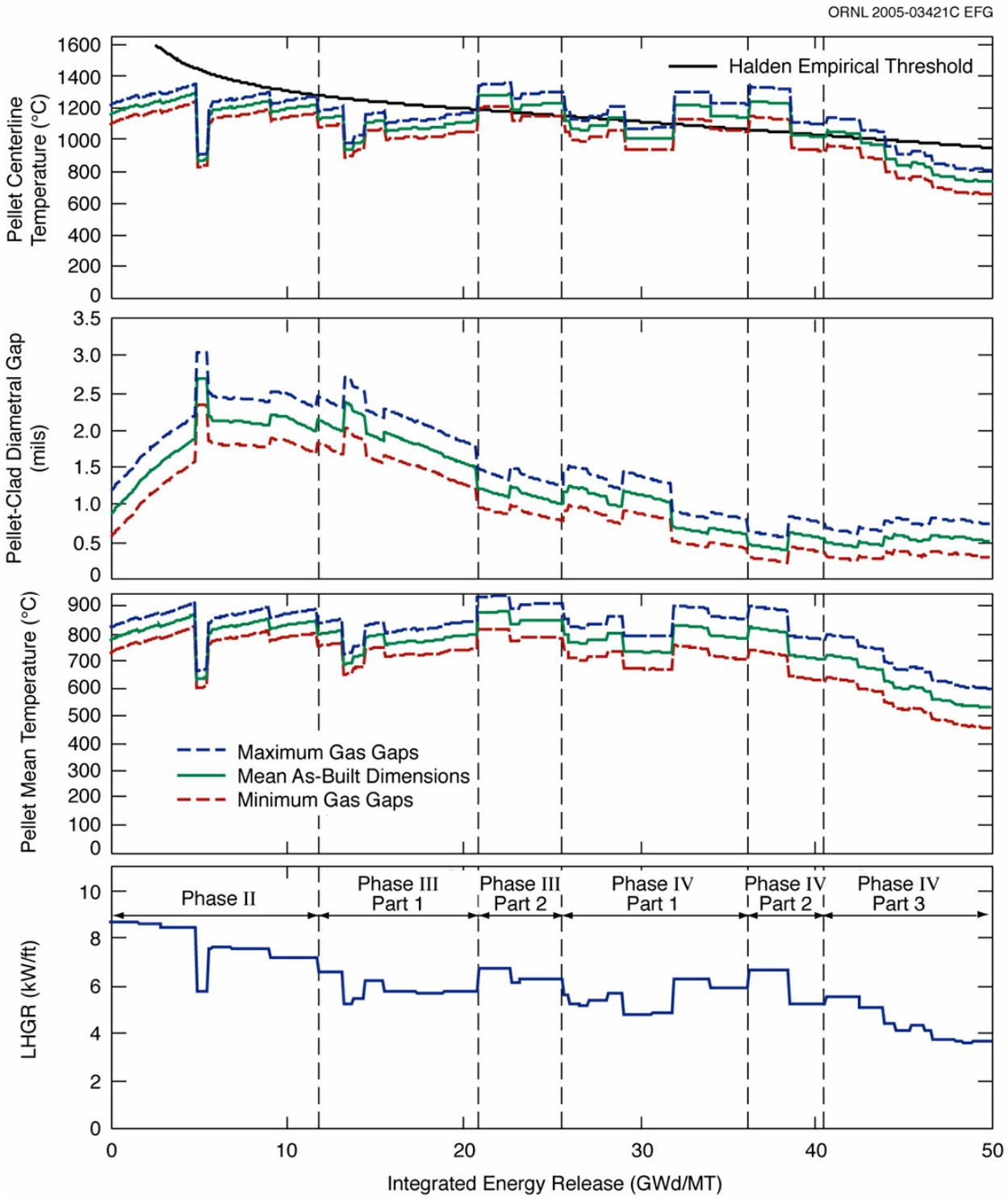

Fig. 8.5. CARTS post-PIE predictions for Capsule 12/Fuel Pin 15. Individual traces show results for maximum, mean, and minimum initial pellet-clad and clad-capsule gap widths.

As in the discussions for Capsule 6 (Section 8.3.1), for the pre-PIE calculations with a predicted fission gas release of 1.8%, the calculated fuel centerline temperature slightly exceeded the Halden empirical threshold only in cycles 126B (31.9–34.0 GWd/MT) and 127C (36.2–38.4 GWd/MT). However, for the post-PIE simulations, which employ the measured FGR of 8.61%, the fuel centerline temperatures exceed the Halden criteria (see Figure 8.5) for the majority of the irradiation for Phases III, Part 2; IV, Part 1; and IV, Part 2 (a period from 22.7 to 43.9 GWd/MT). Thus, it should be expected that the FGR would significantly exceed 1%. From a 15-GWd/MT burnup to the end of the irradiation, the post-PIE fuel centerline temperatures are 10–19% (90–160°C) higher than the pre-PIE calculated temperatures. The lower gap conductance due to the higher fission gas release increases the calculated fuel temperatures.

As with Capsule 6, the gap size for Capsule 12 (Figure 8.5) is nearly the same as the pre-PIE calculations. No contact between fuel pin and capsule is predicted at any time during the irradiation.

8.3.5 FRAPCON-3 and CARTS Predictions for Capsule 12/Fuel Pin 15

A comparison of the CARTS and FRAPCON-3 calculated fuel centerline temperatures for Capsule 12/ Fuel Pin 15 is given in Figure 8.6.

In Figure 8.6, the FRAPCON-3 and CARTS simulations employ mean initial capsule dimensions. As discussed in Section 8.3, the CARTS calculation is one-dimensional; the code uses the average LHGR for the 15-pellet stack and therefore does not recognize local variations in power due to axial peaking. The FRAPCON-3 model has 15 axial nodes (numbered from bottom to top) and does represent the axial power variation. Three FRAPCON-3 axial node centerline temperature plots are included in Figure 8.6: Pellet 7 (local LHGR less than average—Node 8), Pellet 1 [top pellet (next to gas plenum)—Node 15], and Pellet 15 [bottom pellet—Node 1].

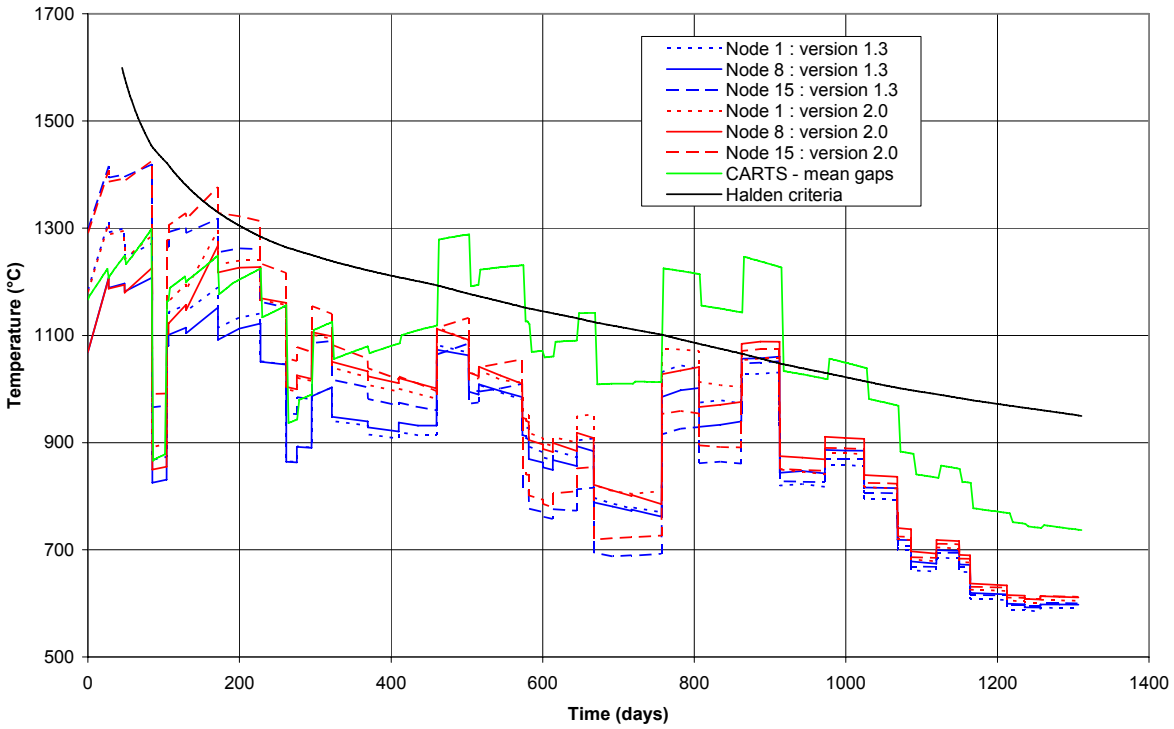

Fig. 8.6. Comparison of CARTS/FRAPCON-3 calculated centerline temperatures for Capsule 12/Fuel Pin 15.

Early in the irradiation, Capsule 12 was located in the lower portion of the test assembly, and hence local power was higher at the upper end of the pellet stack. The FRAPCON-3 simulations in Figure 8.6 clearly illustrate the effects of both capsule position relative to the ATR axial flux profile and the end-peaking in the fuel stack (top and bottom) through ~860 days (a burnup of approximately 36 GWd/MT); thereafter, the nodal temperature plots essentially converge as the burnup increases and end-peaking decreases.

There is good agreement between the CARTS and FRAPCON-3 results through a burnup of approximately 15 GWd/MT (~295 reactor-days). Subsequently, the FRAPCON-3 computed temperatures become increasingly lower than the CARTS predictions. The FRAPCON-3 temperatures are lower because first, CARTS accounts for cladding creep outward, and FRAPCON-3 does not; and, second, FRAPCON-3 employs a model for fuel cracking and segment relocation (essentially closing the pellet-to-clad gap), while CARTS does not.

Local temperature less than about 1000°C promotes the transformation of the fuel matrix to the high-burnup structure. For Capsule 12, the maximum fuel centerline temperature (1426°C, FRAPCON-3, Node 15) occurred at the end of the third cycle and remained below 1000°C for times greater than 914 days (average fuel burnups above 38.5 GWd/MT). Burnup within the agglomerates is much higher than the fuel average, and hence visible evidence of the onset of high-burnup structure formation is expected within the agglomerates in the fuel central region.

The performance of Capsule 6 has been simulated with FRAPCON-3 (version 1.3, modified at ORNL for MOX usage) and FRAPCON-3 (version 2.0, PNL released version applicable for LEU and MOX). There is very close agreement between the predicted fuel temperatures for these two versions through cycle 119A-1 (~104 days in Figure 8.6); thereafter, version 2.0 temperature predictions diverge from version 1.3's. PNL modified the fission gas release model for MOX fuels in version 2.0, and, as shown in Figure 8.7, the predicted FGR for version 2.0 closely matches the PIE data.

8.3.6 In-Reactor Conditions at the End of Phase IV, Part 3

Table 8.1 presents the results of the CARTS calculations for capsule conditions just prior to completion of the Phase IV, Part 3, irradiation and withdrawal of Capsules 6 and 12 for PIE. Fuel burnup at this time was about 50.0 GWd/MT. As indicated in the last column of Table 8.1, none of these calculations predicts clad contact at the pellet midplane any time during the irradiation. Pre-PIE CARTS calculated results are given in red for comparison purposes.

Although the calculated mean capsule wall temperature is virtually independent of assumptions with respect to the initial pellet-clad and clad-capsule gap widths, the calculated mean cladding temperature is higher for the pellets with maximum initial gaps. During reactor operation at the end of Phase IV, Part 3, the temperature (about 167–191°C) of the cladding surrounding these pellets is much higher than that (about 87–88°C) of the capsule wall, where temperature is controlled by forced convection to the coolant flow at the outer surface.

The post-PIE creep model [Equation (7.6)] predicts less cladding expansion than the pre-PIE formulation [Equation (7.5)] for the same cumulative cladding stress × exposure product; however, with the increased fission gas release in the post-PIE fuel pin simulations, the cumulative cladding stress × exposure product is higher (due to the higher fuel pin pressure), which leads to slightly higher cladding creep (which decreases the cladding-to-capsule gap). Also, the gap conductance decreases due to increased fission gas releases, which results in higher fuel temperatures and more fuel thermal expansion; even though there is slightly more cladding creep, the increased fuel expansion results in smaller pellet-to-cladding gaps.

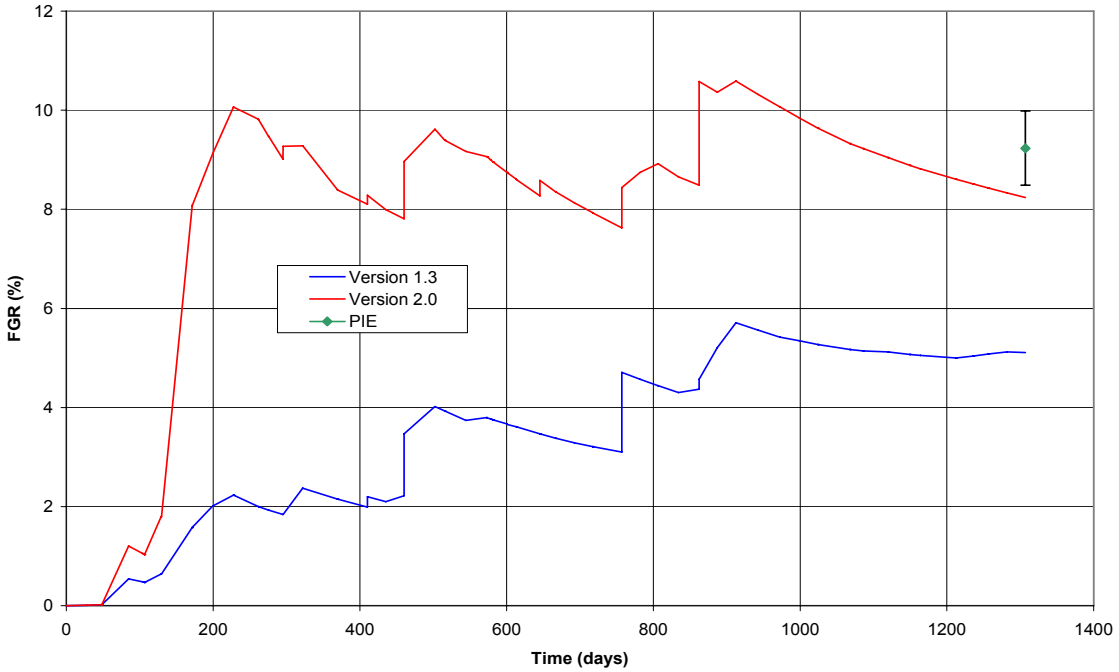

Fig. 8.7. Comparison of FRAPCON-3 calculated fission gas release for Capsule12/ Fuel Pin 15 with PIE data.

Table 8.1. Results of CARTS calculations for Capsules 6 and 12 just prior to the end of Phase IV, Part 3—pre-PIE CARTS results in red

Capsule	Initial pellet-clad clad-capsule gaps	Temperatures (°C)				Diametral gap (mil)		Pellet-clad contact during irradiation
		Pellet centerline	Pellet mean	Clad wall	Capsule wall	Pellet-to-clad	Clad-to-capsule	
6	Minimum	642 590	441 394	167 170	87.4 87.4	0.28 0.34	1.62 1.72	Never
	Maximum	788 680	578 477	187 189	87.3 87.3	0.75 1.00	2.39 2.48	Never
12	Minimum	656 596	453 398	168 171	87.7 87.7	0.27 0.32	1.57 1.71	Never
	Maximum	811 690	598 485	187 191	87.6 87.6	0.71 0.96	2.34 2.48	Never

In all cases, no cladding contact is predicted at the pellet midplane throughout the irradiation. Thus, locally imposed cladding strain is limited to that caused by thermal expansion (about 0.06%) and irradiation-induced outward creep (about 0.2%). Table 8.1 indicates calculated clad-to-capsule diametral gaps of between 1.57 and 2.39 mils at the end of the irradiation.

8.4 Predicted Conditions for the Capsules in the Hot Cell

The final burnup advancement steps in each CARTS calculation represent conditions from the time that the capsules arrived at ORNL (May 2004) through the time that the fuel pins were opened (October 2004, during the fuel pin gas pressure measurement). For these final calculation steps, the fuel pins are heated internally by decay power, while heat transfer from the outer capsule surface is by convection to the hot cell atmosphere.

Capsules 6 and 12 were introduced into the ORNL hot cell on May 17, 2004, about six weeks after completion of irradiation and their removal from the test assembly. The MOCUP protocol (coordinating calculations by MCNP and ORIGEN) was applied at INL to predict isotopic inventories and decay powers. During the period from mid-May to mid-October, these results show that the pellet stack decay power fell from 4.0 to 1.4 W (0.0080 to 0.0028 kW/ft). Fuel Pin 7 was opened on August 27 followed by Fuel Pin 16 on October 21.

The CARTS pre- (and post-) PIE predictions for the capsule conditions at the time of opening were based on a decay power of 1.4 W (0.0028 kW/ft), which corresponds to mid-October 2004. Heat transfer from the outer capsule surface is by free convection to the hot cell atmosphere. The natural convection heat transfer coefficient based on the capsule surface area directly over the pellet stack has been established as 27.5 W/m^2-°C (4.77 Btu/hr-ft^2-°F), based upon temperature measurements for the capsules examined in previous PIEs.

Table 8.2 presents the results of the CARTS calculations for conditions in the hot cell. Pre-PIE CARTS calculated results are given in red for comparison purposes.

Table 8.2. CARTS predictions for Capsules 6 and 12 under hot cell conditions—pre-PIE CARTS results in red

Capsule	Initial pellet-clad clad-capsule gaps	Temperatures (°C)				Diametral gap (mil)		Fuel pin internal pressure[a,b] (psia)
		Pellet centerline	Pellet mean	Clad wall	Capsule wall	Pellet-to-clad	Clad-to-capsule	
6	Minimum	40.1 39.8	40.0 39.7	39.5 39.5	39.4 39.4	1.40 1.30	1.54 1.63	151.3 61.8
	Maximum	40.4 39.9	40.3 39.8	39.5 39.5	39.4 39.4	2.30 2.21	2.33 2.43	145.6 59.7
12	Minimum	41.1 40.7	41.0 40.6	40.3 40.3	40.2 40.2	1.43 1.29	1.49 1.63	181.3 64.3
	Maximum	41.4 40.8	41.3 40.7	40.3 40.3	40.2 40.2	2.33 2.20	2.28 2.42	174.6 62.2

[a]Capsule 6/Fuel Pin 9, 148.4 psia (FPMA measurement)
[b]Capsule 12/Fuel Pin 15, 177.9 psia (FPMA measurement)

The fission gas release percentages employed in the post-PIE calculations for Capsule 6/Fuel Pin 9 and Capsule 12/Fuel Pin 15 are the PIE-measured 7.23% and 8.61%, respectively. The best estimate values considered for the pre-PIE analyses, based on the European experience and the average LHGRs during Phase II, were 1.6% for Capsule 6 and 1.8% for Capsule 12. Using "mean" initial gas gap dimensions, the fission gas release and helium release fraction was adjusted so that the post-PIE CARTS simulations would yield the same pressures [148.4 psia (Fuel Pin 9) and 177.9 psia (Fuel Pin 15)] as were measured via the FPMA. The final column of Table 8.2 indicates the predicted internal pressure within the fuel pins.

At the time of capsule opening, the pellet-to-clad diametral gaps within the fuel pins are predicted to lie between 1.40 and 2.33 mils, a range of 0.93 mil. This range is slightly higher than the pre-PIE predictions due to greater cladding creep. As noted in Section 8.3.6 with the increased fission gas release in the post-PIE fuel pin simulations, the cumulative cladding stress × exposure product is higher (due to the higher fuel pin pressure) which resulted in slightly higher cladding creep (which increases the pellet-to-cladding gap and decreases the cladding-to-capsule gap). Within this calculated range, the individual gap widths associated with the 15 different pellets are determined by the relative width of each pellet's initial cold diametral gap, which the design tolerances allow to lie between 2.0 and 3.5 mils.

The diametral gap between the outer surface of the Zircaloy cladding and the inner surface of the stainless steel capsule is predicted to lie in the range from 1.49 to 2.33 mils (less than pre-PIE predictions due to greater outward cladding creep). The as-built tolerances for the cold clad-to-capsule initial diametral gap vary between 2.2 and 3.0 mils.

8.5 Summary and Conclusions from the Code Simulations

The results of the pre- and post-PIE calculations for Capsules 6 and 12 are summarized in Tables 8.1 and 8.2. Table 8.1 provides a comparison of the two sets of CARTS predictions for the period just prior to the end of the Phase IV, Part 3 irradiation. Table 8.2 compares the predictions under hot cell conditions. In general, the predictions obtained in advance of the PIE are found to have been reasonably accurate, except for the fission gas release rates.

For Capsules 6 and 12 with burnups of 50.0 GWd/MT, the CARTS code predicts that the 15 pellets within each fuel pin will exhibit, under hot cell conditions, individual pellet-to-clad diametral gap widths ranging from 1.40 to 2.33 mils. (Where internal cracks are present, the diametral gap is defined to include the width of these open cracks.)

Cladding contact at the pellet midplane is not predicted to have occurred at any time during the irradiation. However, progressively increased cladding diameters have been observed in the previous PIEs. This outward movement of the cladding adjacent to the pellet midplane is believed due to irradiation-induced creep under the impetus of internal gas pressure. Since the fuel pin and capsule were initially filled with helium at atmospheric pressure, the differential pressure across the clad wall is initially very small, due only to the higher temperature of the gas in the fuel pin. However, the fuel pin internal pressure increases with burnup due to fission gas and helium release, and the wall hoop stress imposed by pressure differential is estimated to be 6–9 MPa as burnup increases to 50 GWd/MT.

With a total irradiation-induced outward creep strain of about 0.2 percent after 50 GWd/MT, the cladding outer diameter has increased. The diametral gap between the fuel pin and capsule is predicted to lie between 1.49 and 2.33 mils under hot cell conditions. This may be compared to the range of 2.2–3.0 mils for the initial cold capsule conditions.

These results with respect to gap widths expected under cold conditions suggest that fuel pin removal from the capsule and the subsequent fuel pin disassembly would be straightforward, without significant interference from either pin-to-capsule or pellet-to-clad binding—during the PIE, removal of the fuel pin was straightforward.

Temperatures were lower than 1000°C in the pellet central region during the latter quarter of the irradiation. Hence, the onset of high-burnup structure formation is expected to be visible within the agglomerates in this region.

Capsules 6 and 12 did exceed the Halden threshold for fission gas release during the test irradiation (for a significant period of time), and these fuel pellets have experienced 54 thermal cycles, about half again as many as would be expected for normal reactor operation to this burnup. Thus, the gas release may have been facilitated by a greater-than-normal extent of pellet thermal cracking. Based on FRAPCON-3 (version 1.3) pre-PIE predictions of higher fission gas releases of 5.34% and 5.84%, respectively, for Capsules 6 and 12, estimates for the total gas pressure within the fuel pins when opened in the hot cell are 124 psia for Capsule 6 and 131 psia for Capsule 12. The PIE FPMA measured fuel pin pressures for Capsules 6 and 12 were 148.4 and 177.9 psia, respectively. Version 2.0 of the FRAPCON-3 code very closely predicted the fission gas release from Fuel Pins 9 and 15.

9. POST-PIE CODE CALCULATIONS OF CAPSULE 5 IRRADIATION RESPONSE

9.1 Introduction

The CARTS and FRAPCON-3 calculations for Capsule 5 presented in Chapter 2 of the 50 GWd/MT Quick Look Report (Reference 53) were performed in advance of the PIE. Given the reassessment of the MOX fuel densification and swelling through a burnup of 50 GWd/MT presented in Section 6.4, the changes in the cladding creep model discussed in Section 7.4, and the final PIE fission gas release determination for Capsule 5 (Table 3.7), it is desirable to determine the extent to which these modeling changes (fuel densification, length of densification period, cladding creep during irradiation, fission gas release) affect the predicted behavior of Capsule 5. These post-PIE analyses are presented in this section, together with a comparison to the earlier predictions.

These CARTS and FRAPCON-3 calculations for Capsule 5 are based upon the actual burnup accumulations and corresponding average LHGRs experienced during ATR cycles 115C through 132C (Phases I–IV). This Capsule, which occupied just two test assembly positions during irradiation Phases I, II, III, and IV, was withdrawn at a burnup of 49.5 GWd/MT with an accumulated total of 1462 EFPDs.

Several aspects of the Capsule 5 irradiation history differ from those of the other MOX test capsules. Capsule 5, which carried untreated (non-TIGR) fuel, was irradiated as a single capsule, that is, not paired with a symmetrically-placed TIGR-treated counterpart. In addition, Capsule 5 is the only test capsule that participated in every irradiation phase and individual ATR cycle. It occupied a low flux test assembly position during most of its irradiation, and hence LHGRs and fuel temperatures were low compared to those of all other MOX test capsules. Because it was irradiated at a relatively low rate, Capsule 5 attained the highest accumulated EFPDs (1462) of any test capsule.

The CARTS calculations predict the conditions at the pellet midplane as a function of increasing burnup and do not include representation of pellet cracking and relocation, or pellet end-effects such as hourglassing.

FRAPCON-3 simulations require (1) the capsule irradiation history (same as CARTS) and (2) the time-dependent cladding surface temperatures predicted by CARTS as a boundary condition.

9.2 Differences in Pre- and Post-PIE Modeling Assumptions

The cold, unirradiated capsule and fuel pin dimensions employed in the Reference 53 analyses and in this chapter are based on the as-built component dimensional ranges given in Table 6.2.

The irradiation histories for Capsule 5 were provided in Sections 2.1 to 2.6 of Reference 53; the final version of the irradiation histories is given in Sections 3.1 to 3.6 of Volume 1 (Reference 36). There are no differences in these histories.

As noted in Chapters 6 and 7, cladding creep (outward) is occurring during the MOX test irradiation. For the pre-PIE analyses, the assumed creep-out of the cladding followed the empirical model given by Equation 7.5 (based on the irradiation data through the 40-GWd/MT PIEs). The post-PIE calculations employ the empirical fit (Equation 7.6) to all the MOX test data through the 50-GWd/MT PIEs.

As shown in Figure 7.4, the post-PIE creep model (Equation 7.6) predicts less cladding expansion than the pre-PIE formulation (Equation 7.5); thus, there is potential for the width of the predicted pellet-to-clad gas gaps to decrease, with a concomitant decrease in fuel temperatures due to higher gap conductances.

CARTS modeling of fuel densification requires user-input of the degree of densification and the length of the densification period. The pre-PIE parameters are based on the assessment given in Section 5.4 of Reference 40, while the post-PIE parameters are based on the re-assessment given in Section 6.4 of this report. It develops that these densification parameters are the same for both the pre- and post-PIE CARTS calculations, as follows:

- FRAPCON-based models: a maximum of 2% fuel densification achieved during the period of 0–10 GWd/MT burnup.

The cumulative fission gas release affects the gap conductance throughout the CARTS calculation and is controlled via a code input parameter specifying the percent released at 45 GWd/MT. The best estimate value considered for the pre-PIE analyses, based on the European experience and the average LHGRs during Phase II, was 0.8% for Capsule 5. Per the CARTS algorithm, this corresponds to a release at 50 GWd/MT of 1.0%.

The fission gas release percentages employed in the post-PIE calculations for Capsule 5 correspond to the PIE-measured 3.1%. These fission gas releases are higher than used in the pre-PIE calculations; thus, the pellet-cladding gap conductance will be lower, resulting in higher fuel temperatures.

Other than these noted differences, all CARTS and FRAPCON-3 code inputs and models for the pre- and post-PIE calculations are the same.

9.3 Post-PIE Results for Capsule Conditions During the Irradiation

In addition to the CARTS simulations, the ORNL version of FRAPCON-3 (version 1.3, modified at ORNL for MOX usage) and the official PNL released version of FRAPCON-3 for MOX (version 2.0) were executed for Capsule 5.

The CARTS simulations are one-dimensional; the code uses the average LHGR for the 15-pellet stack and therefore does not recognize local variations in power due to axial flux peaking. The FRAPCON-3 model contains 15 axial segments or nodes (one per fuel pellet) and uses the axial power peaking factors (as a function of burnup) calculated by G. Chang at INL (Reference 46). Since the local axial power in the fuel is determined via the mean LHGR and the axially-dependent (and burnup-dependent) peaking factors, the burnup of each individual pellet is different; the calculated and measured axial-burnups given in the PIE Observations Report for Capsule 5 (Reference 36) and shown in Figure 9.1 are in good agreement.

There are two notable differences between CARTS and FRAPCON-3 fuel pin modeling: first, FRAPCON-3 does not predict cladding creep-out, while CARTS has specific models for creep-out (based on PIE results); secondly, FRAPCON-3 has models for fuel cracking and relocation, whereas CARTS does not. Both of these code-modeling differences affect the calculated fuel temperatures. It is concluded in Chapter 5 of Reference 40 that the CARTS/FRAPCON-3 predictions provide, respectively, upper and lower bounds for the actual fuel temperature history for these MOX test irradiations.

Also, it should be noted that CARTS specifically accounts for the helium created within and released from the MOX fuel. Although both codes account for the helium charged when the fuel pin is sealed, FRAPCON-3 has no models for helium generation or release.

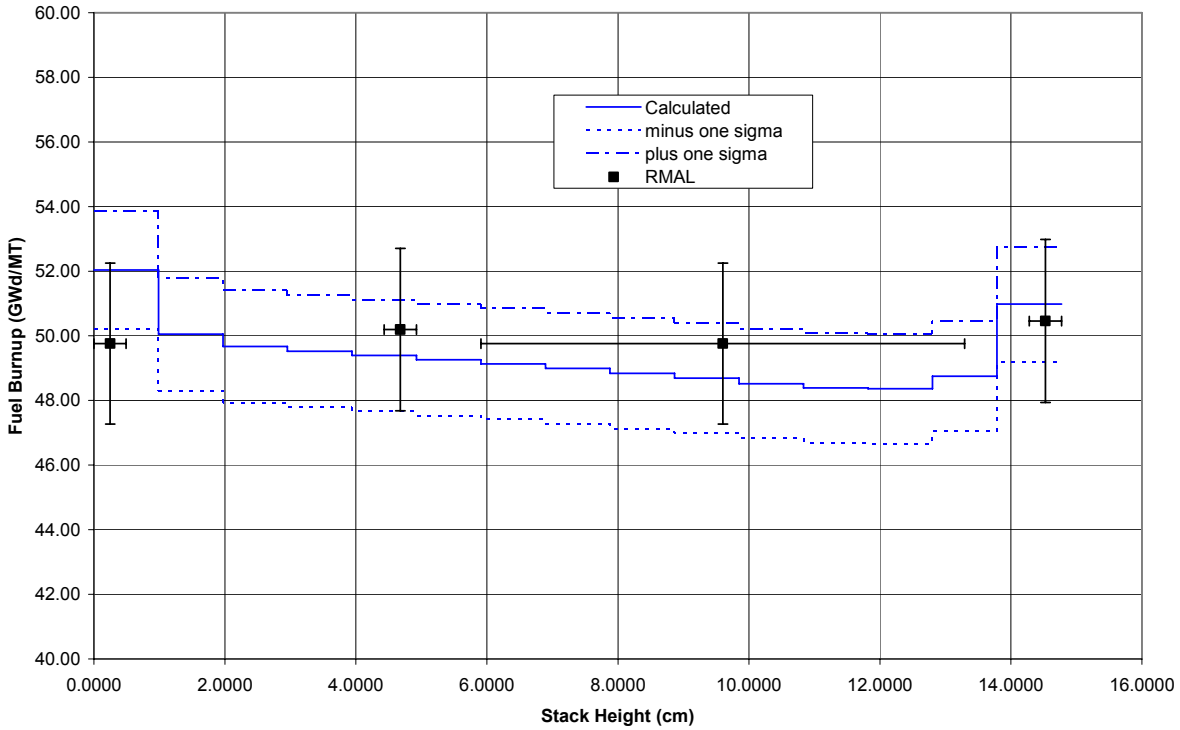

Fig. 9.1. FRAPCON-3 axial burnup predictions for Capsule 5/Fuel Pin 8.

CARTS was originally developed at ORNL for the MOX test irradiations in the ATR because no available fuels-modeling code (including FRAPCON-3) is applicable for the fuel pin/capsule double-containment configuration utilized in this test irradiation. However, given the time-dependent cladding thermal boundary condition (calculated by CARTS), FRAPCON-3 can simulate these fuel pin irradiation histories. (This assumption of a single temperature over the 6-in. cladding length is acceptable in view of the very small actual axial variation.)

As noted above, each capsule surrounds a fuel pin containing 15 MOX pellets. Each pellet has unique dimensions within the specified fabrication tolerances, so that a spectrum of initial pellet-to-clad gaps exists within each fuel pin. In the following discussions, CARTS results are reported for the minimum, mean, and maximum initial gap widths as defined by the measured fuel pin inner diameter and the tolerance range for initial pellet outer diameter.

Before proceeding to the conditions predicted for the capsule components in the hot cell, it is of interest to first consider the variations in pellet temperatures and diametral gaps as calculated for the period of irradiation, with particular attention to the conditions at the end of Phase IV, Part 3, just prior to removal of the 50-GWd/MT capsules for PIE.

Pre-PIE calculated results are italicized in parenthesis for comparison purposes.

9.3.1 CARTS Results for Capsule 5

Figure 9.2 illustrates the cycle-by-cycle LHGRs as calculated by the MCNP code for Capsule 5, with the corresponding CARTS predictions of pellet mean and centerline temperatures and variations in pellet-clad diametral gap. These parameters are plotted against the integrated internal energy release per unit heavy metal mass. The integrated energy release within the fuel includes power contributions other than fission (such as gamma heating by the ATR core) and thereby differs slightly from fuel burnup. In the interest of

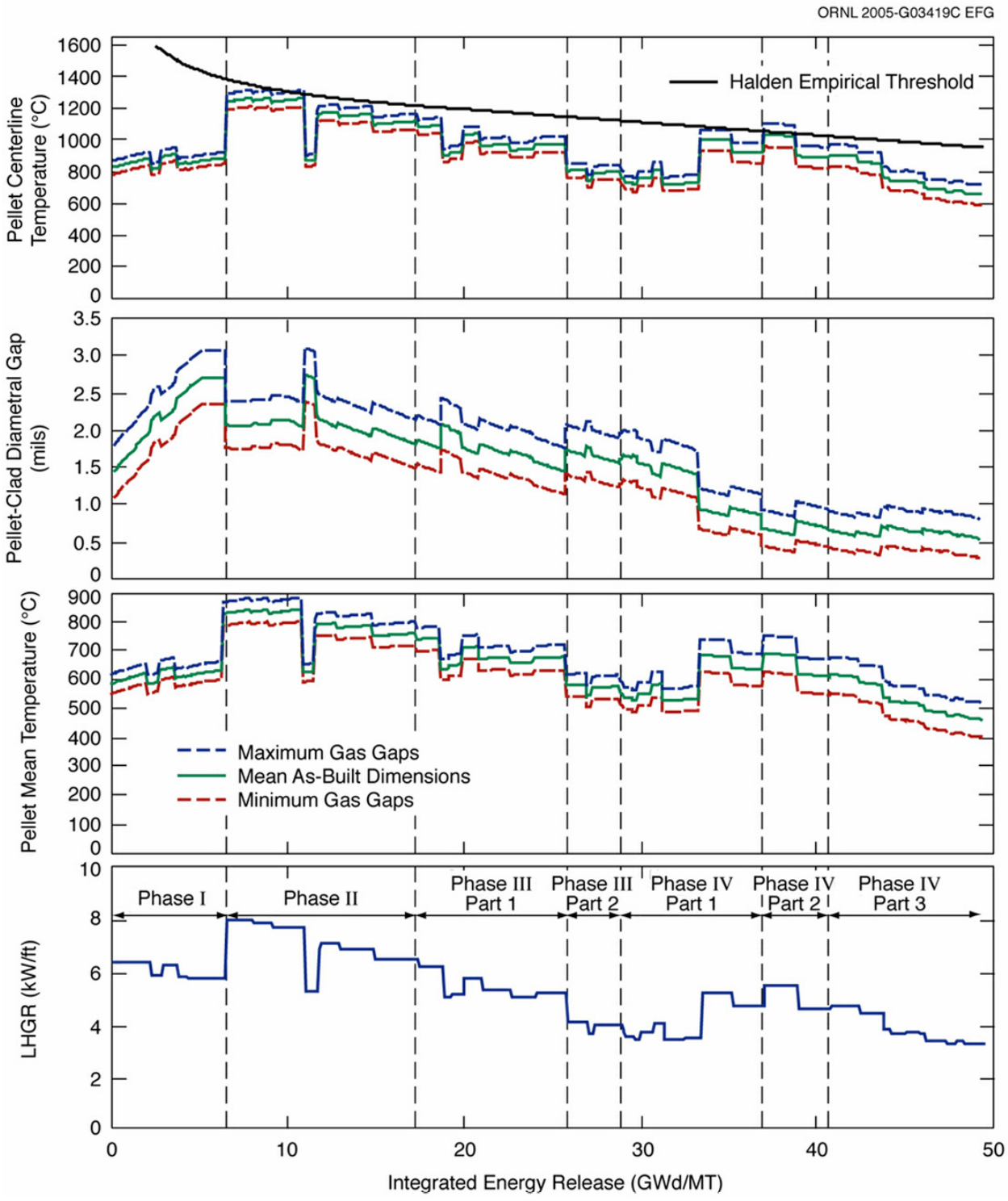

Fig. 9.2. CARTS post-PIE predictions for Capsule 5/Fuel Pin 8. Individual traces show results for maximum, mean, and minimum initial pellet-clad and clad-capsule gap widths.

avoiding unnecessary clutter, the LHGR trace does not include spikes to near zero to mark the between-cycle reactor outages.

Three traces are shown in each of the temperature and diametral gap plots, illustrating results as calculated for minimum, mean, and maximum initial pellet-to-clad gap widths. As indicated, the diametral gap is predicted to have remained open throughout the irradiation, with a closest approach to closure (for the case of minimum initial gap) of about 0.29 (*0.446*) mil near the end of cycle 132C (near the end of Phase IV, Part 3).

Unless otherwise stated, the following discussion will reflect the mean-value traces as shown in Figure 9.2. The ranges between the minimum and maximum traces on the temperature and diametral gap plots indicate the variations associated with pellet-specific differences in the initial pellet-clad gap width. With pellet densification of 2.0% completed before burnup reaches 10.0 GWd/MT, the pellet diameter initially decreases and remains smaller than its initial value throughout Phase I. This pellet shrinkage causes the predicted pellet-clad diametral gap to almost double (from 1.45 to 2.70 [*2.73*] mils) during this period.

The highest LHGR experienced by Capsule 5 (7.99 kW/ft) was imposed at the beginning of Phase II. As indicated in Figure 9.2, the accompanying increase in pellet thermal expansion causes the pellet-clad gap to narrow to 2.07 [*2.10*] mils. Reduced LHGRs during the subsequent cycles lower the pellet temperature with corresponding reductions in thermal expansion that tend to increase the pellet-clad gap (through a burnup of 10 GWd/MT). Subsequently, with fuel densification complete, this trend is countered by monotonically increasing fuel swelling as burnup accumulates. The gap width tends to decrease with increasing burnup, but remains greater than its initial value until near the middle of Phase IV, Part 1 (integrated energy release of 33.4 GWd/MT).

The increased LHGRs during the last two cycles of Phase IV, Part 1 (and all of Parts 2 and 3) are due to the shift of the test assembly to the Southwest I-hole. The higher thermal expansion of the fuel (due to the increased LHGRs) during these cycles reduces the gap width to its smallest values during the irradiation.

The predicted temperatures are consistently higher for the calculation based on maximum initial pellet–clad gaps. This follows from the lower effective thermal conductance associated with wider gaps. Figure 9.2 shows that the highest predicted pellet centerline temperature (1263 [*1245*]°C) occurs at the end of the first irradiation cycle of Phase II (7.8 GWd/MT). Because this is more than 1000°C below the melting temperature of the MOX fuel, there is no concern for the possibility of fuel melting.

In the pre-PIE calculations with a predicted fission gas release of 1.0%, the calculated fuel centerline temperature approached but did not exceed the Halden empirical threshold (for FGR releases greater than 1%). However, for the post-PIE simulations, which employ the measured FGR of 3.1%, the fuel centerline temperatures exceed the Halden threshold (see Figure 9.2) in cycle 118B (Phase II), in cycle 126B (Phase IV, Part 1) and in cycle 127C (Phase IV, Part 2). Thus, it should be expected that the FGR would significantly exceed 1%.

From 22.6-GWd/MT burnup to the end of the irradiation, the post-PIE fuel centerline temperatures are 9–15% (70–100°C) higher than the pre-PIE calculated temperatures. The lower gap conductance due to the higher fission gas release increases the calculated fuel temperatures.

The gap size (Figure 9.2) is nearly the same as the pre-PIE calculations.

No contact between fuel pin and capsule is predicted at any time during the irradiation.

9.3.2 FRAPCON-3 Results for Capsule 5 with Comparisons to CARTS Predictions

A comparison of the CARTS (mean gap) and FRAPCON-3 (versions 1.3 and 2.0) post-PIE calculated fuel centerline temperatures for Capsule 5/Fuel Pin 8 is given in Figure 9.3.

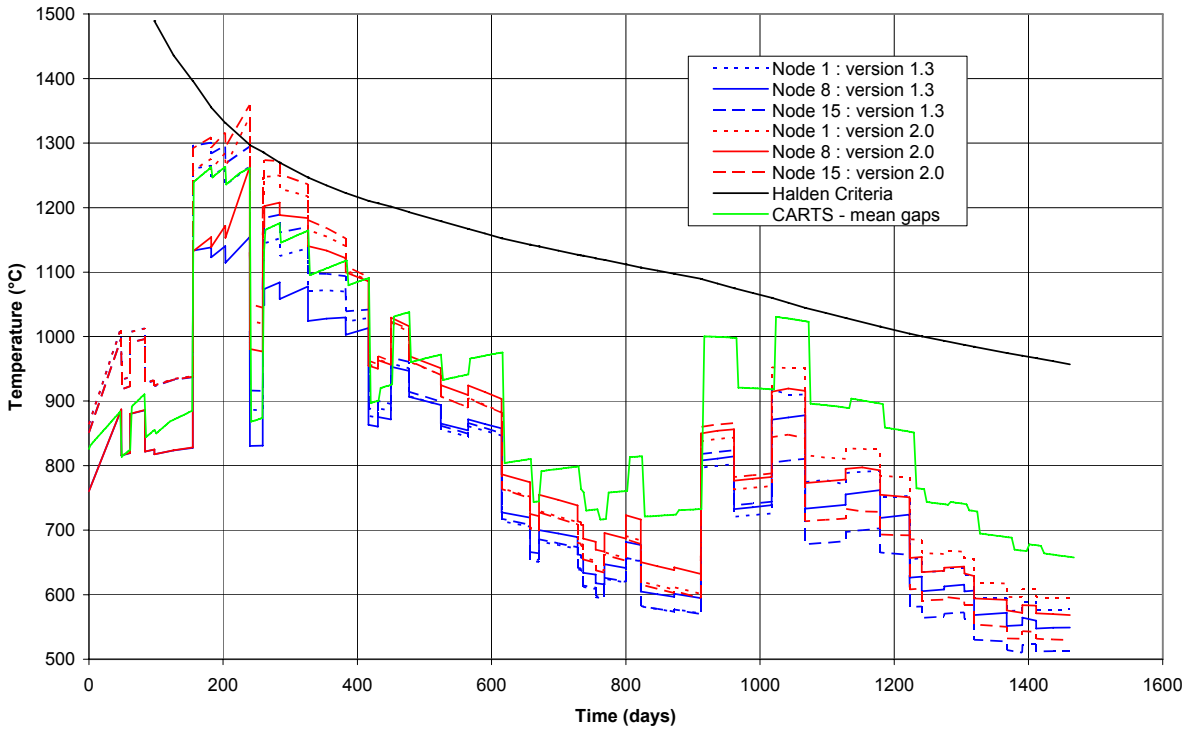

Fig. 9.3. Comparison of CARTS/FRAPCON-3 calculated centerline temperatures for Capsule 5/Fuel Pin 8.

In Figure 9.3, the FRAPCON-3 and CARTS simulations employ mean initial capsule dimensions. As discussed in Section 9.3, the CARTS calculation is one-dimensional; the code uses the average LHGR for the 15-pellet stack and therefore does not recognize local variations in power due to axial peaking. The FRAPCON-3 model has 15 axial nodes (numbered from bottom to top) and does represent the axial power variation. Three FRAPCON-3 axial node centerline temperature plots are included in Figure 9.3: Pellet 7 (local LHGR less than average—Node 8), Pellet 1 [top pellet (next to gas plenum)—Node 15], and Pellet 15 (bottom pellet—Node 1).

The FRAPCON-3 simulations in Figure 9.3 clearly illustrate the end-peaking in the fuel stack (top and bottom).

There is good agreement between the CARTS and FRAPCON-3 results through approximately 450 reactor-days (~20 GWd/MT burnup). Subsequently, the FRAPCON-3 computed temperatures become increasingly lower than the CARTS predictions. The lower FRAPCON-3 temperatures are caused by two factors, both contributing to a higher calculated gap thermal conductance: first, CARTS accounts for cladding creep outward, and FRAPCON-3 does not; and, secondly, FRAPCON-3 employs a model for fuel cracking and segment relocation (essentially closing the pellet-to-clad gap), while CARTS does not.

Local temperature less than about 1000°C promotes the transformation of the fuel matrix to the high-burnup structure. For Capsule 5, the maximum fuel centerline temperature (1360°C, FRAPCON-3,

Node 15) occurred at the end of cycle 118B (Phase II, 240 EFPDs [~10.8-GWd/MT burnup]) and the centerline remained below 1000°C for times greater than 1068 reactor-days (average fuel burnups above 38.8 GWd/MT). Burnup within the agglomerates is much higher than the fuel average, and hence the onset of high-burnup structure formation is expected to be visible within the agglomerates in the fuel central region.

The performance of Capsule 5 has been simulated with FRAPCON-3 (version 1.3, modified at ORNL for MOX usage) and FRAPCON-3 (version 2.0, PNL released version applicable for LEU and MOX). There is very close agreement between the predicted fuel temperatures for these two versions through Phase I [cycle 117B (~155 days in Figure 9.3)]; thereafter, version 2.0 temperature predictions diverge from version 1.3's. PNL modified the fission gas release model for MOX fuels in version 2.0 and, as shown in Figure 9.4, the measured FGR falls between the predicted results for versions 1.3 and 2.0. Version 2.0's FGR prediction is significantly higher than the version 1.3 simulation results after ~155 days; hence, the gap conductance is lower, due to the increased fission gas release, and the resulting fuel temperatures are higher for the version 2.0 predictions. Comparing Figures 9.3 and 9.4, the fission gas release "bursts" occur when the fuel temperature approaches (or exceeds) the Halden threshold.

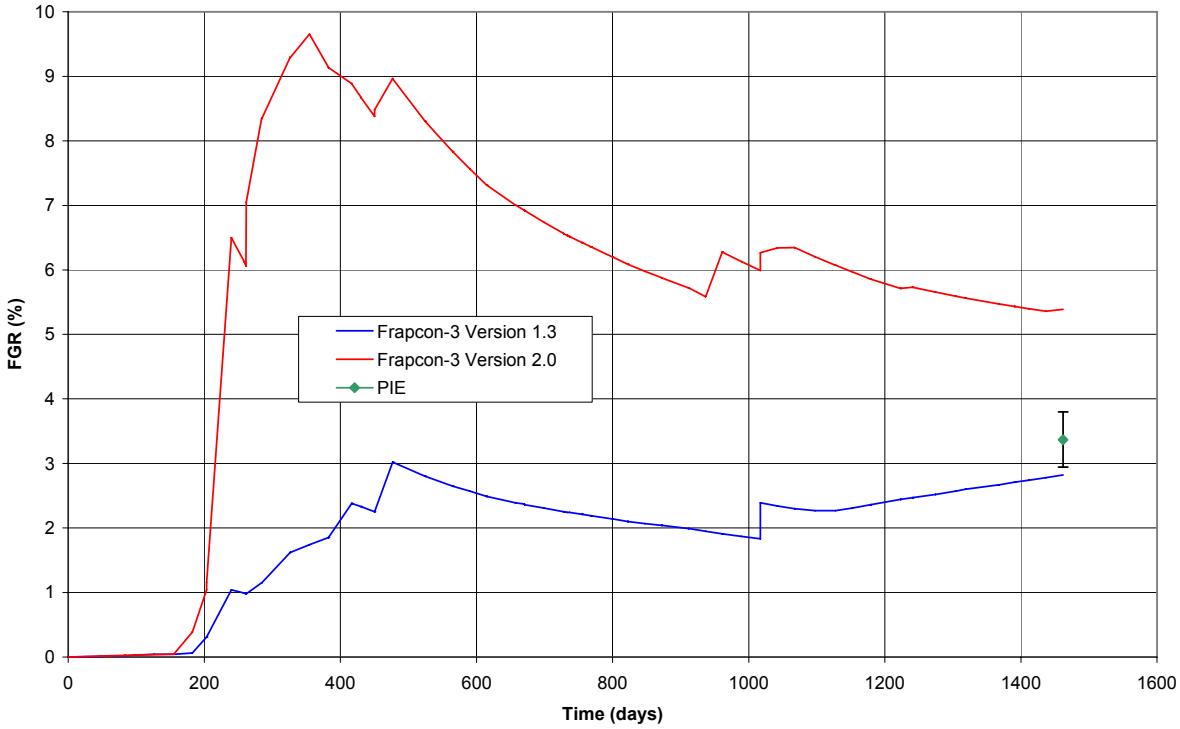

Fig. 9.4. Comparison of FRAPCON-3 calculated fission gas release for Capsule 5/ Fuel Pin 8 with PIE data.

9.3.3 In-Reactor Conditions at the End of Phase IV, Part 3

Table 9.1 presents the results of the CARTS calculations for capsule conditions just prior to completion of the Phase IV, Part 3 irradiation and withdrawal of Capsule 5 for PIE. Fuel burnup at this time was about 49.5 GWd/MT. As indicated in the last column of Table 9.1, none of these calculations predicts clad contact at the pellet midplane any time during the irradiation. Pre-PIE CARTS calculated results are given in red for comparison purposes.

Table 9.1. Results of CARTS calculations for Capsule 5 just prior to the end of Phase IV, Part 3—pre-PIE CARTS results in red

Capsule	Initial pellet-clad clad-capsule gaps	Temperatures (°C)				Diametral gap (mil)		Pellet-clad contact during irradiation
		Pellet centerline	Pellet mean	Clad wall	Capsule wall	Pellet-to-clad	Clad-to-capsule	
5	Minimum	590 549	407 370	164.5 164	86.0 86.0	0.29 0.42	1.77 1.76	Never
	Maximum	720 622	528 437	182.5 182	86.0 86.0	0.81 1.13	2.54 2.53	Never

Although the calculated mean capsule wall temperature is virtually independent of assumptions with respect to the initial pellet-clad and clad-capsule gap widths, the calculated mean cladding temperature is higher for the pellets with maximum initial gaps. During reactor operation at the end of Phase IV, Part 3, the temperature (about 164–182°C) of the cladding surrounding these pellets is much higher than that (about 86°C) of the capsule wall, where temperature is controlled by forced convection to the coolant flow at the outer surface.

The post-PIE creep model [Equation (7.6)] predicts less cladding expansion than the pre-PIE formulation [Equation (7.5)] for the same cumulative cladding stress × exposure product; however, with the increased fission gas release in the post-PIE fuel pin simulations, the cumulative cladding stress × exposure product is higher (due to the higher fuel pin pressure), which leads to slightly higher cladding creep (which decreases the cladding-to-capsule gap). Also, the gap conductance decreases due to increased fission gas releases, which results in higher fuel temperatures and more fuel thermal expansion; even though there is slightly more cladding creep, the increased fuel expansion results in smaller pellet-to-cladding gaps.

In all cases, no cladding contact is predicted at the pellet midplane throughout the irradiation. Thus, locally imposed cladding strain is limited to that caused by thermal expansion (about 0.07%) and irradiation-induced outward creep (about 0.2%). Table 9.1 indicates calculated clad-to-capsule diametral gaps of between 1.76 and 2.54 mils at the end of the irradiation.

9.4 Predicted Conditions for the Capsules in the Hot Cell

The final burnup advancement steps in each CARTS calculation represent conditions from the time that the capsule arrived at ORNL (May 2004) through the time that the fuel pin was opened (mid-November 2004, during the fuel pin gas pressure measurement). For these final calculation steps, the fuel pin is heated internally by decay power, while heat transfer from the outer capsule surface is by convection to the hot cell atmosphere.

Capsule 5 was introduced into the ORNL hot cell on May 17, 2004, about 6 weeks after completion of irradiation and its removal from the test assembly. The MOCUP protocol (coordinating calculations by MCNP and ORIGEN) was applied at INL to predict isotopic inventories and decay powers. During the period from mid-May to mid-November, these results show that the pellet stack decay power fell from 2.8 to 1.2 W (0.0056 to 0.0024 kW/ft). Fuel Pin 8 was opened on November 11.

The CARTS pre- (and post-) PIE predictions for the capsule conditions at the time of opening were based on a decay power of 1.2 W (0.0024 kW/ft), which corresponds to mid-November 2004. Heat transfer from the outer capsule surface is by free convection to the hot cell atmosphere. The natural convection heat transfer coefficient based on the capsule surface area directly over the pellet stack has been established as 27.5 W/m^2-°C (4.77 Btu/hr-ft^2-°F), based upon temperature measurements for the capsules examined in previous PIEs.

Table 9.2 presents the results of the CARTS calculations for conditions in the hot cell. Pre-PIE CARTS calculated results are given in red for comparison purposes.

Table 9.2. CARTS predictions for Capsule 5 under hot cell conditions—pre-PIE CARTS results in red

Capsule	Initial pellet-clad clad-capsule gaps	Temperatures (°C)				Diametral gap (mil)		Fuel pin internal pressure[a] (psia)
		Pellet centerline	Pellet mean	Clad wall	Capsule wall	Pellet-to-clad	Clad-to-capsule	
5	Minimum	39.3 39.1	39.2 39.0	38.8 38.8	38.7 38.7	1.30 1.31	1.68 1.67	71.5 50.2
	Maximum	39.5 39.1	39.4 39.0	38.8 38.8	38.7 38.7	2.20 2.22	2.48 2.46	69.1 48.7

[a]Capsule 5/Fuel Pin 8, 70.3 psia (FPMA measurement).

The fission gas release percentage employed in the post-PIE calculations for Capsule 5/Fuel Pin 8 is the PIE-measured 3.1%. The best estimate value considered for the pre-PIE analyses, based on the European experience and the average LHGRs during Phase II, was 1.0%. Using "mean" initial gas gap dimensions, the fission gas release and helium release fraction was adjusted so that the post-PIE CARTS simulation would yield the same pressure (70.3 psia) as was measured via the FPMA The final column of Table 9.2 indicates the predicted internal pressure within the fuel pins.

At the time of capsule opening, the pellet-to-clad diametral gaps within the fuel pins are predicted to lie between 1.30 and 2.22 mils, a range of 0.92 mil. This range is slightly higher than the pre-PIE predictions due to greater cladding creep. As noted in Section 9.3.3 with the increased fission gas release in the post-PIE fuel pin simulation, the cumulative cladding stress × exposure product is higher (due to the higher fuel pin pressure), which resulted in slightly higher cladding creep (which increases the pellet-to-cladding gap and decreases the cladding-to-capsule gap). Within this calculated range, the individual gap widths associated with the 15 different pellets are determined by the relative width of each pellet's initial cold diametral gap, which the design tolerances allow to lie between 2.0 and 3.5 mils.

The diametral gap between the outer surface of the Zircaloy cladding and the inner surface of the stainless steel capsule is predicted to lie in the range from 1.67 to 2.48 mils (less than pre-PIE predictions due to greater outward cladding creep). The as-built tolerances for the cold clad-to-capsule initial diametral gap vary between 2.2 and 3.0 mils.

9.5 Summary and Conclusions from the Code Simulations

The results of the pre- and post-PIE calculations for Capsule 5 are summarized in Tables 9.1 and 9.2. Table 9.1 provides a comparison of the two sets of CARTS predictions for the period just prior to the end of the Phase IV, Part 3 irradiation. Table 9.2 compares the predictions under hot cell conditions. In general, the predictions obtained in advance of the PIE are found to have been reasonably accurate, except for the fission gas release.

For Capsule 5 with a burnup of 49.5 GWd/MT, the CARTS code predicts that the 15 pellets within each fuel pin will exhibit, under hot cell conditions, individual pellet-to-clad diametral gap widths ranging from 1.30 to 2.22 mils. (Where internal cracks are present, the diametral gap is defined to include the width of these open cracks.)

Cladding contact at the pellet midplane is not predicted to have occurred at any time during the irradiation. However, progressively increased cladding diameters have been observed in the previous PIEs. This outward movement of the cladding adjacent to the pellet midplane is believed due to

irradiation-induced creep under the impetus of internal gas pressure. Because the fuel pin and capsule were initially filled with helium at atmospheric pressure, the differential pressure across the clad wall is initially very small, due only to the higher temperature of the gas in the fuel pin. However, the fuel pin internal pressure increases with burnup due to fission gas and helium release, and the wall hoop stress imposed by pressure differential is estimated to be ~2.6 MPa as burnup increases to 49.5 GWd/MT.

With an irradiation-induced outward creep of about 0.2%, the cladding outer diameter has increased. The diametral gap between the fuel pin and capsule is predicted to lie between 1.67 and 2.48 mils under hot cell conditions. This may be compared to the range of 2.2–3.0 mils for the initial cold capsule conditions.

These results with respect to gap widths expected under cold conditions suggest that fuel pin removal from the capsule and the subsequent fuel pin disassembly would be straightforward, which was the PIE experience.

Temperatures were lower than 1000°C in the pellet central region during the latter quarter of the irradiation. Hence, the onset of high-burnup structure formation is expected to be visible within the agglomerates in this region.

Capsule 5 did briefly exceed the Halden threshold for fission gas release during the test irradiation, and these fuel pellets have experienced 62 thermal cycles, about half again as many as would be expected for normal reactor operation to this burnup. Thus, the gas release may have been facilitated by a greater-than-normal extent of pellet thermal cracking.

The PIE FPMA measured fuel pin pressure for Capsule 5 was 70.3 psia. Post-PIE simulations of the FRAPCON-3 code (versions 1.3 and 2.0) predicted, respectively, 61 and 102 psia pressure in the fuel pin.

10. CONCLUSIONS

1. Mixed-oxide (MOX) fuel prepared with plutonium derived from weapons components has been irradiated to 50 GWd/MT under conditions more severe than will be encountered by Mission Fuel. Gallium is present within the test fuel at 1–5 ppm, much more than will be present in Mission Fuel, and is present in the unirradiated cladding at approximately 0.5 ppm.

   - Comparisons of the measured gallium concentrations in the irradiated cladding with those of the unirradiated material indicate no significant change.

   - Gallium measurements during the successive PIEs for the irradiated pellets of both fuel types (untreated and TIGR) indicate pellet-to-pellet variations (expected) but no reduction in the overall fuel gallium content.

   - It is concluded that any migration of gallium from fuel to cladding is insignificant and presents no credible threat to the cladding integrity.

2. The fuel examined in the current PIE experienced (during Phase II of the irradiation) LHGRs less than 9 kW/ft. Capsule 5/Fuel Pin 8 is the only test capsule that participated in every irradiation phase and individual ATR cycle. It occupied a low flux test assembly position during most of its irradiation, and hence LHGRs and fuel temperatures were low compared to those of all other MOX test capsules. Because it was irradiated at a relatively low rate, Capsule 5 attained the highest accumulated EFPDs (1462) of any test capsule.

3. The release of fission gas to the fuel pin free volume is largely controlled by diffusion of the gas atoms, whose mobility (diffusivity) increases exponentially with temperature. Thus, fission gas release fraction is largely determined by the maximum temperature experienced by the fuel. The centerline temperatures of the current test fuels exceeded the Halden Threshold during irradiation, and hence fission gas release in excess of 1% is to be expected. The actual fission gas release (for all the irradiated capsules—through fuel burnups of 50 GWd/MT) is comparable with the European experience for MOX fuel.

4. The MOX test fuel was fabricated with a MIMAS-type process involving use of a master-mix produced by milling together all of the PuO_2 with a greater mass of UO_2. (This consumes only a small fraction of the total UO_2.) The milling produces an intimate mixing, but also modifies the powder physical characteristics (surface area, density, flowability), while electrostatic forces induce self-agglomeration. After milling, the master-mix was diluted (mixed) into the remainder of the UO_2 to form the secondary blend, from which the pellets were pressed. This secondary blending was less effective than intended in dispersing the master-mix into the UO_2 matrix. Consequently, a few relatively large residual agglomerates (clumps of master-mix) are evident in the irradiated fuel.

5. At 50-GWd/MT average fuel burnup, local burnups are about 110 GWd/MT within the agglomerates and only about 38 GWd/MT in the surrounding UO_2 matrix. Corresponding fuel lattice swelling (at 0.7% per 10 GWd/MT) is ~3.5% overall.

6. Literature values for modern European commercial fuels indicate postirradiation agglomerate maximum equivalent diameters in the 250- to 400-micron range for fuel average burnups in the vicinity of 45 GWd/MT. The current PIE results (and the measured preirradiation sizes) indicate that this test fuel began irradiation with a greater fraction of large agglomerates than is normally encountered in modern MOX fuels. Nevertheless, the subsequent swelling during irradiation has been

in the proportions expected for the current burnup, and there have been no performance problems with the fuel. In particular, the fission gas release has been no greater than that expected from the European experience.

7. The halos surrounding each of the agglomerates are clear regions distinct from both the fuel matrix and the high-burnup structure. These regions are visible because athermal (fission recoil) diffusion of fission products from the agglomerate has altered the adjacent matrix in a manner that responds differently to polishing. Agglomerates of widely varying sizes display the halo, which comprises very small (nanometer-size) gas bubbles within the adjoining low-burnup UO_2 matrix grains. The presence of xenon in these regions has been confirmed by EPMA measurements.

8. The high-burnup structure transformations for agglomerates in the central pellet region are evident from the metallographic mounts for the current PIE. Transformation requires locally high burnups at temperatures less than 1000°C. Temperatures this low in this region for Fuel Pins 8, 9, and 15 occurred in the last phases of the test irradiation.

9. The flux spectrum experienced by the MOX test fuel in the ATR reflector was softer than that encountered by fuel in a commercial PWR. The softer spectrum served to increase the effective fission cross section by a factor of about 4, meaning that fuel irradiated in the ATR reflector could sustain the same linear power with about one-fourth the thermal flux that would be necessary in a commercial PWR. The ^{238}U capture cross section is, however, only slightly increased in the softer spectrum. With one-fourth the thermal flux, the buildup of ^{239}Pu at the pellet rim is much slower in the ATR reflector than for fuel at the same axial power level in a commercial PWR. With less local buildup of fissile material, the rim burnup will be closer to the UO_2 matrix average. This explains the absence of high-burnup structure around the pellet rims in the MOX test fuel.

10. The fuel behavior (Chapter 6, i.e., cracking, densification, and swelling) of the MOX test fuel is normal and prototypic of commercial fuel.

11. As stated in Reference 13, “When stress is applied to a metal, it creeps, even if this creep rate is very slow. When this occurs under neutron flux, a much greater strain rate is observed at temperatures where thermal creep is not even measurable.” The test fuel pin cladding diameter has expanded by about 0.8–0.9 mil at 50 GWd/MT. This irradiation-induced outward creep occurred under the impetus of a tensile wall (hoop) stress that increased from zero to a little more than nine MPa as fuel pin internal pressure increased during the irradiation. Although information on outward cladding creep is limited (most interest lies in creep down), some data are found as discussed in Chapter 7. As shown in Figure 7.3, the creep observed in the current test irradiation is compatible with the experience documented in the available literature.

12. ABAQUS code finite-element calculations performed for the zero-burnup initial heatup with as-built dimensions for the pellet, fuel pin, and capsule, and with the actual initial LHGR are documented for the 30-GWd/MT withdrawal in Chapter 6 of Reference 39. These calculations (not repeated for the current PIE) clearly predict pellet hourglassing (due to a greater axial thermal expansion along the pellet centerline) with cladding contact at the pellet ends. The applied loading is sufficient to induce local yielding. This explains the small local cladding deformations (“primary ridges”) measured in the PIEs.

13. The empirical creep correlation described in Section 7.4 represents adequately the outward relocation of the MOX test fuel pins.

14. The uneven and noncontiguous nature of the corrosion observed on the cladding inner surfaces is an artifact of the manner in which the pellet fragments came into contact with the cladding during irradiation. Inner surface oxidation requires that excess oxygen be available and that the fuel be in contact with the cladding to provide a path for solid-state athermal diffusion of the oxygen atoms. The thicker oxidation layers over the agglomerates follow directly from the narrower local pellet-clad gaps during irradiation. The observed clad corrosion patterns are in accordance with expectations based on the European experience.

15. The CARTS and FRAPCON-based calculations for the 50-GWd/MT Capsules 5, 6, and 12 have been repeated with code input adjusted as necessary to conform to the current PIE results:

    a. Fuel densification is specified as 2.0% densification complete by 10.0 GWd/MT burnup. This model, first used in the previous (30-GWd/MT) PIE, was also found accurate for the 40-GWd/MT fuel pins.

    b. The burnup-dependent fission gas release fraction representation has been set to match the observations (at 50 GWd/MT) of 7.2% for Capsule 6 (Fuel Pin 9), 8.6% for Capsule 12 (Fuel Pin 15), and 3.1% for Capsule 5 (Fuel Pin 8).

    c. The models for clad diameter increase have been modified to reflect the observed clad expansion (Items 11 and 13 above).

    d. The CARTS predictions for capsule conditions in the hot cell obtained in advance of the PIE are found to have been reasonably accurate. The new CARTS calculations predict fuel structural dimensions that agree closely with the PIE observations.

    e. Post-PIE CARTS calculations resulted in fuel centerline temperatures 10–20% higher than the pre-PIE calculations, and in all cases the centerline temperatures approached or exceeded the Halden threshold (thus fission gas release rates greater than 1% should be expected).

    f. FRAPCON-3 calculations of the fission gas releases compare very closely with the PIE results.

16. The behavior of this weapons-derived fuel, evaluated at a burnup of 50 GWd/MT, is similar to the European experience with reactor-grade MOX fuel.

11. REFERENCES

1. B. S. Cowell and S. A. Hodge, *Fissile Materials Disposition Program Light-Water Reactor Mixed Oxide Fuel Irradiation Test Project Plan*, ORNL/MD/LTR-78, Rev. 3, February 2004.
2. D. G. Kolman, M. E. Griego, C. A. James, and D. P. Butt, "Thermally Induced Gallium Removal From Plutonium Dioxide for MOX Fuel Production," *J. Nuclear Materials*, **282**, 245–254 (2000).
3. R. N. Morris, J. Giaquinto, and S. A. Hodge, *MOX Average Power Test Fuel Pellet Initial Gallium Content*, ORNL/MD/LTR-182, Oak Ridge National Laboratory, Oak Ridge, Tennessee, March 2000.
4. R. N. Morris et al., *MOX Average Power 30 GWd/MT PIE: Final Report*, ORNL/MD/LTR-212, Volume 1, Oak Ridge National Laboratory, Oak Ridge, Tennessee, November 2001.
5. R. N. Morris, C. A. Baldwin, and C. M. Malone, *MOX Fission Gas Pressure Measuring Apparatus*, ORNL/MD/LTR-176, Oak Ridge National Laboratory, Oak Ridge, Tennessee, January 2000.
6. J. A. Turnbull et al., *Measurement of ^{85}Kr As A Method For Assessing Fission Gas Release in CAGR Fuel Pins*, Nuclear Fuel Performance BNES, 319–325, London, 1985.
7. S. A. Hodge, *Effects of Fission Gas Release and Pellet Swelling Within the LWR Mixed-Oxide Irradiation Test Assembly*, ORNL/MD/LTR-83, Rev. 1, Oak Ridge National Laboratory, Oak Ridge, Tennessee, November 1997.
8. P. Blanpain et al., "Recent Results From The In-Reactor MOX Fuel Performance in France and Improvement Program," pp 39–45 in *Proceedings of the 1997 International Topical Meeting on LWR Fuel Performance, Portland, Oregon, March 1997*, American Nuclear Society, 1997.
9. Y. Guerin et al., "Microstructure Evolution and In-Reactor Behaviour of MOX Fuel," *LWR Fuel Performance Conference, Park City, Utah, April 10–13, 2000*.
10. I. Kamimura et al., "Helium Generation and Release in MOX Fuels," *IAEA Symposium "MOX Fuel Cycle Technologies for Medium and Long Term Deployment," Vienna, 17–21 May 1999*.
11. T. Mitsugi et al., "Behavior of MOX Fuel Irradiated in a Thermal Reactor," *Proceedings of the 1997 International Topical Meeting on LWR Fuel Performance, Portland, Oregon, March 1997*.
12. W. Goll et al., "Irradiation Behavior of UO_2/PuO_2 Fuel in Light Water Reactors," *Nuclear Technology*, **102**, 29–46 (April 1993).
13. H. Bailly, D. Menessier, and C. Prunier, Eds., *The Nuclear Fuel of Pressurized Water Reactors and Fast Reactors—Design and Behaviour*, Lavoisier Publishing Inc., Secaucus, New Jersey, 1999.
14. L. Caillot et al., "Analytical Studies of the Behavior of MOX Fuel," pp. 62–69 in *Proceedings of the 1997 International Topical Meeting on LWR Fuel Performance, Portland, Oregon, March 1997*, American Nuclear Society, 1997.
15. C. T. Walker, W. Goll, and T. Matsumura, "Effect of Inhomogeneity on the Level of Fission Gas and Cesium Release from OCOM MOX Fuel During Irradiation," *J. Nuclear Materials*, **228**, 8–17 (1996).
16. B. S. Cowell and S. F. Fisher, *Survey of Worldwide Light Water Reactor Experience With Mixed Uranium-Plutonium Oxide Fuel*, ORNL/TM-13428, Oak Ridge National Laboratory, Oak Ridge, Tennessee, February 1999.
17. Personal Communication. These differences were noted by Mr. Tom Blair, who directly supervised the preparation of the MOX test fuel at Los Alamos National Laboratory.
18. P. Blanpain, C. Callens, G. Chiarrelli, J. Guillet, and W. Goll, *MOX Fuel Performance and Development*, European Nuclear Society TOPFUEL Meeting, Stockholm, May 2001.
19. M. D. Freshley et al., "Behavior of Discrete Plutonium-Dioxide Particles in Mixed-Oxide Fuel During Rapid Power Transients," *Nuclear Technology*, p. 239 **(**August 15, 1972).
20. T. Abe, N. Nakae, K. Kodato, M. Matsumoto, and T. Inabe, "Failure Behavior of Plutonium–Uranium Mixed Oxide Fuel Under Reactivity-Initiated Accident Condition," *J. Nuclear Materials*, **188**, 154–161 (1992).
21. ASTM Designation C 833–01, "Standard Specification for Sintered (Uranium-Plutonium) Dioxide Pellets," approved June 10, 2001.

22. "Appendix D" *Fuel Qualification Plan* prepared by Framatome ANP for U.S. Department of Energy dated April 2001.
23. B. S. Cowell, *Technical Specification: Mixed-Oxide Pellets for the Light-Water Reactor Irradiation Demonstration Test*, ORNL/MD/LTR-75, Oak Ridge National Laboratory, Oak Ridge, Tennessee, June 1997.
24. G. S. Chang, "Pu-rich MOX Agglomerate-by-Agglomerate Model for Fuel Pellet Burnup Analysis," *Proceedings of ICONE 12: Nuclear Energy—Powering the Future, Arlington, Virginia, April 25–29, 2004*.
25. C. T. Walker, W. Goll, and T. Matsumura, "Further Observations on OCOM MOX Fuel; Microstructure in the Vicinity of the Pellet Rim and Fuel-Cladding Interaction," *J. Nuclear Materials*, **245**, 169–178 (1997).
26. R. Manzel and C. T. Walker, "EPMA and SEM of Fuel Samples from PWR Rods with an Average Burn-up of Around 100 MWd/kg HM," *J. Nuclear Materials*, **301**, 170–182 (2002).
27. S. B. Fisher et al., "Microstructure of Irradiated SBR MOX Fuel and Its Relationship to Fission Gas Release," *J. Nuclear Materials*, **306**, 153–172 (2002).
28. R. N. Morris et al., *MOX Average Power Intermediate PIE: 21 GWd/MT Final Report*, ORNL/MD/LTR-199, Oak Ridge National Laboratory, Oak Ridge, Tennessee, December 2000.
29. R. N. Morris et al., *MOX Average Power 40 GWd/MT PIE: Final Report*, ORNL/MD/LTR-241, Volume 1, Oak Ridge National Laboratory, Oak Ridge, Tennessee, August 2003.
30. C. Ronchi and C. T. Walker, "Determination of Xenon Concentration in Nuclear Fuels by Electron Microprobe Analysis," *J. Phys. D: Appl. Phys*., **13**, 2175–84 (1980).
31. R. E. Woodley, "Variation in the Oxygen Potential of a Mixed-Oxide Fuel with Simulated Burnup," *J. Nuclear Materials*, **74**, 290–296 (1978).
32. L. Desgranes, "Internal Corrosion Layer in PWR Fuel," pp. 187–195 in *OECD Proceedings, Seminar on Thermal Performance of High Burn-up LWR Fuel, March 3–6, 1998, CEA, Cadarache, France*.
33. H. R. Peters and J. L. Harlow, "The Effect of the Trace Impurity Uranium on PWR Aqueous Corrosion of Zircaloy-4," pp. 295–318 in *Zirconium in the Nuclear Industry: Eleventh International Symposium, ASTM STP1295*, E. R. Bradley and G. P. Sabol, Eds., American Society for Testing and Materials, 1996.
34. R. N. Morris et al., *MOX Average Power Early PIE: 8 GWd/MT Final Report*, ORNL/MD/LTR-172, Oak Ridge National Laboratory, Oak Ridge, Tennessee, November 1999.
35. R. N. Morris et al., *MOX Test Fuel 50 GWd/MT PIE: Capsules 6 and 12 Final Report*, ORNL/MD/LTR-279, Volume 1, Oak Ridge National Laboratory, Oak Ridge, Tennessee, September 2005.
36. R. N. Morris et al., *MOX Test Fuel 50 GWd/MT PIE: Capsule 5 Final Report*, ORNL/MD/LTR-280, Volume 1, Oak Ridge National Laboratory, Oak Ridge, Tennessee, September 2005.
37. R. N. Morris and C. A. Baldwin, *MOX Fuel Pin Measuring Apparatus*, ORNL/MD/LTR-209, Oak Ridge National Laboratory, Oak Ridge, Tennessee, March 2001.
38. R. N. Morris et al., *MOX Average Power Test 30 GWd/MT PIE: Quick Look*, ORNL/MD/LTR-208, Oak Ridge National Laboratory, Oak Ridge, Tennessee, February 2001.
39. S. A. Hodge, L. J. Ott, F. P. Griffin, and C. R. Luttrell, *Implications of the PIE Results for the 30-GWd/MT-Withdrawal MOX Capsules*, ORNL/MD/LTR-212, Volume 2, Rev. 1, Oak Ridge National Laboratory, Oak Ridge, Tennessee, February 2002.
40. S. A. Hodge, L. J. Ott, and F. P. Griffin, *Implications of the PIE Results for the 40-GWd/MT-Withdrawal MOX Capsules*, ORNL/MD/LTR-241, Volume 2, Oak Ridge National Laboratory, Oak Ridge, Tennessee, September 2003.
41. "Image-Pro Plus," Version 5.1, Media Cybernetics, 8484 Georgia Avenue, Silver Spring, Maryland.
42. S. A. Hodge, *Fission Gas Release and Pellet Swelling Within the Capsule Assembly During Phase IV of the Average Power Test*, ORNL/MD/LTR-184, Oak Ridge National Laboratory, Oak Ridge, Tennessee, July 2000.

43. R. N. Morris and D. W. Heatherly, *MOX Fuel Pin Volume Measuring Apparatus*, ORNL/MD/LTR-232, Oak Ridge National Laboratory, Oak Ridge, Tennessee, September 2002.
44. *ESCORE—The EPRI Steady-State Core Reload Evaluator Code: General Description*, EPRI NP-5100, Combustion Engineering, Inc., Windsor, Connecticut, February 1987.
45. G. A. Berna et al., *FRAPCON-3: A Computer Code for the Calculation of Steady-State Thermal-Mechanical Behavior of Oxide Fuel Rods for High Burnup*, NRC Report NUREG/CR-6534, December 1997.
46. G. S. Chang, *MCNP and ORIGEN-2 Calculated Axial, Radial, and Azinuthal Profiles Versus Burnup in the MOX Test Assembly*, ORMOX-GSC-10-00, Idaho National Engineering and Environmental Laboratory, March 2000.
47. M. A. McGrath, *In-Reactor Creep Behavior of Zircaloy Cladding*, International Topical Meeting on LWR Fuel Performance, American Nuclear Society, Park City, Utah, April 10–13, 2000.
48. A. Soniak et al., "Irradiation Creep Behavior of Zr-Base Alloys," pp. 837–862 in *Zirconium in the Nuclear Industry: Thirteenth International Symposium*, ASTM STP 1423, G. D. Moan and P. Rudling, Eds., ASTM International, 2002.
49. M. Limback and T. Andersson, "A Model for Analysis of the Effect of Final Annealing on the In- and Out-of-Reactor Creep Behavior of Zircaloy Cladding," pp. 448–468 in *Zirconium in the Nuclear Industry: Eleventh International Symposium*, ASTM STP 1295, E. R. Bradley and G. P. Sahol, Eds., American Society for Testing and Materials, 1996.
50. R. N. Morris et al., *MOX Test Fuel 50 GWd/MT PIE: Capsules 6 and 12 Quick Look*, ORNL/MD/LTR-271, Oak Ridge National Laboratory, Oak Ridge, Tennessee, January 2005.
51. C. Vitanza, E. Kolstad, and U. Graziami, Fission Gas Release from UO_2 Pellet Fuel at High Burn-up, "ANS Topical Meeting on Light Water Reactor Fuel Performance," Portland, Oregon, 29 April–3 May, 1979.
52. W. Wiesenack, "Issues Related to High Burnup Utilization, and Experimental Results from the OECD Halden Reactor Project," Colloquium on High Burnup Fuels for LWRs: Benefits and Limitations, Massachusetts Institute of Technology, Cambridge, Massachusetts, January 23, 2003.
53. R. N. Morris et al., *MOX Test Fuel 50 GWd/MT PIE: Capsule 5 Quick Look*, ORNL/MD/LTR-272, Oak Ridge National Laboratory, Oak Ridge, Tennessee, January 2005.

INTERNAL DISTRIBUTION

1. C. A. Baldwin
2. K. J. Beierschmitt
3. J. L. Binder
4. E. E. Bloom
5. W. R. Corwin
6. B. S. Cowell
7. K. M. Downer
8. S. E. Fisher
9. S. R. Greene
10. F. P. Griffin
11. D. W. Heatherly
12. W. R. Hendrich
13. J. N. Herndon
14. L. L. Horton
15. R. A. Jaramillo
16. C. R. Luttrell
17–21. R. N. Morris
22. D. L. Moses
23–27. L. J. Ott
28. N. H. Packan
29. J. E. Rushton
30. D. J. Spellman
31. K. R. Thoms
32. G. L. Yoder, Jr.
33. S. J. Zinkle
34. ORNL Laboratory Records (RC)

EXTERNAL DISTRIBUTION

35. D. Alberstein, Los Alamos National Laboratory, MS-E541, P.O. Box 1663, Los Alamos, NM 87545
36. P. Bailey, Duke Energy, P.O. Box 1006, Charlotte, NC 28201-1006
37. S. Basu, U.S. Nuclear Regulatory Commission, RES/DSARE/AREAB, Two White Flint North, MS-10F13A, 11555 Rockville Pike, Rockville, MD 20852
38. C. Beyer, Pacific Northwest National Laboratory, 3230 Q Street, Richland, WA 99354
39. R. N. Boudreau, DOE/NA-26, Forrestal Building, 1000 Independence Avenue SW, Washington, DC 20585
40. R. Clark, Duke/Cogema/Stone & Webster, P.O. Box 31847, Charlotte, NC 28231-1847
40. F. Eltawila, U.S. Nuclear Regulatory Commission, RES/DSARE, Two White Flint North, MS-10E32, 11555 Rockville Pike, Rockville, MD 20852
41. M. W. Kennard, Stoller Nuclear Fuel, 1 Baltic Place, Suite 201A, Croton-on-Hudson, NY 10520
42. D. Lanning, Pacific Northwest National Laboratory, 3230 Q Street, Richland, WA 99354
43. R. Y. Lee, U.S. Nuclear Regulatory Commission, RES/DSARE/SMSAB, Two White Flint North, MS-10K8, 11555 Rockville Pike, Rockville, MD 20852
44. G. D. Lunsford, DOE/NA-265, Forrestal Building, 1000 Independence Avenue SW, Washington, DC 20585
45–49. G. Meyer, Framatome Cogema Fuels, 3315 Old Forest Road, Lynchburg, VA 24506
50. R. O. Meyer, U.S. Nuclear Regulatory Commission, RES/DSARE/SMSAB, Two White Flint North, MS-10K8, 11555 Rockville Pike, Rockville, MD 20852
51. S. Nesbit, Duke Energy, P.O. Box 1006, Charlotte, NC 28201-1006
52. M. D. Newdorf, DOE/NA-261, Forrestal Building, 1000 Independence Avenue SW, Washington, DC 20585
53. J. Olencz, DOE/NA-26, Forrestal Building, 1000 Independence Avenue SW, Washington, DC 20585
54–57. R. C. Pedersen, Idaho National Laboratory, Mail Stop 7101, P.O. Box 1625, Idaho Falls, ID 83415-7101

58. P. T. Rhoads, U.S. Department of Energy, 1000 Independence Avenue SW, Forrestal Building, Washington, DC 20585
59. H. H. Scott, U.S. Nuclear Regulatory Commission, RES/DSARE/SMSAB, Two White Flint North, MS-10K8, 11555 Rockville Pike, Rockville, MD 20852